Clinical transitions in photoacoustic imaging

by

Tyler Joshua Harrison

A thesis submitted in partial fulfillment of the requirements for the degree of

Doctor of Philosophy

in

Biomedical Engineering

Department of Electrical and Computer Engineering
University of Alberta

Abstract

Optical imaging has long been a gold standard for medical imaging. However, due to the high optical scattering in tissues, it has not been possible to image deeper than a few wavelengths with a useful resolution. Photoacoustic imaging - the use of short-pulsed lasers to induce an ultrasound signal - can provide optical contrast at ultrasonic resolution. This thesis focuses on the refinement of photoacoustic imaging for practical use by clinicians in clinical and preclinical studies. The first focus of this work is in system development. Beginning with a single-element based system suitable for some preclinical studies, we have worked towards a more practical ultrasound array based system. This system provides several different ultrasound modes to augment the photoacoustic data available including ultrasound flash imaging, synthetic aperture imaging, and ultrasound Doppler imaging. With this array system we demonstrate two fundamentally different clinically-applicable photoacoustic techniques using both optical and acoustic resolution. Similar methods may be used with both of these using multiple interrogation wavelengths providing label-free functional imaging. Other system development work has focused on transducer design and fabrication to provide better imaging capabilities. The second focus of this thesis is image reconstruction. We explore alternative imaging techniques using different source/array geometries and illumination patterns, demonstrate the applicability of ultrasound beamformers to photoacoustic imaging, and even work with different ultrasound imaging techniques including s-sequence

excitation and minimum variance beamforming. The final focus is on clinical applications. We show photoacoustic imaging of gene expression through a tyrosinase reporter gene developed by my colleagues with exciting applications in studying metabolic pathways and cancer development. Using a longer wavelength, We also demonstrate the imaging of small metallic seeds used in brachytherapy which may aid in localizing them during radiotherapy of prostate cancer. Finally, we demonstrate multi-modal human imaging of the thyroid *in vivo*. Through exploration of system development, image reconstruction, and applications, this thesis aims to prove the clinical practicality of photoacoustic imaging.

Preface

This thesis is an original work by Tyler Joshua Harrison. The research projects, which this thesis is a part, received research ethics approval from the University of Alberta Research Ethics Board

- Animal imaging protocol: AUP00001170
- Human imaging protocol: Pro00007759_AME4

Some of the research for this thesis derives from collaborative work, both with lab members working under Dr. Roger Zemp, and in the case of chapter 4, we worked in collaboration with Dr. Edward Wiebe. The thesis introduction in chapter 1, the background information in chapter 2, and the final discussion in 12 are all my original work.

Chapter 3 has been published as: T. Harrison, J. Ranasinghesagara, H. Lu, K. Mathewson, A. Walsh, and R. Zemp, "Combined photoacoustic and ultrasound biomicroscopy," Opt. Express 17, 22041-22046 (2009). I was responsible for system debugging, data collection, and analysis with the assistance of J. Ranasinghesagara. Portions of the manuscript writing were handled by myself, H. Lu, and J. Ranasinghesagara. J. Ranasinghesagara was responsible for the compilation and submission of the manuscript. R. Zemp was the supervisory author and was involved with conceptual development and manuscript preparation.

Chapter 4 has been published as: T. Harrison, D. Jeffery, E. Wiebe, and Roger J. Zemp, "Real-time clinically oriented array-based in vivo combined photoacoustic and power Doppler imaging." Proc. SPIE 8943, Photons Plus Ultrasound: Imaging and Sensing 2014, 89435A (March 3, 2014), doi:10.1117/12.2040609. My contribution was the implementation of the imaging mode and reconstruction techniques, data collection, analysis and writing of the paper. D. Jeffery aided in the data collection. R. Zemp was the supervisory author and was involved with conceptual development and manuscript preparation.

Chapter 5 has been published as: Tyler Harrison, Parsin Hajireza, Alexander Forbrich, Roger Zemp, "Optical-resolution photoacoustic micro-endoscopy with ultrasound array system detection ." Proc. SPIE 8581, Photons Plus Ultrasound: Imaging and Sensing 2013, 85810C (March 4, 2013), doi:10.1117/12.2004887. My contribution was the development of the data acquisition and imaging mode, and phantom construction. P. Hajireza developed the optical setup, and A. Forbrich aided with data collection. I was responsible for the compilation of the manuscript, with some writing provided by P. Hajireza. R. Zemp was the supervisory author and was involved with conceptual development and manuscript preparation.

Chapter 6 has been published as: Harrison, T., Zemp, R.J., "The applicability of ultrasound dynamic receive beamformers to photoacoustic imaging," Ultrasonics, Ferroelectrics and Frequency Control, IEEE Transactions on , vol.58, no.10, pp.2259,2263, October 2011 doi: 10.1109/TUFFC.2011.2076. I was responsible for the implementation of simulations, reconstruction techniques, experimental data collection, and writing of the manuscript. R. Zemp was the supervisory author and was involved with conceptual development and manuscript preparation.

Chapter 7 has been published as: T. Harrison, P. Shao, and R. Zemp, "A least-squares fixed-point iterative algorithm for multiple illumination photoacoustic tomography," Biomed. Opt. Express 4, 2224-2230 (2013). My contribution was the implementation and simulation of the multiple-illumination iterative approach from theory developed by R. Zemp. P. Shao provided some initial code. I was responsible for the drafting of the manuscript. R. Zemp was the supervisory author and was involved with conceptual development and manuscript preparation.

Chapter 8 has been published as: Harrison, T., Sampaleanu, A., Zemp, R.J., "S-sequence spatially-encoded synthetic aperture ultrasound imaging," Ultrasonics, Ferroelectrics and Frequency Control, IEEE Transactions on , vol.61, no.5, pp.886,890, May 2014 doi: 10.1109/TUFFC.2014.6805701. My contribution was the adaptation of code provided by A. Sampaleanu from simulations for a different array geometry to a linear array geometry, and adaptation to our experimental system. I ran all simulations, collected all data, and drafted the manuscript. R. Zemp was the supervisory author and was involved with conceptual development and manuscript preparation.

Chapter 9 has been submitted for publication as: T. Harrison, P. Shao, and R. Zemp, "S-sequence spatial coding for iterative multiple illumination photoacoustic tomography," J. Biomed. Opt. 140294P. My contribution was the simulation design, implementation, and paper authorship. P. Shao aided with some of the initial coding. R. Zemp was the supervisory author and was involved with conceptual development and manuscript preparation.

Chapter 10 has been published as: Harrison T, Zemp RJ, "Coregistered photoacoustic-ultrasound imaging applied to brachytherapy." J. Biomed. Opt. 16(8):080502-080502-3. doi:10.1117/1.3606566. My contribution was experimental design, the collection and analysis of data, and drafting of the manuscript. R. Zemp was the supervisory author and was involved with conceptual devel-

opment and manuscript preparation.

Chapter 11 has been published as: Tyler Harrison, Robert J. Paproski, Roger J. Zemp, "In vivo imaging of inducible tyrosinase gene expression with an ultrasound array-based photoacoustic system." Proc. SPIE 8223, Photons Plus Ultrasound: Imaging and Sensing 2012, 82230S (February 9, 2012), doi:10.1117/12.908987. R.J. Paproski prepared the mice and cell lines used, my contribution was photoacoustic imaging and analysis. I was responsible for manuscript drafting and submission, with some sections written by R.J. Paproski. R. Zemp was the supervisory author and was involved with conceptual development and manuscript preparation.

Acknowledgements

I gratefully acknowledge the funding support of NSERC, Alberta Advanced Education & Technology, Alberta Innovates Technology Futures, and the University of Alberta.

I would also like to thank my supervisor, Dr. Roger Zemp, and my colleagues past and present (listed in no particular order): Janaka Ranasinghesagara, Peiyu Zhang, Robert Paproski, Parsin Hajireza, Alexander Forbrich, Huihong (Jack) Lu, Peng (Clark) Shao, Yan Jiang, Wei Shi, Alexander Sampaleanu, Ryan Chee, and Tarek Kaddoura.

Additionally, I acknowledge the contributions of the various summer students that have spent time in our lab, and all of our collaborators, particularly Dr. Usmani, Dean Jeffries, and Dr. Weibe without whom many of our studies would have been impossible.

Finally, I thank my supervisory committee and all the staff in both the Electrical and Computer Engineering department and the Faculty of Graduate Studies and Research for the support and structure under which I have completed my studies.

List of Symbols

This list is not exhaustive, but serves simply as a quick reference to aid the reader. In order of appearance.

- $f_{\#}$: F-number, an ultrasound parameter defined as the ratio of focal distance to transducer diameter.
- f: Ultrasound focal distance.
- D: Transducer focal diameter.
- p_0: Initial pressure distribution (i.e. photoacoustic image).
- μ_a: Optical absorption, a material property.
- Φ: Optical fluence; a measure of local optical energy per unit area.
- Γ: Grüneisen paramter, material property relating energy absorption to initial pressure.
- μ_s': Optical scattering, a material property.
- σ: Typically, standard deviation of noise. May also refer to a regularization paramter.
- c: Speed of sound.
- a: Scaling factor for speed of sound available on ultrasound systems.

- λ: Ultrasound wavelength.
- $\hat{\cdot}$: Estimated value.
- $\mathbf{r}$: Spatial position.
- diag$(\cdot)$: Diagonal operator, arranges inputs along the diagonal of a matrix.
- ϵ: Measurement of error.
- $\kappa_2(\cdot)$: Condition number, describes how quickly the output of a linear system varies with changes of the input (i.e. how much noise variation will change the output). Uses L^2 norm.
- L^2 norm: Integral of the magnitude squared of the input vector, calculate condition number.
- β: Regularization parameter for MIPAT.

Glossary of Terms

Terms that may not defined every time they are used. *This is not an exhaustive list, but is presented alphabetically as an aid to the reader.*

- *A-line*: A 1-D image in depth (time) produced by an ultrasound system.
- *Atherosclerosis*: A buildup of plaque in arteries.
- *AUC*: Area Under the Curve, the area under an ROC curve. It is a measure of classifier performance, and is ideally close to 1.
- *Beamforming*: Using time-of-flight delays to reconstruct an image (either in ultrasound or photoacoustic imaging).
- *B-mode image*: 2-D image formed by collecting A-lines.
- *Brachytherapy*: A cancer treatment using small, metallic, radioactive seeds.
- *Contrast*: Signal distinguishable above background in an image.
- *C-scan image*: A 2-D en-face image (i.e. not depth resolved, typical of OR-PAM).
- *Doppler ultrasound*: A technique that takes advantage of the Doppler effect to measure the speed of particles using ultrasound.

- *DOT*: Diffuse Optical Tomography, a pure optical technique that measures optical absorption deep in tissues.
- *Endoscope*: A remote imaging system that uses a long flexible probe to view areas such as blood vessels or the digestive tract.
- *Exogenous*: Originating outside the body.
- *ex vivo*: From latin, outside the body.
- *Hemoglobin*: Oxygen carrier molecule in blood. Has oxy- (with oxygen) and deoxy- (without oxygen) states with differing amounts of optical absorption.
- *in vivo*: From latin, inside the body.
- *MCF-7*: An immortalized breast cancer cell line commonly used in cancer studies.
- *Melanin*: The pigment in human skin.
- *Microvasculature*: Small blood vessels; capillary networks.
- *MIPAT*: Multiple Illumination Photoacoustic Tomography, a photoacoustic tomography technique that uses multiple illuminations to perform quantitative recovery of optical absorption.
- *NRMSE*: Normalized RMSE, uses a slightly different definition to scale the error relative to the magnitude of the image.
- *OR-PAM*: Optical Resolution Photoacoustic Microscopy, a technique that uses optical focusing rather that ultrasonic focusing to determine pixel locations.
- *Photoacoustic (PA) imaging*: The use of ultrasound to form images of initial pressures caused by heating due to incident light.

- *PRF*: Pulse repetition frequency, the freqeuncy at which a laser pulses.
- *PSF*: Point-spread-function, A 1-D projection of the image of a point (ideally much smaller than the expected resolution of a system). Can be used to quantify resolution.
- *Realtime*: Typically refers to video-rate (30fps) capture.
- *Resolution*: A property of an imaging system, the smallest distance between points which will allow them to be distinguished.
- *RMSE*: Root Mean Squared Error, a measure of how well an image is reproduced.
- *ROC*: Receiver Operating Characteristic, a type of analysis that measures classifier performance by plotting false positives vs. true positives.
- *ROI*: Region of Interest, the area of the image that constitutes a true signal.
- *SNR*: Signal-to-noise ratio, a measure of image quality.
- *Ultrasound (US) imaging*: A technique using transmission and measured backscattered mechanical waves to form images.
- *Tomography*: Using a detector ring (or circular-scanned detector) to form cross-sectional images.
- *Transactivator*: A genetic sequence that will cause the activation of another gene in the presence of some substance.
- *Transducer*: A device capable of converting between energy domains; here used to refer to an ultrasound device capable of transmission and reception of signals.

- *Tyrosinase*: An enzyme responsible for the production of melanin by the conversion of an amino acid, tyrosine.
- *Vascular:* Relating to blood vessels.
- *VDAS*: Verasonics Data Acquisition System, a flexible ultrasound research system.
- *Xenograft*: Tissue originating from a different species.

Contents

List of Figures

Chapter 1

Introduction

1.1 Thesis objectives

Photoacoustic imaging is a hybrid optical-ultrasound technique that may be applied to medical imaging problems. It offers deep-tissue optical contrast at ultrasonic resolution, extending this contrast far beyond what is possible with purely optical techniques in turbid media. The main absorbers of light in the body are hemoglobin and melanin, suggesting two important clinical applications relating to cancer imaging: melanoma detection, and angiogenesis studies. However, with the addition of exogenous contrast agents, such as tagged injectable dyes, the potential applications expand considerably.

While photoacoustic imaging has been around for several years, it is still in its infancy in terms of clinical adoption. The aim of the thesis work is the development of combined ultrasound-photoacoustic imaging systems for clinical applications through three main aims:

1. Technology development - Different light delivery methods and ultrasound setups have been developed to create systems suitable for simultaneous ultrasound and photoacoustic imaging in a clinical setting.

2. Reconstruction techniques - Many image reconstruction approaches have

been explored for both ultrasound and photoacoustic imaging.

3. Applications - With the help of collaborators collaborators, some potential clinical uses for combined ultrasound-photoacoustic techniques have been introduced.

This thesis is titled 'Clinical transitions in photoacoustic imaging' because the focus was on developing tools and feasability data for future translational studies, and it was anticipated that the impact would be less than true translational studies. The end goal of the work was to develop tools to allow the use of photoacoustic imaging in a clinical setting.

1.2 Key contributions

1.2.1 Technology development

Our first contribution to technology development focused on a fast-scanning single-element system (chapter 3)[1]. That system was the first high-frequency (>25 MHz) fast-scanning photoacoustic system, which allowed for fine resolution (defined as the minimum distance required between two points to see them distinctly) at video rates, naturally co-registered ultrasound and photoacoustic imaging, and included transmit gain compensation. Previous fast-scanning systems had focused on imaging at lower frequencies, making them less well-suited for studies of microvasculature. Additionally, the combination of voice-coil actuation and relatively high laser repetition rate lead to the first realtime ultrasound microscopy system with photorealistic capabilities. Our ultrasound capture was interlaced with photoacoustic capture permitting co-registered multi-media imaging. Transmit-gain-compensation (the use of an amplifier to account for ultrasound attenuation) is quite common in clinical ultrasound systems, but virtually unheard-of in fast-scanning systems. Our

approach allowed for separate gain for both ultrasound and photoacoustic imaging using the same hardware.

We subsequently acquired a Verasonics data acquisition system (VDAS, a flexible commercial ultrasound imaging platform) that allowed us to interface with an array transducer. This allowed for photoacoustic imaging using only a single laser pulse, which in turn allowed the use of a higher power tunable laser without sacrificing much in terms of frame rate. The more powerful laser limited us to 10 frames per second instead of the 30 or so we were getting with the fast-scanning system, but the flexibility of the VDAS platform allowed for the development of many novel imaging modes.

The such contribution was a combined flash ultrasound and photoacoustic imaging mode [2]. This mode captured flash ultrasound (i.e. using the entire aperture to transmit a plane wave) interlaced with photoacoustic images. Previous array-based efforts were constrained to phased-array imaging, with only a subset of elements available at a time. Flash imaging, while sacrificing quality, allows for very fast ultrasound imaging, or linear array walking aperture.

Later efforts focused on combined Doppler ultrasound and photoacoustic imaging (chapter 4)[3]. My colleagues had previously shown a similar combination of techniques using the fast scanning system with the ultimate goal of imaging oxygen flux (essentially functional imaging) [4]. Our effort was unique in combining Doppler ultrasound, ultrasound, and photoacoustic imaging on a single system with interlaced capture. To achieve functional imaging, it is important that the Doppler and photoacoustic images are as close together as possible temporally to avoid motion artifacts, and these images should in turn be very well registered with the ultrasound image to allow the identification of a region of interest. Our unique combined approach allows us to capture all three imaging modes in about the shortest time possible (limited

by time-of-flight for imaging depth).

The very high frame rate available with the VDAS system was instrumental in another study showing the first array-based photoacoustic endoscope guidance and image capture (chapter 5) [5, 6]. Previous endoscopy techniques had typically used a single-element transducer, either attached to the end or external to the endoscope. We were the first to demonstrate guiding the endoscope using an ultrasound imaging mode, followed by triggering and capturing data for an optical-resolution photoacoustic microscopy (OR-PAM) scan through an image-guide fiber. We proved the feasibility of this technique to several centimeters through tissue phantoms.

Finally, we implemented encoded synthetic aperture ultrasound using a new type of spatial encoding sequence (chapter 8)[7]. Synthetic aperture imaging uses multiple pulses of ultrasound from single elements to provide nearly ideal spatial resolution over the entire field of view at the cost of signal-to-noise ratio (SNR). Spatial encoding uses an array to encode each transmission by using multiple elements at once, which allows for decoding of the linear system to create a higher SNR version of the data from individual elements. Previous Hadamard-based encoding schemes depended on inverted ultrasound pulses, which are often not available at the same time as the non-inverted pulses. Additionally, the transducer may not transmit an exact inversion, causing image artifacts. Our new S-sequences require only non-inverted pulses, and achieve nearly the same theoretical and experimental SNR as Hadamard encoding sequences.

1.2.2 Reconstruction techniques

Delay-and-sum beamforming is the bread-and-butter of ultrasound image reconstruction. We wanted to explore the idea of using the hardware-based ultrasound beamformers available in commercial ultrasound systems to create

photoacoustic images by modifying the speed of sound (a typical parameter in commercial systems). We successfully demonstrated the concept using our VDAS system (chapter 6)[8], and demonstrated the viability on real data. This required the implementation and integration of both ultrasound and photoacoustic beamformers suitable for real-time use, and some experimental work with phantoms. While other systems had previously used commercial ultrasound platforms, they either gathered pre-beamformed data, or simply had very poor image quality.

Coincident to the work in this thesis, we also explored quantitative techniques for tomographic imaging reconstruction [9]. Work has focused on developing a family of algorithms to iteratively measure optical absorption using measured pressure estimates from multiple illumination events [9]. Previous tomographic work focused on the use of single illumination patterns. Issues arose when trying to quantitatively estimate optical properties due to the complex interplay between optical parameters. The introduction of multiple sources is similar to techniques used in Diffuse Optical Tomography (DOT). Multiple optical sources for photoacoustic tomography had not been fully explored. Thus, we used this concept of multiple illuminations to extend previous work based on an iterative technique using an initial pressure image from a single illumination. We demonstrated that issues with convergence due to overiteration and poor estimation of optical scattering may be ameliorated by this use of multiple sources (chapter 7)[10].

Finally, we have worked on improving SNR for this iterative multiple illumination technique by using patterned illumination based on S-sequences (chapter 9)[11], which we previously introduced for spatially-coded synthetic transmit aperture ultrasound (chapter 8) [7]. To our knowledge, this was that first application of such a patterned illumination to photoacoustic tomography.

1.2.3 Applications

The most straightforward application of photoacoustic imaging is simple vascular mapping. It is relatively straightforward for most setups as the dominant absorber in the body at most visible wavelengths is hemoglobin. Thus, even our early fast-scanning system could be used for vascular mapping (chapter 3)[1]. More recently, my colleagues have focused on microvasculature, which may be examined using Optical Resolution Photoacoustic Microscopy (OR-PAM). OR-PAM techniques employed by other groups have even tracked the oxygenation status of individual red blood cells. Functional imaging has been a tantalizing goal for researchers, and can be done even in large vessels to gain understanding of local metabolic activities [4].

Perhaps the fastest-growing areas of photoacoustic imaging research are imaging applications related to cancer. Similarly to vascular mapping, imaging melanistic tumors is quite easy - melanin absorbs very strongly in the visible range. There is a gene responsible for the conversion of the amino acid tyrosine into melanin, tyrosinase. Combined with a transactivator gene, tyrosinase can be used to signal the activation of a particular pathway. This leads to the potential for many studies into the efficacy of drug delivery, longitudinal deep-tissue tumor observation, and the imaging of gene expression or gene therapies. We created a tyrosinase sequence with a proof-of-concept transactivator, transfected MCF-7 cancer cells, and grew tumors in a murine model. We then used our combined flash-ultrasound/photoacoustic imaging mode to demonstrate this gene imaging technique for the first time (chapter 11)[12]. Another group had simultaneously developed a similar cell line based on the tyrosinase gene, but without the transactivator. Without the transactivator, the expression cannot be controlled, and thus their cell line only appeared dark. Our cell line has the capability of tyrosinase expression being linked to a metabolic activity, or the presence of a drug, and is thus more

useful for studies into drug delivery or cellular mechanisms.

We have since shifted focus slightly towards more clinical applications in humans. First, we have assessed the use of photoacoustic imaging for tracking tiny metallic seeds used for a type of prostate cancer treatment called brachytherapy. Currently, ultrasound is the gold standard for placement, but the seeds can be difficult to locate in the body. We conducted the first study into this imaging target, showing that photoacoustic imaging in the near infrared provides high contrast (i.e. signal level compared to surrounding tissue) seed images compared to blood, allowing for deep imaging in tissue (chapter 10)[13]. Previous efforts had shown the viability of photoacoustic needle guidance, but had not explored the appropriate wavelengths, or looked at brachytherapy seeds.

Finally, we have been working on thyroid imaging for the purpose of distinguishing malignant versus benign growths. We are interested in comparing flow information from ultrasound Doppler to photoacoustic contrast to measure the vascularity, though the work so far is preliminary (chapter 4) [3]. Nonetheless, we demonstrate that it is feasible to image to an appropriate depth in the neck to photoacoustically assess the thyroid with a linear array transducer, and we were the first to do so simultaneously with both photoacoustic and Doppler measurements.

1.3 Layout of the thesis

Chapter 2 will provide additional background information that is intended to aid the reader in contextualizing the remainder of the work. Subsequent chapters are derived from individual publications, save chapter 12, which provides an in-depth discussion to wrap up the thesis. For a detailed description of the individual contributions to each published work included in Chapters 3 to 11,

please refer to the preface.

The main body of the thesis is roughly divided into three parts, corresponding to the three aims. Chapters 3 through 5 deal with system development; discussing single-element (chapter 3 [1]), combined photoacoustic and ultrasound Doppler (chapter 4 [3]), and fast capture for optical resolution photoacoustic microscopy (chapter 5 [5]). Chapters 6 through 9 discuss beamforming (chapter 6), multiple-source iterative techniques for quantitative imaging (chapter 7 [10]), and S-sequence encoding for ultrasound (chapter 8 [7]) and photoacoustic (chapter 9 [14]) imaging. Finally, chapters 10 [13] and 11 [12] deal with photoacoustic imaging applications involving imaging brachytherapy seeds and gene expression.

References

[1] Tyler Harrison et al. "Combined photoacoustic and ultrasound biomicroscopy". In: *Optics Express* 17.24 (2009), pp. 22041–22046. DOI: 10.1063/1.2195024.2..

[2] Tyler Harrison and Roger J. Zemp. "Interlaced realtime channel-domain photoacoustic and ultrasound imaging". In: *Proceedings of SPIE*. Vol. 7899. 2011, pages. DOI: 10.1117/12.875507.

[3] Tyler Harrison et al. "Real-time clinically oriented array-based in vivo combined photoacoustic and power Doppler imaging". In: vol. 8943. 2014, pages. DOI: 10.1117/12.2040609.

[4] Yan Jiang et al. "Blood oxygen flux estimation with a combined photoacoustic and high-frequency ultrasound microscopy system: a phantom study." In: *Journal of biomedical optics* 17.3 (Mar. 2012), p. 036012. ISSN: 1560-2281. DOI: 10.1117/1.JBO.17.3.036012.

[5] Tyler Harrison et al. “Optical-resolution photoacoustic micro-endoscopy with ultrasound array system detection”. In: vol. 8581. 2013, pages. DOI: 10.1117/12.2004887.

[6] Parsin Hajireza et al. “Optical resolution photoacoustic microendoscopy with ultrasound-guided insertion and array system detection”. In: *Journal of Biomedical Optics* 18.9 (2013), pp. 090502–090502. DOI: 10.1117/1.JBO.18.9.090502.

[7] Tyler Harrison, Alexander Sampaleanu, and Roger J. Zemp. “S-Sequence Spatially-Encoded Synthetic Aperture Ultrasound Imaging”. In: 61.5 (2014), pp. 886–890. DOI: 10.1109/TUFFC.2014.2979.

[8] Tyler Harrison and Roger J Zemp. “The applicability of ultrasound dynamic receive beamformers to photoacoustic imaging.” In: *IEEE transactions on ultrasonics, ferroelectrics, and frequency control* 58.10 (Oct. 2011), pp. 2259–63. ISSN: 1525-8955. DOI: 10.1109/TUFFC.2011.2076.

[9] Peng Shao, Tyler Harrison, and Roger J. Zemp. “Iterative algorithm for multiple illumination photoacoustic tomography (MIPAT) using ultrasound channel data”. In: *Biomed. Opt. Express* 3.12 (Dec. 2012), pp. 3240–3249. DOI: 10.1364/BOE.3.003240.

[10] Tyler Harrison, Peng Shao, and Roger J. Zemp. “A least-squares fixed-point iterative algorithm for multiple illumination photoacoustic tomography”. In: *Biomed. Opt. Express* 4.10 (Oct. 2013), pp. 2224–2230. DOI: 10.1364/BOE.4.002224.

[11] Tyler Harrison, Peng Shao, and Roger Zemp. “S-sequence patterned illumination for fixed-point iterative multiple illumination photoacoustic tomography”. In: vol. 8943. 2014, pages. DOI: 10.1117/12.2040580.

[12] Tyler Harrison, Robert J. Paproski, and Roger J. Zemp. "In vivo imaging of inducible tyrosinase gene expression with an ultrasound array-based photoacoustic system". In: vol. 8223. 2012, pages. DOI: 10.1117/12.908987.

[13] Tyler Harrison and Roger J Zemp. "Coregistered photoacoustic-ultrasound imaging applied to brachytherapy." In: *Journal of biomedical optics* 16.8 (Aug. 2011), p. 080502. ISSN: 1560-2281. DOI: 10.1117/1.3606566.

[14] Tyler Harrison, Peng Shao, and Roger J. Zemp. "S-sequence spatial coding for iterative multiple illumination photoacoustic tomography". Manuscript submitted for publication (Journal of Biomedical Optics, 140294P). 2014.

Chapter 2

Background

2.1 Ultrasound imaging

Ultrasound imaging is a clinical modality that most people are quite familiar with. It has become a very important tool due to its low cost, non-invasiveness, safety, and portability. In addition to its uses in prenatal care, ultrasound can be used to image just about any part of the body. Some examples include kidney, heart, liver, muscular, ocular, prostate, breast, and thyroid imaging. Higher powered ultrasound can even be used to non-invasively destroy tissue, which has applications for everything from destroying kidney stones (a relatively common procedure called lithotripsy) to potentially non-invasively treating brain tumors [1]. Ultrasound imaging is also used intraoperatively, for example for guidance in prostate brachytherapy [2]. Brachytherapy refers to the implantation of small radioactive sources in the tumor region to provide a localized dose.

Image formation in ultrasound varies from very simple to rather complicated. With simple geometric focusing, via a curved transducer face or acoustic lens, a single ultrasound pulse will give you an image of the beam area, coming to maximum gain in the focal volume. This image is called an A-line.

Many of these A-lines can be put together to form a B-scan (two-dimensional slice), C-scan (2D en-face image), or three-dimensional image. However, when one pictures a typical ultrasound imaging system, they picture a handheld transducer that accomplishes imaging without any motion. These are linear array transducers, composed of many transducer elements arranged in a line. Perpendicular to the array (in the elevation direction), these transducers are focused geometrically, but along the line (in the lateral direction), image reconstruction techniques are used to provide focusing in a larger area. For each point in an image, received data can be delayed and summed such that the image is focused at that point. So, a single two-dimensional image can be formed with focusing throughout the entire volume from one interrogation. Typically, ultrasound systems will use several transmit events focused in different areas to obtain a few scanlines at a time to increase image quality.

From a slightly more technical perspective, ultrasound imaging is analogous to optical imaging in many ways: focusing, numerical aperture, depth of field, and even diffraction limitations apply. Ultrasound transducers have a characteristic bandwidth, and transmission of the interrogating pulse is typically done at the center frequency of the transducer. This frequency can be used to calculate the diffraction limit, and thus the maximum achievable resolution very similar to optical imaging, though the formulae are not identical. In ultrasound imaging with a linear array, there are actually three different focusing parameters: lateral resolution along the transducer face (determined by electronic focusing), elevational resolution (determined by the geometric focusing), and axial resolution (determined by transducer bandwidth). Lateral and elevational resolution are very similar to optical focusing and are determined by the frequency used for imaging, whereas axial resolution is more like a time-gated measure of the transducer's impulse response. Both ultrasound and optical imaging systems are typically considered as linear systems, where

there is some sort of characteristic response of the imaging system that will 'blur' the object function [3]. This means that for certain geometries, similar reconstruction techniques can be used. For example, filtered backprojection is a reconstruction technique that is common in x-ray computed-tomography imaging, and can also be applied to ultrasound tomography [4]. One complicating factor in ultrasound is that the speed of sound in tissue is non-uniform. While this is somewhat of a problem in imaging, it can also provide useful diagnostic information such as bone density measurements [5].

2.2 The photoacoustic effect

Alexander Graham Bell first demonstrated the photoacoustic effect in 1880. As the name implies, it is the conversion of light into sound. The particular mechanism of this is that incident light is absorbed by optically absorbing materials, causing local heating. This heating, and the successive cooling creates a longitudinal wave originating from the absorbing material. These waves can be detected acoustically.

The content of these waves in terms of frequency is in part determined by the time of excitation, and the amplitude by the strength of the incident light. For efficient photoacoustic signal generation, the pulse of light must meet thermal and stress confinement conditions. Thermal confinement states that the temperature change in a voxel (the smallest area that can be imaged) must not diffuse out of the voxel during the pulse. Stress confinement requires that the mechanical waves not propagate out of the voxel during the pulse. For typical clinical ultrasound frequencies, the required pulse duration is in the < 100ns range [6]. In addition to ultrasonic frequency and strength of illumination. A sample of tissue can be considered as an assortment of optical absorbers, or chromophores. Each species of chromophore has its own absorption spectrum.

If a broadband light source is used, many chromophores will absorb well, obfuscating the image. If a single wavelength is used then the number of species seen in the final image can be limited. As water is present in all biological tissues, it is desirable to limit its absorption relative to other species. It turns out that there is a window in the visible to near infrared range where substances such as hemoglobin, melanin, and even lipids are more highly absorbing than water. Dyes are also available that absorb in this range. So, the characteristics of a light source required for photoacoustic imaging are: short pulse duration, high intensity, and in the visible to near-infrared range. Suitable sources are primarily high pulse energy lasers.

2.3 Photoacoustic imaging

The basics of photoacoustic imaging are very similar to ultrasound imaging, and utilize similar setups. The obvious complication is the addition of light delivery. This hurdle has been tackled in several ways, with varying physical setups. While light can be delivered from an angle directly onto the sample for most systems, this can lead to non-uniformity in fluence, large signals from melanin in the skin (which is typically undesirable), and tends to make setups difficult to work with. There are three loose categories of photoacoustic systems that offer different solutions to the problem of light delivery, as shown in figure 2.1.

- Scanning systems, consisting of a single element transducer scanned in one or two dimensions. A typical light-delivery setup is a dark-field confocal design, where light is directed around the transducer, and reflected to come to a focus co-incident with the transducer focus (Chapter 3)[7]. geometries. The more practical versions of these will couple one or more light paths (either fiber [10] or free space [11, 12]) to deliver light on one

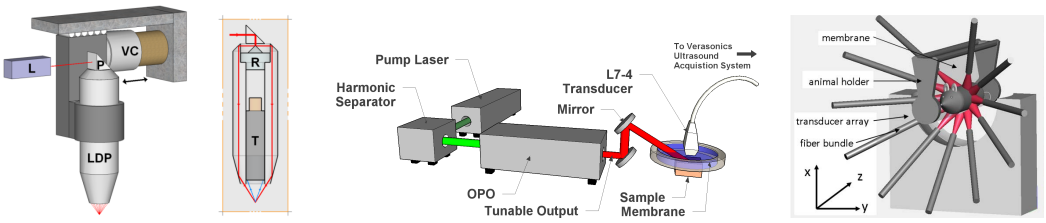

Figure 2.1: Images of a fast-scanning probe (left) [7], typical array system setup (center) [8] and tomographic system [9] (right, reprinted with permission from [Andreas Buehler et al. "Video rate optoacoustic tomography of mouse kidney perfusion". In: Optics Letters 35.14], copyright OSA 2010).

or more side. In this case, a large illumination area is desired such that the entire field of view can be covered.

- Linear array systems, which have the advantage of forming an image from a single laser pulse (Chapter 4).

- Tomographic systems, which are typically half-circle or hemi-spherical arrays of transducers. Light delivery can be accomplished using a fiber or other light guide to inject light at an angle [9], or in a different plane [13].

All of these systems have slightly different uses. Scanning systems are inexpensive to set up, and easy to use in terms of image reconstruction, since single A-lines can be stacked together. However, this style of system only provides focusing in a small volume, is susceptible to motion artifacts, and requires multiple laser shots per image. Focusing can be aided by the use of annular-array transducers [14], and motion artifacts can be limited by keeping motor speed low, but the requirement for multiple laser shots is fundamental. Typical systems require hundreds of laser shots to form a single image. To perform clinically relevant measurements in human tissue, about 50mm of imaging depth is desirable. Laser systems capable of outputting the energy required for photoacoustic imaging operate at up to 1 kHz or so, which would

only allow around 10 frames per second, which is unsuitable for many photoacoustic applications. In terms of usability, scanned systems are difficult to make handheld because the transducer, moving parts, and an acoustic coupling medium would have to be completely enclosed. This style of handheld transducer has not been made, and would likely produce poor-quality images due to vibrations.

Array systems have the advantage of forming a single image from a single laser shot, with focusing in the whole image area, and no mechanical scanning. There are, however, some tradeoffs for this. The first is computational complexity. Images need to be reconstructed based on data. This can be done with current hardware at hundreds of frames per second in realtime, but by capturing raw data and post-processing it, higher frame rate images can be achieved. Even capturing raw data is much more difficult than the single-element case. Instead of a single channel, array systems require data from multiple channels at once. For a linear array, 128 or 256 element setups are common. Most ultrasound systems are actually only capable of capturing a few channels at once, though research systems are currently available with up to 128 channels for a price. Compared to a scanned single-element system, array systems are much more costly due to the increased hardware and software required. Nevertheless, photoacoustic array systems are an attractive prospect, and many even use handheld transducers similar or identical to those used in clinical systems today [11, 15, 12].

2.4 Image reconstruction

2.4.1 Delay and sum beamforming

Delay and sum beamforming is based on simple geometry. For each point at which an image is to be reconstructed, ultrasound data are appropriately

delayed based on the speed of sound, and summed in order to form a focused image at that point. After summation envelope detection is applied to eliminate negative pressures. In older ultrasound systems, the delays were often implemented in hardware. These systems are also limited to reconstruction of only a few image lines simultaneously, and typically used only a subset of the elements for focused transmission at a time. Thanks to rapid advancements in computational power, ultrasound systems today can provide high-quality reconstructed images at hundreds of frames per second. Most commercial ultrasound systems use delay-and-sum beamforming due to its relative simplicity, and can be adapted with relative ease for photoacoustic imaging, as explored in Chapter 6 [16].

This algorithm suffers from poor performance in the near-field, which can be ameliorated by using fixed f-number reconstruction. The f-number, defined as $f_{\#} = \frac{f}{D}$ where f is the focal length and D is the transducer diameter, can be kept constant for small distances from the array by limiting the number of elements used in reconstruction. Effectively, as one reduces f by choosing points closer to the transducer face, one also reduces D by reducing the number of elements being used. Typically, to avoid excessive artifacts, $f_{\#} > 1$ is used. This has the unfortunate side effect of worsening the resolution. Additional windowing functions (i.e. gaussian) are also sometimes used in order to suppress sidelobe levels, improving resolution at the expense of signal-to-noise ratio.

As mentioned previously, ultrasound imaging often uses multiple focused transmit events to boost image quality. Due to the scattering nature of biological tissues, a focused transmission is not possible deep in tissue. In photoacoustic imaging, the incident light can be thought of as a plane wave that occurs instantaneously, meaning that the travel time for propagation through the sample need only be considered in one direction. However, for very shal-

low depths (less than one transport mean free path) photons can be considered ballistic, and images can be formed with very fine resolution defined by optical spot size in a technique called optical resolution photoacoustic microscopy (OR-PAM) [17].

2.4.2 Backprojection

Backprojection is a useful reconstruction technique that offers excellent image quality with the right transducer geometry. In x-ray computed tomography, backprojection is essentially the process of projecting the integral of the energy (data measured by the x-ray sensors) back along the sensor area (i.e. the locations where the energy could have been absorbed) and adding it all up to create an image. In photoacoustic imaging, temporal pressure recordings are backprojected rather than spatial projections [18, 19]. Modified backprojection provides exact reconstruction of initial pressure distributions in enclosed spherical geometries, infinite cylindrical or infinite planar geometries given adequate sampling [20, 19, 21].

2.4.3 Data-dependant methods

In the ultrasound field, much of the newest research in reconstruction algorithms fall under the classification of data-dependent. The general idea is that by doing some statistics on the data before summation, sidelobe levels can be suppressed, eliminating image artifacts at the cost of either signal-to-noise ratio or resolution. Two of these methods are known as short-lag spatial coherence beamforming (SLSC), and minimum variance (capon) beamforming.

SLSC beamforming is fairly straightforward. A spatial coherence function is generated across the transducer face for a particular set of delayed data and integrated up to some threshold. With this technique, resolution tends to be lower with lower integration thresholds, but it provides better signal-

and contrast-to-noise ratios. This is a result of the reduction of clutter in ultrasound by the reduction of incoherent off-axis echoes at the expense of some signal energy [22].

Minimum variance beamforming is an algorithm that is applicable to narrow-band RADAR arrays. Essentially, an analytic solution to selecting weighting factors based on minimizing the variance across delayed data is used before summation. It is not inherently numerically stable as it depends on the inversion of a data-dependent matrix, so some tricks such as diagonal loading are used to ensure that the technique will always give results at the expense of image quality. Some groups have had success in adapting it to ultrasound imaging, either by applying it on the broadband signal [23] or dividing the signal into narrow bands [24]. While Holfort et al. have shown that sub-wavelength resolution is possible with the sub-band method [25], those results have yet to be repeated by any other group. Nonetheless, even the more moderate performance improvements have been worth pursuing for many researchers.

2.4.4 Quantitative techniques

One of the attractive features of photoacoustic imaging is the possibility of performing functional imaging. Due to the differing absorption spectra of hemoglobin in its oxygenated and deoxygenated states, imaging at multiple wavelengths permits the formation of images showing concentrations of the two species. Using these images, one can measure blood oxygenation, and by measuring the oxygenation states of blood entering and exiting a region of interest, information about oxygen consumption can be gathered. While this is a simple idea in principle, in practice it is quite challenging. The basic idea behind photoacoustic imaging is explained by the simple equation below:

$$p_0 = \mu_a \Phi \Gamma \tag{2.1}$$

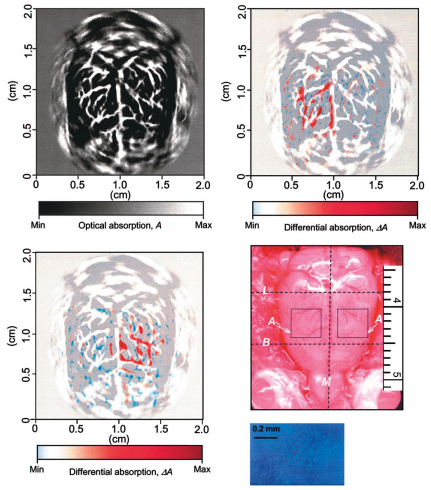

Figure 2.2: Functional imaging with photoacoustic tomography (PAT). **Top left:** PAT image of rat brain, **Top right:** Functional image under left whisker stimulation and **Bottom left:** right whisker stimulation. **Bottom right:** Photograph of rat brain. (Figure reprinted by permission from Macmillan Publishers Ltd: Nature Biotechnology [Xueding Wang et al. "Noninvasive laser-induced photoacoustic tomog- raphy for structural and functional in vivo imaging of the brain". eng. In: Nature Biotechnology 21.7 (2003), pp. 803–806], copyright 2003)[13]

Where p_0 is the initial pressure distribution, μ_a is the spatially varying optical absorption coefficient, Φ is the spatially varying fluence, and Γ is the Green's function, or Grüneisen coefficient, which can be considered a sort of transfer function between energy absorption and initial pressure. While all of the contributors to the initial pressure distribution are technically spatially varying, Γ is often considered to be a constant, but that is not strictly true as it relates to the material properties of the imaging subject.

The first difficulty in extracting quantitative information is the accurate recovery of p_0. This is covered somewhat in Section 2.4, but there are some compounding effects to consider. Firstly, reconstruction techniques typically assume a well-known, uniform speed of sound. This is not the case in biological tissues, and even a small perturbation can greatly impact the accuracy. In the case where metals are introduced, reconstruction will suffer due to the extreme difference in speed of sound: around 5000 m/s compared to the ∼1540 m/s

assumed in biological tissue. Even within tissues, speed of sound can vary from 1450 m/s in fat, up to 4080 m/s in bone [26]. It thus becomes very difficult to create an accurate image. Ultrasound techniques do exist to measure speed of sound, which may be able to account for this [27]. There are other ultrasound concerns such as transducer response and geometry that are best addressed using a tomographic system, which can achieve ideal reconstruction for a well-designed setup [28].

The next challenge is to take p_0, and recover some optical information, which may be μ_a, μ_s' (the reduced scattering coefficient), or even Γ. With sufficient information (i.e. multiple wavelengths or multiple illumination angles), all three may be recovered simultaneously [29]. Recovering μ_a is often the end goal in quantitative reconstruction in order to perform the spectral unmixing required to measure concentrations of chromophores. This is quite tricky, since Φ can vary greatly within tissue, as it is affected by not only μ_a, but also μ_s'. Some recent approaches to this sort of recovery have combined techniques like Diffuse Optical Tomography (DOT) to estimate bulk optical properties (in the form of μ_a and μ_s) with photoacoustic imaging in order to inform reconstruction [30]. Iterative techniques are also common, using models of optical absorption and light diffusion in order to obtain quantitative data. However, these techniques are often numerically unstable [31], and difficult to implement in practice due to the complexity of properly modeling biological tissues.

Apart from the task of system setup, the accurate representation of optical properties is the most important limitation of photoacoustic imaging that this thesis attempts to address. More information on our iterative quantitative techniques is available in Chapters 7 and 9.

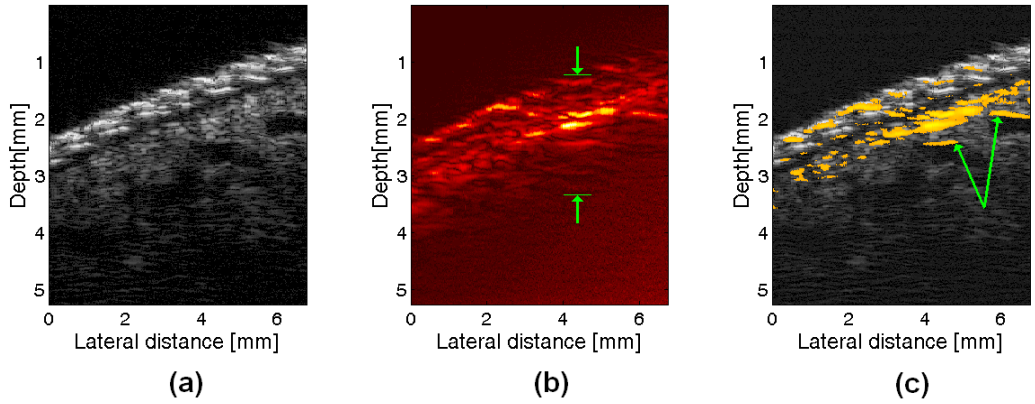

Figure 2.3: High-frequency fast-scanned (a) ultrasound, (b) photoacoustic (with imaging depth indicated), and (c) combined (with blood vessels indicated) images of a human finger. [7]

2.5 Applications of photoacoustic imaging

2.5.1 Vascular mapping

One of the main areas of interest for photoacoustic imaging has been the ability to visualize vasculature, shown in concept in figure 2.3. This has immediate applications in cancer detection. Cancers often develop tortuous vessel networks that feed their rapid growth by stimulating a process called angiogenesis. These will result in a bright region of increased blood volume on low-resolution photoacoustic systems, but with higher frequency transducers, it is possible to image down to the microvasculature, potentially on the order of hundreds of microns at multiple centimeter depths [12]. Mapping blood vessel networks can be used as a diagnostic tool for clinicians to assess the nature of tumors.

2.5.2 Functional imaging

Another common feature of cancerous tumors is that they will often develop a necrotic core, exhibiting regions of both hyperoxia and hypoxia. At a single wavelength, it is impossible to positively identify these regions. Thus, multiple

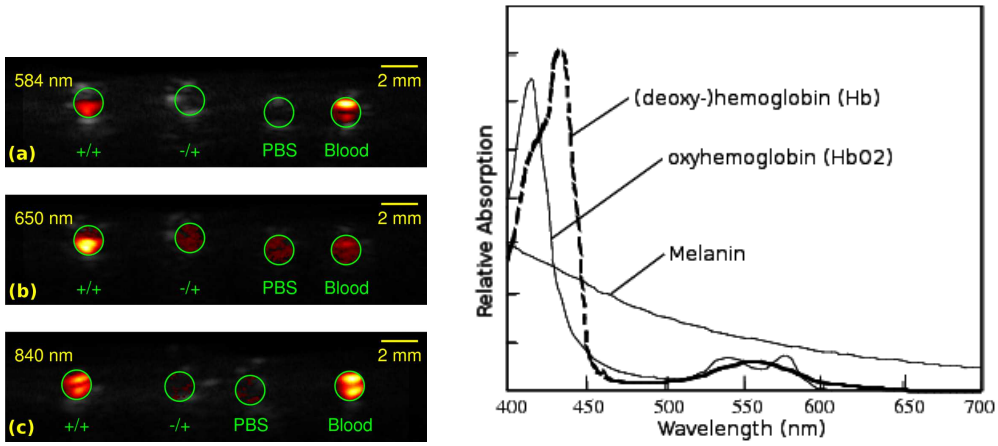

Figure 2.4: **Left:** (a) Photoacoustic images overlaid on ultrasound at (a) 584, (b) 650, and (c) 840 nm of melanin-expressing cells compared to control cells, phosphate-buffered saline, and blood. See Chapter 11 [8] for more information. **Right:** Optical absorption of several species.

wavelengths are used to perform functional imaging. Functional imaging aims to examine blood oxygenation states, and ideally quantitatively map oxygen consumption. This has long been the domain of fMRI, which has proven to be a valuable tool for studying things like brain function and metabolic processes. However, unlike photoacoustic imaging, fMRI is only sensitive to changes in deoxyhemoglobin, and struggles to estimate oxygenation in small vessel networks.

2.5.3 Contrast agents

While significant attention has been paid to imaging blood, other endogenous pigments and tissues have been used for photoacoustic imaging, such as melanin shown in figure 2.4. Lipid imaging is also being explored, though the wavelengths required for this are closer to 1210 nm [32]. So far, this discussion has focused only on intrinsic contrast agents, but extrinsic contrast agents in the form of optical dyes are also quite promising. Perhaps the most appealing varieties of these are dyes that are already FDA approved for human use, such as indocyanine green (ICG) and methylene blue, both of which have shown

promise as photoacoustic contrast agents [9, 33]. Methylene blue is routinely used to label sentinel lymph nodes to allow surgeons to see them during a procedure to extract them for biopsy. Using photoacoustic imaging, Erpelding et al. have managed to extract biopsy samples from a rat by guiding a needle to the labelled lymph node [33], greatly reducing the invasiveness of the biopsy procedure.

New dual-mode contrast agents for ultrasound and photoacoustic imaging have also been developed by Wilson et al. [34] that take advantage of the optical absorption of nanoparticles in order to create microbubbles out of nano-scale droplets of heavy gasses such as perfluoropentane mixed with optically absorbing nanoparticles. These have the advantage of size over microbubbles, such nanodroplets can accumulate in tumors where microbubbles cannot. While nanodroplets can be activated using only ultrasound, the acoustic pressure required to do so is beyond most imaging systems. Numerous other dyes and contrast agents have been explored or are emerging, including plasmonic nanoparticles [35], porphysomes [36], and fluorescent proteins [37].

2.5.4 Needle guidance

Needle biopsies are often currently performed under ultrasound guidance, but the huge mismatch in mechanical properties between the needles and the surrounding tissues causes reverberation artifacts that degrade image quality. Additionally, imaging the needle at an angle can be quite challenging, as incident waves are reflected away from the transducer face. As it turns out, metallic objects exhibit a large photoacoustic response as shown in in figure 2.5 [38]. The pressure waves resulting from photoacoustic imaging do not suffer from the same reverberation and off-axis signal problems since the induced acoustic waves radiate in all directions. Photoacoustic imaging has shown some promise in this regard as well [39]. While metallic objects are typically

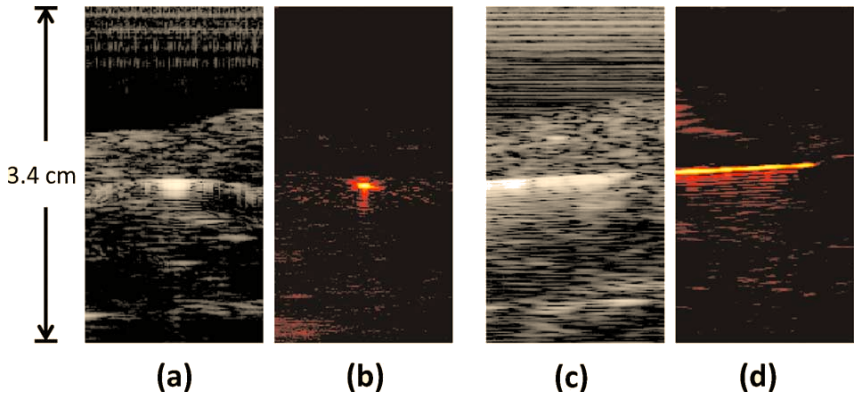

Figure 2.5: (a), (c) Ultrasound and (b), (d) photoacoustic images of metal needle (a), (b) cross-section axially, and (c), (d) cross-section laterally. (Reprinted with permission from [Jimmy Su et al. "Photoacoustic imaging of clinical metal needles in tissue." In: Journal of biomedical optics 15.2 (2010), p. 021309] copyright SPIE 2010.)[38]

considered quite refelctive, 10% or more of incident energy may be absorbed by the metal. Metals also may exhibit a higher Grüneisen parameter than tissue, but that has yet to be verified in the literature.

2.6 Alternatives to photoacoustic imaging

2.6.1 Ultrasound

Ultrasound is the most directly comparable imaging technology to photoacoustic imaging in that much of the physical equipment is identical. However, the contrast mechanism is mechanical rather than optical. While mechanical contrast agents exist, largely in the form of microbubbles, multiple species cannot be distinguished from one another. That is to say that while spectral unmixing can yield images of different chromophores in photoacoustic imaging, the same cannot be done in ultrasound. Ultrasound images also often suffer from high levels of speckle, though some techniques exist to suppress this noise. Nonetheless, ultrasound has clear advantages in terms of cost and availability to clinicians, and has become an important diagnostic tool. Ad-

vanced imaging modes such as Doppler imaging allow ultrasound to visualize blood flow, and even quantitatively measure flow velocity. Studies have even demonstrated functional imaging, even in mouse brains [40].

Contrast ultrasound techniques have shown increased contrast for some imaging applications, but microbubble agents typically have a very short longevity in tissues, requiring readministration of the contrast agent for extended studies [41]. Ultrasound imaging is fundamentally limited to half the frame rate of photoacoustic imaging due to the two-way travel required, but practically speaking, frame rates of hundreds to thousands of frames per second are possible with current technology.

Ultrasound can also be limiting in surgical procedures such as brachytherapy, which ends up requiring pre- and post-operative imaging. The first step is a CT scan tumor growth and placement relative to internal structures. A radiologist will design a treatment plan based on these images. The patient is imaged with ultrasound and the same identification of internal structures is performed as was done during CT imaging. The surgeon then inserts a series of needles containing the seeds, marking their locations on the ultrasound images. This is a technique that requires some amount of skill in both accounting for tissue deformation and interpreting the ultrasound image. After the procedure is completed, the dosimetry is calculated for the tumor area based on the surgeon's identification of seeds, and if necessary some small modification of the treatment can be done in the operating room. After this the patient is typically imaged again with CT, and may have to undergo the procedure again to adjust the dosage to the affected area. This form of treatment is less invasive than surgical procedures and requires fewer clinical visits than traditional radiotherapy. However, there is some difficulty with visualizing these seeds intraoperatively (arising from off-axis reflections in ultrasound), and additional CT imaging is undertaken post-operatively to verify that the

treatment was successful. CT imaging is much better at localizing brachytherapy seeds. In extreme cases, this may require a second procedure to implant additional seeds. This has led to the investigation of other techniques such as CT imaging for intraoperative use in order to avoid extra implantation sessions [42].

In many circumstances, photoacoustic imaging systems allow ultrasound acquisition concurrent with photoacoustic imaging, allowing for both modes to be used at the same time. The two image types provide complementary information allowing visualization of both structural and optical contrast.

2.6.2 MRI

Magnetic resonance imaging (MRI) uses radio-frequency modulated magnetic fields in order to image polar molecules in the presence of a large static magnetic field. In the human body, the most prolific polar molecule is water. Contrast arises from different materials interacting with water in different ways which modifies the relaxation time, or the time that it takes the water molecules to return to alignment with the static magnetic field. The process of relaxation gives off electromagnetic radiation which can be detected by coils. Ultimately, this can provide excellent resolution at the expense of imaging time. There are some contrast agents available for MRI, typically gadolinium or iron oxide based that act to reduce the relaxation time [43].

There are actually three different relaxation times that can be measured: T_1 which measures the exponential decay factor for the time it takes for the nuclear spin to recover in the direction of the static magnetic field; T_2 which measures the exponential decay factor for the time it takes the spin to recover in the direction perpendicular to the applied field; and T_2^* which measures the effect of local chemistry on magnetic field inhomogeneity. By examining the different relaxation times, it is possible to achieve some level of species

identification [44].

One intrinsic source of contrast that is important for a comparison with photoacoustic imaging is deoxyhemoglobin which alters the T_2^* relaxation time. This is used in an imaging technique called blood-oxygen level dependent (BOLD) MRI, which forms the basis for functional MRI (fMRI). Essentially, low-resolution MR images are taken frequently, and the T_2^* relaxation time measured. Any differences in T_2^* indicate a change in blood oxygenation. The net effect of deoxyhemoglobin is a reduction in MR signal. When neural activity increases in an area of the brain, the proportion of oxyhemoglobin in that area will also increase due to the vascular response leading to an increase in signal. The advantage of fMRI over functional photoacoustic imaging is that it can easily be used deep in brain tissue. However, fMRI can also be misleading since BOLD imaging is only sensitive to deoxyhemoglobin, and thus an increase in blood volume in an area will be detected as a decrease of blood oxygenation. MRI also requires bulky, costly equipment. The major advantages that MRI has over photoacoustic imaging is the ability to image at an excellent resolution deep in the body, including in the brain where photoacoustic imaging is quite challenging due to the optical and acoustic properties of the skull, though important advances are also being made [45].

2.6.3 X-ray computed tomography

X-ray computed tomography (CT) is another common medical imaging modality. It uses a rotating x-ray source with a number of detectors arranged in a circle around the imaging subject in order to capture photons transmitted through the subject. Collected data are used to reconstruct 2 or 3 dimensional images. CT is well suited for some imaging tasks, though soft tissue often suffers from poor delineation. CT can provide good imaging resolution, but it is typically not well-suited for intraoperative use due to the bulky imaging setup

and relatively poor temporal resolution. The most important concern about CT imaging is the use of ionizing radiation, though more recent imaging and reconstruction techniques often feature a much lower dose.

2.6.4 Others

There are other optical techniques that also attempt to recover optical properties. In general, techniques like diffuse optical tomography (DOT), optical coherence tomography (OCT), and near-infrared spectroscopy perform poorly at any significant depth. These depend on ballistic photons, and thus the high scattering coefficient of tissue prevents imaging beyond about 1mm without resolution degradation far beyond the level that photoacoustic imaging provides.

Other medical imaging techniques do exist, such as positron emission tomography (PET) and EPRI (electron paramagnetic resonance imaging). PET uses a radioactive tracer which emits a positron, causing an eventual annihilation event and paired photons to be emitted. Since this tracer is a glucose analogue, PET is useful for highlighting areas of high metabolic activity. This is primarily used for imaging metastasis in cancers, but the radiation exposure is higher than techniques like CT imaging. EPRI is capable of imaging free radicals or transition metal complexes [46], but these may have toxic effects. Both of these can provide functional imaging, but depend on potentially dangerous external contrast agents to do so - which motivates the study of photoacoustic imaging.

References

[1] B Larrat et al. "MR-guided transcranial brain HIFU in small animal models." In: *Physics in medicine and biology* 55.2 (Jan. 2010), pp. 365–88. ISSN: 1361-6560. DOI: 10.1088/0031-9155/55/2/003.

[2] Ben H. Han et al. "Prostate brachytherapy seed identification on post-implant TRUS images". In: *Medical Physics* 30.5 (2003), p. 898. ISSN: 00942405. DOI: 10.1118/1.1568976.

[3] R.J. Zemp, C.K. Abbey, and M.F. Insana. "Linear system models for ultrasonic imaging: application to signal statistics". In: *Ultrasonics, Ferroelectrics and Frequency Control, IEEE Transactions on* 50.6 (June 2003), pp. 642–654. ISSN: 0885-3010. DOI: 10.1109/TUFFC.2003.1209551.

[4] A Devaney. "A filtered backpropagation algorithm for diffraction tomography". In: *Ultrasonic Imaging* 4.4 (Oct. 1982), pp. 336–350. ISSN: 01617346. DOI: 10.1016/0161-7346(82)90017-7.

[5] C.F Njeh et al. "Assessment of bone status using speed of sound at multiple anatomical sites". In: *Ultrasound in Medicine & Biology* 27.10 (Oct. 2001), pp. 1337–1345. ISSN: 03015629. DOI: 10.1016/S0301-5629(01)00437-9.

[6] M Xu and L.V. Wang. "Photoacoustic imaging in biomedicine". In: *Review of Scientific Instruments* 77.4041101 (2006), pp. 1–22.

[7] Tyler Harrison et al. "Combined photoacoustic and ultrasound biomicroscopy". In: *Optics Express* 17.24 (2009), pp. 22041–22046. DOI: 10.1063/1.2195024.2..

[8] Tyler Harrison, Robert J. Paproski, and Roger J. Zemp. "In vivo imaging of inducible tyrosinase gene expression with an ultrasound array-based

photoacoustic system". In: vol. 8223. 2012, pages. DOI: 10.1117/12.908987.

[9] Andreas Buehler et al. "Video rate optoacoustic tomography of mouse kidney perfusion". In: *Optics Letters* 35.14 (July 2010), p. 2475. ISSN: 0146-9592. DOI: 10.1364/OL.35.002475.

[10] Roger J Zemp et al. "Photoacoustic imaging of the microvasculature with a high-frequency ultrasound array transducer". In: *Journal of biomedical optics* 12.1 (2007), p. 010501. ISSN: 1083-3668. DOI: 10.1117/1.2709850.

[11] Suhyun Park, Salavat R Aglyamov, and S. Emelianov. "Beamforming for Photoacoustic Imaging Using Linear Array Transducer". In: *IEEE Ultrasonics Symposium Proceedings*. Vol. 1. IEEE, Oct. 2007, pp. 856–859. ISBN: 978-1-4244-1383-6. DOI: 10.1109/ULTSYM.2007.219.

[12] Tyler Harrison and Roger J. Zemp. "Interlaced realtime channel-domain photoacoustic and ultrasound imaging". In: *Proceedings of SPIE*. Vol. 7899. 2011, pages. DOI: 10.1117/12.875507.

[13] Xueding Wang et al. "Noninvasive laser-induced photoacoustic tomography for structural and functional in vivo imaging of the brain". eng. In: *Nature Biotechnology* 21.7 (2003), pp. 803–806. ISSN: 1087-0156.

[14] Huihong Lu et al. "Improved depth-of-field photoacoustic microscopy with a custom high-frequency annular array transducer". In: *Proceedings of SPIE*. Vol. 7899. 2011, pages. DOI: 10.1117/12.875601.

[15] Chulhong Kim et al. "Deeply penetrating in vivo photoacoustic imaging using a clinical ultrasound array system". In: *Biomedical Optics Express* 1.1 (July 2010), pp. 278–284. ISSN: 2156-7085. DOI: 10.1364/BOE.1.000278.

[16] Tyler Harrison and Roger J Zemp. "The applicability of ultrasound dynamic receive beamformers to photoacoustic imaging." In: *IEEE transactions on ultrasonics, ferroelectrics, and frequency control* 58.10 (Oct. 2011), pp. 2259–63. ISSN: 1525-8955. DOI: 10.1109/TUFFC.2011.2076.

[17] Konstantin Maslov et al. "Optical-resolution photoacoustic microscopy for in vivo imaging of single capillaries". In: *Optics Letters* 33.9 (2008), pp. 929–931.

[18] Robert A. Kruger et al. "Photoacoustic ultrasound (PAUS)-Reconstruction tomography". In: *Medical Physics* 22.10 (1995), pp. 1605–1609. DOI: 10.1118/1.597429.

[19] Lvming Zeng et al. "High antinoise photoacoustic tomography based on a modified filtered backprojection algorithm with combination wavelet". In: *Medical Physics* 34.2 (2007), pp. 556–563. DOI: 10.1118/1.2426406.

[20] Minghua Xu and Lihong Wang. "Universal back-projection algorithm for photoacoustic computed tomography". In: *Physical Review* 71.016706 (Jan. 2005), pp. 1–7. ISSN: 1539-3755. DOI: 10.1103/PhysRevE.71.016706.

[21] Daniel Razansky, Claudio Vinegoni, and Vasilis Ntziachristos. "Multispectral photoacoustic imaging of fluorochromes in small animals". In: *Opt. Lett.* 32.19 (Oct. 2007), pp. 2891–2893. DOI: 10.1364/OL.32.002891.

[22] Muyinatu a. Lediju et al. "Short-lag spatial coherence imaging". In: *2010 IEEE International Ultrasonics Symposium*. IEEE, Oct. 2010, pp. 987–990. ISBN: 978-1-4577-0382-9. DOI: 10.1109/ULTSYM.2010.5935711.

[23] Babak Mohammadzadeh Asl and Ali Mahloojifar. "Minimum variance beamforming combined with adaptive coherence weighting applied to medical ultrasound imaging." In: *IEEE transactions on ultrasonics, fer-*

roelectrics, and frequency control 56.9 (Sept. 2009), pp. 1923–31. ISSN: 1525-8955. DOI: 10.1109/TUFFC.2009.1268.

[24] I K Holfort, F Gran, and J A Jensen. "Plane wave medical ultrasound imaging using adaptive beamforming". In: *Sensor Array and Multichannel Signal Processing Workshop, 2008. SAM 2008. 5th IEEE*. July 2008, pp. 288–292. DOI: 10.1109/SAM.2008.4606874.

[25] IK Holfort, Fredrik Gran, and JA Jensen. "Broadband minimum variance beamforming for ultrasound imaging". In: *IEEE Transactions on Ultrasonics, Ferroelectrics and Frequency Control* 56.2 (2009), pp. 314–325.

[26] Haim Azhari. "Appendix A: Typical Acoustic Properties of Tissues". In: *Basics of Biomedical Ultrasound for Engineers*. John Wiley & Sons, Inc., 2010, pp. 313–314. ISBN: 9780470561478. DOI: 10.1002/9780470561478.app1.

[27] Ho-Chul Shin et al. "Ultrasound in medicine & biology". In: 36.4 (Apr. 1, 2010), pp. 623–636. ISSN: 0301-5629.

[28] Chi Zhang and Yuanyuan Wang. "Deconvolution reconstruction of full-view and limited-view photoacoustic tomography: a simulation study". In: *J. Opt. Soc. Am. A* 25.10 (Oct. 2008), pp. 2436–2443. DOI: 10.1364/JOSAA.25.002436.

[29] Guillaume Bal and Kui Ren. "Multi-source quantitative photoacoustic tomography in a diffusive regime". In: *Inverse Probl.* 27.7 (2011), p. 075003.

[30] Ben Cox et al. "Quantitative spectroscopic photoacoustic imaging: a review." In: *Journal of biomedical optics* 17.6 (June 2012), p. 061202. ISSN: 1560-2281. DOI: 10.1117/1.JBO.17.6.061202.

[31] Thomas Jetzfellner et al. “Performance of iterative optoacoustic tomography with experimental data”. In: *Applied Physics Letters* 95.1 (2009), p. 013703. ISSN: 00036951. DOI: 10.1063/1.3167280.

[32] Thomas J Allen et al. “Spectroscopic photoacoustic imaging of lipid-rich plaques in the human aorta in the 740 to 1400 nm wavelength range”. In: *Journal of biomedical optics* 17.6 (June 2012), p. 061209. ISSN: 1560-2281. DOI: 10.1117/1.JBO.17.6.061209.

[33] Todd N Erpelding et al. “Sentinel lymph nodes in the rat: noninvasive photoacoustic and US imaging with a clinical US system.” In: *Radiology* 256.1 (July 2010), pp. 102–10. ISSN: 1527-1315. DOI: 10.1148/radiol.10091772.

[34] Katheryne E Wilson, Kimberly A Homan, and Stanislav Y Emelianov. “Remotely triggered contrast nanoagent for ultrasound and photoacoustic imaging”. In: *2010 IEEE International Ultrasonics Symposium*. IEEE, Oct. 2010, pp. 1003–1006. ISBN: 978-1-4577-0382-9. DOI: 10.1109/ULTSYM.2010.5935757.

[35] Srivalleesha Mallidi et al. “Multiwavelength Photoacoustic Imaging and Plasmon Resonance Coupling of Gold Nanoparticles for Selective Detection of Cancer”. In: *Nano Letters* 9.8 (2009). PMID: 19572747, pp. 2825–2831. DOI: 10.1021/nl802929u.

[36] Jonathan F. Lovell et al. “Porphysome nanovesicles generated by porphyrin bilayers for use as multimodal biophotonic contrast agents”. In: *Nat Mater* 10.4 (Apr. 2011), pp. 324–332. ISSN: 1476-1122. DOI: 10.1038/nmat2986.

[37] Arie Krumholz et al. “Photoacoustic imaging of the near-infrared fluorescent protein iRFP in vivo”. In: vol. 8223. 2012, pages. DOI: 10.1117/12.908927.

[38] Jimmy Su et al. "Photoacoustic imaging of clinical metal needles in tissue." In: *Journal of biomedical optics* 15.2 (2010), p. 021309. ISSN: 1560-2281. DOI: 10.1117/1.3368686.

[39] Jimmy L Su et al. "Photoacoustic imaging of prostate brachytherapy seeds." In: *Biomedical optics express* 2.8 (Aug. 2011), pp. 2243–54. ISSN: 2156-7085. DOI: 10.1364/BOE.2.002243.

[40] Emilie Mace et al. "High sensitivity brain angiography using Ultrafast Doppler". In: *2010 IEEE International Ultrasonics Symposium*. IEEE, Oct. 2010, pp. 1194–1197. ISBN: 978-1-4577-0382-9. DOI: 10.1109/ULTSYM.2010.5935810.

[41] VR Stewart and PS Sidhu. "New directions in ultrasound: microbubble contrast". In: *British Journal of Radiology* 79 (2006), pp. 188–194. DOI: 10.1259/bjr/17790547.

[42] Donald B Fuller et al. "CT-ultrasound fusion prostate brachytherapy: A dynamic dosimetry feedback and improvement method. A report of 54 consecutive cases". In: *Brachytherapy* 4.3 (2005), pp. 207–216. ISSN: 1538-4721. DOI: 10.1016/j.brachy.2005.07.005.

[43] Peter Caravan. "Strategies for increasing the sensitivity of gadolinium based MRI contrast agents." In: *Chemical Society reviews* 35.6 (June 2006), pp. 512–23. ISSN: 0306-0012. DOI: 10.1039/b510982p.

[44] Chun Yuan et al. "Contrast-Enhanced High Resolution MRI for Atherosclerotic Carotid Artery Tissue Characterization". In: *Journal of Magnetic Resonance Imaging* 15 (2002), pp. 62–67. DOI: 10.1002/jmri.10030.

[45] Lun-De Liao et al. "Transcranial imaging of functional cerebral hemodynamic changes in single blood vessels using in vivo photoacoustic microscopy." In: *Journal of cerebral blood flow and metabolism : official journal of the International Society of Cerebral Blood Flow and*

Metabolism 32.6 (June 2012), pp. 938–51. ISSN: 1559-7016. DOI: 10.1038/jcbfm.2012.42.

[46] Murali C. Krishna et al. "Electron Paramagnetic Resonance for Small Animal Imaging Applications". In: *ILAR Journal* 42.3 (2001), pp. 209–218. DOI: 10.1093/ilar.42.3.209.

Chapter 3

Combined photoacoustic and ultrasound biomicroscopy

3.1 Introduction

The work in this chapter represents some early fundamental work into high-frequency photoacoustic (PA) imaging, motivating many in the field to pursue similar system designs for more advanced imaging techniques, such as OR-PAM [1].

Photoacoustic imaging provides optical absorption contrast with high depth-to-resolution ratios compared to other transport- and diffusion-regime optical imaging technologies [2]. It has attracted considerable attention in the recent literature due to its capacity for functional [3] and molecular imaging [4], and for imaging microvascular networks [5].

We have developed a hybrid photoacoustic (PA) and ultrasound (US) imaging system to provide ultrasonic B-mode images as a structural context

A version of this chapter has been published. Harrison et al. 2009. Optics Express. 17(24): 22041-22046.

for optical-contrast photoacoustic B-scans. While some groups have already combined ultrasound and photoacoustic imaging at diagnostic frequencies (2-15MHz) [6]; to our knowledge this has not been done at high ultrasound frequencies (>20MHz) for real-time scanning rates. High-frequency photoacoustic microscopy (PAM) has provided outstanding images of microvascular structures to depths of 2-3 mm in vivo [7]. Our hybrid imaging system operates at 25 MHz and offers real-time ultrasound imaging capabilities at a resolution and depth-scale comparable with PAM parameters. Additionally, the ultrasound and laser pulses are interlaced in our system, providing natural co-registration of the two complementary contrasts. We believe that the combined ultrasound and photoacoustic biomicroscopy system provides significant diagnostic value over either standalone modality. Moreover, the addition of micro-ultrasound to PAM may prove important considering the recent proliferation of articles utilizing high-frequency ultrasound for pre-clinical studies.

While real-time photoacoustic imaging has been developed using a high-frequency array transducer [8], high-frequency arrays are only now coming on the market and can be cost-prohibitive. Moreover, real-time photoacoustic systems developed thus far lack ultrasound structural context. We believe that a viable alternative to these systems may be based on fast-scanning single element transducers, since such systems have proved to be a workhorse in many pre-clinical ultrasound imaging studies [9]. Unfortunately to use fast-scanning systems for real-time photoacoustic imaging requires high-repetition-rate lasers which are also cost-prohibitive. Our approach is to develop a fast-scanning single-element transducer system capable of high-frame-rate ultrasound imaging coupled with a slower-scanning photoacoustic mode (with interlaced ultrasound and laser pulses), frame-rate limited by the pulse-repetition-rate of the laser. We anticipate that B-mode ultrasound may be used for localizing a region of interest then the photoacoustic mode may be invoked to retrieve

the optical contrast information in the desired location. While our future plan is to incorporate multi-wavelength photoacoustic imaging, the present study uses only a single optical wavelength at 532 nm. Our study shows that speckle-changes in ultrasound B-scans representing blood flow correlate with photoacoustic signatures - and that photoacoustic and ultrasound images each offer information that the sister modality cannot alone provide.

3.2 Method

3.2.1 Light delivery probe

We used a 532 nm pulsed laser (Ultra UL 421111, Big Sky Technologies, Bozeman, MT, USA) with a maximum pulse repetition rate of 20 Hz and pulse duration of 10 ns for this study. At the focus, the optical fluence was estimated as 20 mJ/cm2.

As shown in Figure 3.1, we developed a light delivery probe based on dark field illumination. A 25-MHz ultrasound transducer with a 12.7-mm focal length and 6-mm active aperture (V324-SM, Panametrics, Waltham, MA, USA) is mounted within the lower part of the probe. A down-looking right angle prism mounted above the acrylic probe (n = 1.46), which diverts the incident laser beam towards a 45° reflective cone to spread the light horizontally. The 45° polished surface of the probe reflects the horizontal light downward along the probe. Another polished face, machined at an angle smaller than the acrylic-water critical angle deflects light confocally around the transducer focal axis. Light is focused at ∼10.5 mm below the bottom of this probe. During setup, the ultrasound transducer position is adjusted vertically to match its focus point with the laser focus by maximizing the photoacoustic signal from the carbon fiber.

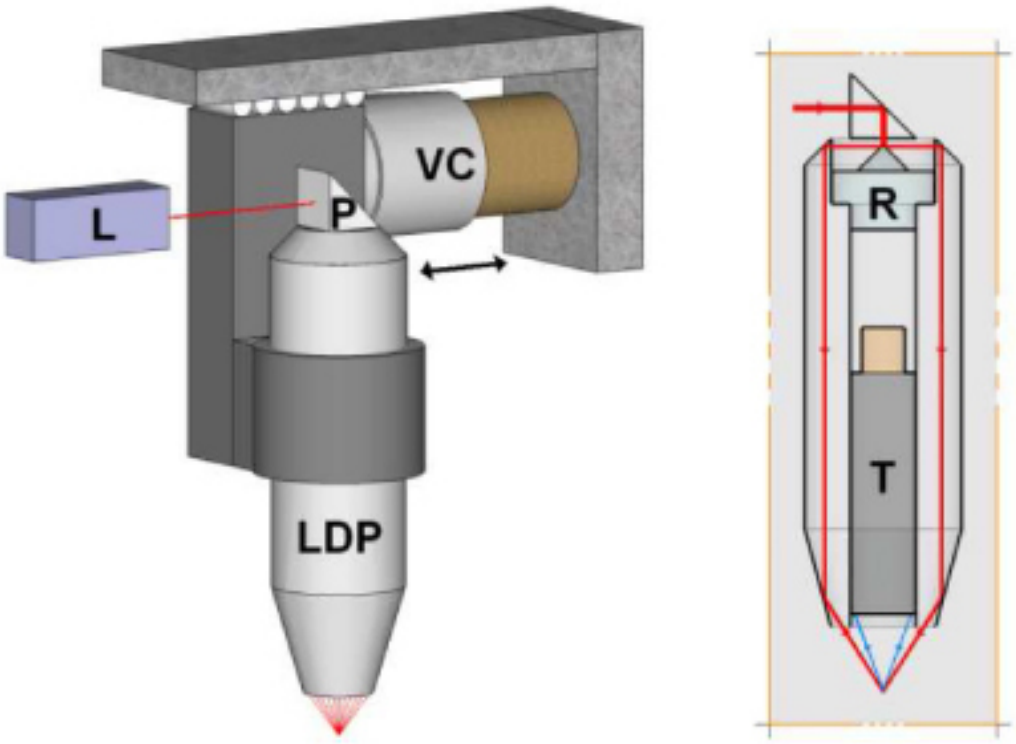

Figure 3.1: Voice coil (VC) US/PA scanning system and cross section of Light Delivery Probe (LDP). Incident light from laser (L) is diverted towards the reflective cone (R) by the prism (P). Ultrasound transducer (T) is mounted inside the LDP.

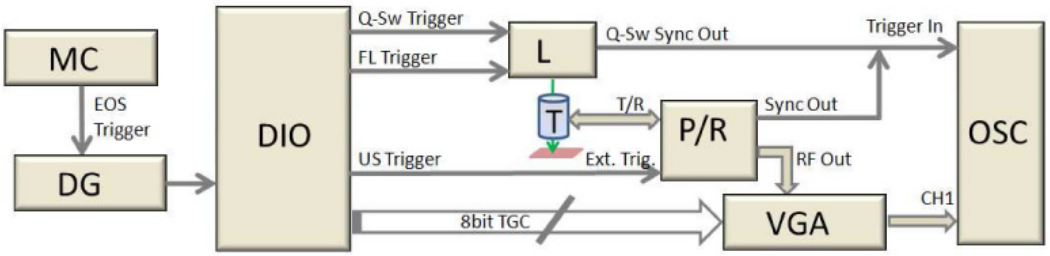

Figure 3.2: Combined ultrasound-photoacoustic system block diagram. MC: Motor Controller; DG: Delay Generator; DIO: Digital Input Output card; L: Laser; T: Ultrasound Transducer; P/R: Ultrasound Pulser/Receiver; VGA: Variable Gain Amplifier; OSC: Oscilloscope; Q-Sw: Q-Switch; FL: Flashlamp; EOS: End of Scan.

3.2.2 Fast scanning system

The combined ultrasound transducer and light probe is mounted on a voice-coil stage. This stage is driven by a programmed motor controller to achieve up to 10 Hz oscillations over ∼9mm, providing up to 20 imaging frames per second (higher rates are possible for shorter scan ranges). At present, our system provides three imaging modes: ultrasound mode, photoacoustic mode and interlaced ultrasound-photoacoustic mode. A system block diagram may be seen in Figure 3.2.

In the ultrasonic scanning mode, the motor controller (Elmo Harmonica HAR 5/60, Elmo Motion Control Inc., Nashua, NH, USA) drives the voice coil stage (VCS-10-023-BS-01, 1.0 inch travel, 2.3lbs continuous force, 6.9 lbs peak force, purchased from H2W technologies, Inc., Valencia, CA, USA) to oscillate at a fixed and desired scanning rate. A digital output bit from the motor controller is set to high for a short duration at the end of each scan trajectory. This end-of-scan trigger is used to mark the beginning of each image frame. This output event triggers a sequence of A-scan line trigger pulses which are generated by a digital input-output (DIO) card (NI PCI-6542, National Instruments Inc., Austin, TX, USA) and are sent to the ultrasound pulser-receiver (5703PR, Panametrics, Waltham, MA, USA). The ultrasound

pulser-receiver is capable of a repetition rate up to 10 kHz, with excitation energy up to 16 μJ. The pre-amplifier built into the pulser-receiver provides gain of up to 39 dB.

In the photoacoustic mode, the frame-rate is limited by the 20 Hz pulse repetition rate of the laser. Just as in the ultrasound mode, the end-of-scan causes the DIO card to generate a trigger sequence, this time for the laser flash-lamp trigger. However, there was an unacceptable jitter of multiple microseconds between the laser flash lamp trigger and the lasing output, so we also generate a pulse sequence for the laser's Q-switch trigger to reduce jitter to zero.

The variable-gain amplifier (VGA) is analog-voltage controlled via an 8-bit DAC (HI3338, Intersil, Milpitas, CA, USA) controlled by the DIO card. The particular VGA used (AD603ARZ evaluation board, Analog Devices, Norwood, MA, USA) is capable of an amplification range of 40 dB (-10 dB to 30 dB in the configuration used), with a response rate of 80 dB/μs. The time-gain compensation for photoacoustic modes is a constant gain of some small attenuation until about 7.5 μs to minimize unwanted signals (the focus is at 8.45 μs), then a ramp up to maximum gain at 11 μs. For ultrasound, a similar scheme is used, save that the ramp begins at 11 μs (the focus is at 16.9 μs) and achieves full gain at 24.6 μs, followed by a drop of about 6 dB at 31 μs, and a further drop to the original level at 34 μs.

3.2.3 Data acquisition

Data is currently acquired using an oscilloscope (DPO 7054, Tektronix, Beaverton, OR, USA), using a sampling rate of 500 MHz. Signal inputs are terminated at 50 Ω for impedance matching to the VGA. Acquisition triggers are provided by the sync-out outputs of the ultrasound pulser-receiver and the laser. Future improvements to the system will have data acquisition via a PCI

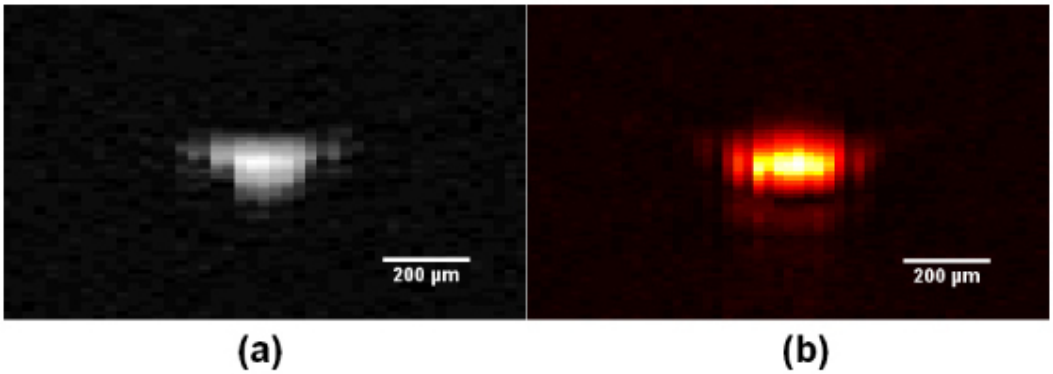

Figure 3.3: Images of a carbon fiber at the focal position: (a) US (Log Scale); (b) PA.

card, allowing the entire system to be controlled by a single computer. For interlaced images, the horizontal delay of the oscilloscope is set to 6 μs and the length of the acquisition window is set to 20 μs. This allows us to capture total of 8.5 mm depth of a sample in both modes.

3.2.4 US-PA data mapping

Interlaced images are separated and plotted as standard B-mode ultrasound and photoacoustic images. To combine images, a simple program was written to co-register the images. The photoacoustic images were thresholded and superimposed on the ultrasound B-scans in an orange colormap.

3.3 Results

3.3.1 Resolution studies

A single 7.5-μm carbon fiber (Sigrafil C25 T060 EPY, SGL Group, Wisbaden, Germany) was imaged at different depths by using our system. The focal lateral resolution of the ultrasound mode was measured at 140 $\pm$ 10 μm, with accompanying axial resolution of $<$40 μm. Lateral resolution of the photoacoustic mode was slightly worse at 180 $\pm$ 10 μm due to one-way, rather than

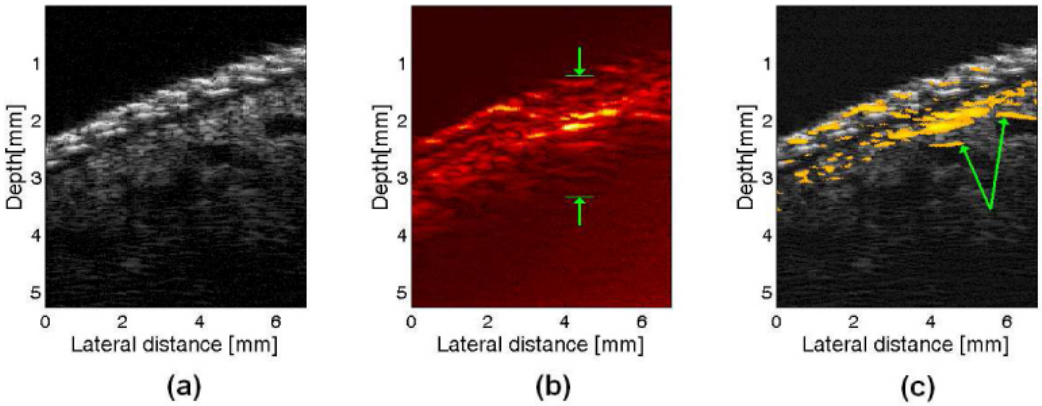

Figure 3.4: US and PA images of human finger (a) US image; (b) PA image, arrows indicate effective photoacoustic imaging depth; (c) Combined image, arrows indicate where large vessels are seen only in part in PA data.

2-way focusing. Both were measured at the focus by taking the maxima along the appropriate direction, normalizing to the absolute maximum, plotting on a decibel scale, and finding the full-width half-maximum at the -6 dB point. Images of the fiber at the focus are shown in Figure 3.3a and 3.3b using US and PA modalities respectively.

3.3.2 In vivo imaging

To capture in vivo images, we imaged the underside tip of the ring finger of an adult subject's right hand, immersed in a water bath.

Figure 3.4 shows the combined ultrasound-photoacoustic mode. The interleaved scans are separated to form individual images of ultrasound data (Figure 3.4a), and photoacoustic data (Figure 3.4b), then combined to form a composite image (Figure 3.4c). Figure 3.5 provides a sample of the intended use of the system. First, an interesting structure may be located using the ultrasound-only mode (Figure 3.5a), then the combined imaging mode may be used to form a more detailed image. In a video, it is possible to see speckle changes, indicating blood flow, suggesting that this system may be suitable for color Doppler applications.

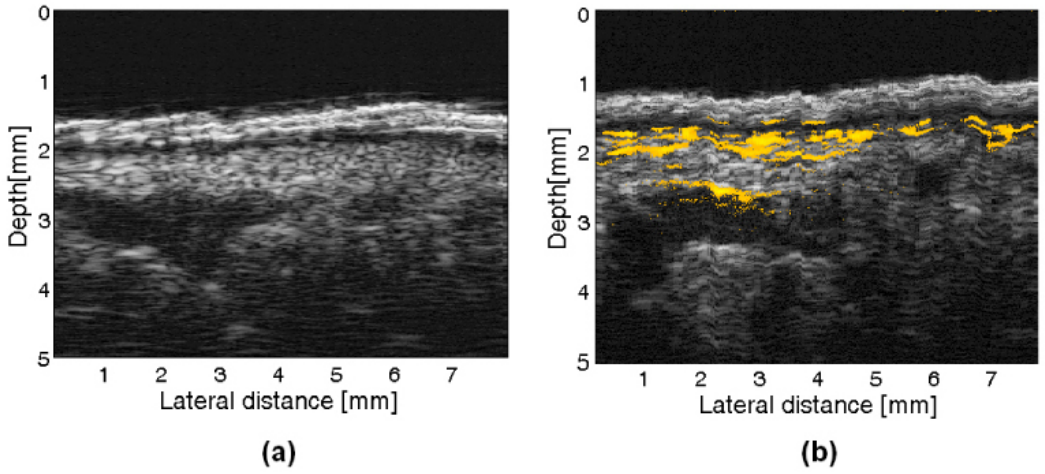

Figure 3.5: Similar structures in movie frame ((a), (Media 1) and a combined image (b).

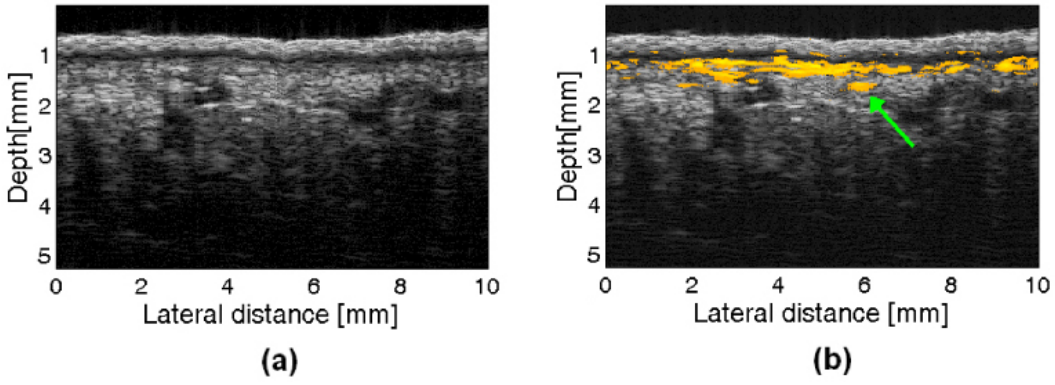

Figure 3.6: Example of seeing vessel with PA (Green Arrow in (b)) that is not visible in US in (a).

Figure 3.6 shows how the two imaging modalities can be used in a complimentary fashion. Figure 3.6a shows the ultrasound-only data, and Figure 3.6b shows the combined image. In Figure 3.6b, the photoacoustic image shows vascular structures not clearly present in the ultrasound-only image, an example of which is annotated by a green arrow.

3.4 Discussion

The synergy of combining ultrasound and photoacoustic biomicroscopy is evident from viewing Figures 3.4 to 3.6. In the data acquired for Figure 3.6 using the fast-scanning ultrasound mode, subcutaneous vessel structures and visible speckle changes within the vessel corresponding to blood flow can be seen. Photoacoustic imaging shows very fine vessel structures not evident from the ultrasound scan. Figure 3.6 shows a fairly prominent vessel that is clear from the photoacoustic scan but not the ultrasound scan. Conversely, ultrasound shows some large vessel structures that are too deep to be seen by photoacoustic imaging. Vessels on the right side of Figure 3.4c are clearly seen in the ultrasound scan – and they have a corresponding photoacoustic signature, however, this signal is only seen at the top of the vessel. The principle reason for this is that the optical penetration depth of green light in whole blood is <50 μm.

From Figure 3.4b, we gauge the photoacoustic penetration depth as roughly 2 mm. Improved penetration depth may be expected at longer optical wavelengths where the reduced scattering coefficient is less, and where penetration through blood is more. The present system uses 532 nm light due to laser availability. Penetration depth is limited by the attenuation of light and ultrasound, and by the depth of field of the single element transducer ($\sim$2 mm).

Future work will incorporate a tunable laser system that operates at a

higher pulse-repetition rate, thus enabling multiwavelength studies and faster imaging rates respectively. These and other future improvements, including realtime display, high-frequency arrays for dynamic focusing, and 3-D scanning should prove highly valuable for a number of pre-clinical and clinical studies concerned with microvascular morphology and function within a number of pathologies.

3.5 Summary and conclusions

To our knowledge this is the first work that combines ultrasound and photoacoustic imaging at high frequencies (>20MHz) and fast imaging rates. By combining fast-scanning high-resolution ultrasound with photoacoustic microscopy we are able to see photoacoustic signatures in context of the surrounding tissue structures. Blood flow can be visualized in the B-scan movie, and overlaid photoacoustic images provide optical contrast information to the ultrasound backscatter information provided by pure ultrasound. Multiwavelength studies may open up doors to measure blood oxygen saturation and flow, which could pave the way to quantitative oxygen consumption measurements [10, 11].

References

[1] Lidai Wang et al. "Fast voice-coil scanning optical-resolution photoacoustic microscopy". In: *Opt. Lett.* 36.2 (Jan. 2011), pp. 139–141. DOI: 10.1364/OL.36.000139.

[2] M Xu and L.V. Wang. "Photoacoustic imaging in biomedicine". In: *Review of Scientific Instruments* 77.4041101 (2006), pp. 1–22.

[3] Konstantin Maslov, Hao F Zhang, and Lihong V Wang. "Effects of wavelength-dependent fluence attenuation on the noninvasive photoacoustic imaging of hemoglobin oxygen saturation in subcutaneous vasculature in vivo". In: *Inverse Problems* 23.6 (2007), S113.

[4] Li Li et al. "Simultaneous imaging of a lacZ-marked tumor and microvasculature morphology in vivo by dual-wavelength photoacoustic microscopy". In: *Journal of Innovative Optical Health Sciences* 01.02 (2008), pp. 207–215. DOI: 10.1142/S1793545808000212.

[5] Edward Zhang, Jan Laufer, and Paul Beard. "Backward-mode multiwavelength photoacoustic scanner using a planar Fabry-Perot polymer film ultrasound sensor for high-resolution three-dimensional imaging of biological tissues". In: *Appl. Opt.* 47.4 (Feb. 2008), pp. 561–577. DOI: 10.1364/AO.47.000561.

[6] J.J. Niederhauser et al. "Combined ultrasound and optoacoustic system for real-time high-contrast vascular imaging in vivo". In: *Medical Imaging, IEEE Transactions on* 24.4 (Apr. 2005), pp. 436–440. ISSN: 0278-0062. DOI: 10.1109/TMI.2004.843199.

[7] Hao F Zhang et al. "Functional photoacoustic microscopy for high-resolution and noninvasive in vivo imaging". In: *Nat. Biotechnol.* 24.7 (July 2006), pp. 848–51. ISSN: 1087-0156. DOI: 10.1038/nbt1220.

[8] Roger J. Zemp et al. "Realtime photoacoustic microscopy in vivo with a 30-MHz ultrasound array transducer". In: *Opt. Express* 16.11 (May 2008), pp. 7915–7928. DOI: 10.1364/OE.16.007915.

[9] F.S. Foster et al. "A new ultrasound instrument for in vivo microimaging of mice". In: *Ultrasound in Medicine and Biology* 28.9 (2002), pp. 1165–1172. ISSN: 0301-5629. DOI: 10.1016/S0301-5629(02)00567-7.

[10] L.V. Wang. “Prospects of photoacoustic tomography”. In: *Medical Physics* 35 (12 2008), pp. 5758–5767.

[11] Song Hu et al. “Functional transcranial brain imaging by optical-resolution photoacoustic microscopy”. In: *Journal of Biomedical Optics* 14.4 (2009), pages. DOI: 10.1117/1.3194136.

Chapter 4

Realtime clinically-oriented array-based in vivo combined photoacoustic and power Doppler imaging

4.1 Introduction

Photoacoustic (PA) imaging has been steadily moving towards clinical imaging applications. *In vivo* experiments using both optical-resolution photoacoustic microscopy (OR-PAM) and tomographic systems have shown special promise. For instance, Wang et al. demonstrated an OR-PAM system capable of video-rate visualization of individual blood cells [1], and the tomographic work of Ntziachristos and Razansky has shown very good agreement with histology [2]. Endoscopic OR-PAM being developed by our group promises to allow for

A version of this chapter has been published. Harrison et al. 2014. Proc SPIE. 8943.

assessment of potentially cancerous lesions [3].

Regular photoacoustic imaging has seen much less development and use. In particular, ultrasound array-based systems have seen little exploration. We have shown that array-based ultrasound systems can be converted to photoacoustic systems with minimal modification [4], but the most powerful systems allow for simultaneous ultrasound and photoacoustic capture. These systems remain out of reach for many researchers due to cost and a lack of demonstrated value. Certainly, there have been some pre-clinical studies using such systems exploring applications such as gene expression [5], needle guidance [6], and even brachytherapy implantation [7], but little showing array photoacoustic imaging in humans. Some groups have shown some imaging in peripheral joints [8] and breast tissue [9], but in order to increase the adoption of these systems, more *in vivo* human imaging needs to be demonstrated.

In this work, we focus on the use of a flexible ultrasound acquisition system to provide real-time overlaid multi-angle flash ultrasound, photoacoustic, and power Doppler imaging. The inclusion of power Doppler provides a method of validation as flowing blood will be visualized in photoacoustic images as well. However, photoacoustic imaging is much better at showing small and slow flowing vessels while power Doppler more clearly shows large and fast vessels, making these two modes somewhat complementary. The reasons for these different strengths stem from the differences in contrast mechanisms. Photoacoustic signal arises purely from absorption, so any absorber of sufficient strength will be visualized, no matter the size. Doppler imaging relies on the movement of speckle patterns, and the faster the flow and Doppler repetition rate, the fewer motion artifacts will be present. One important point is that vessels look very different between the two modes. Since power Doppler imaging relies on tracking the speckle pattern within vessels, the entire flow area is imaged. Photoacoustic images, however, show only the top and bottom

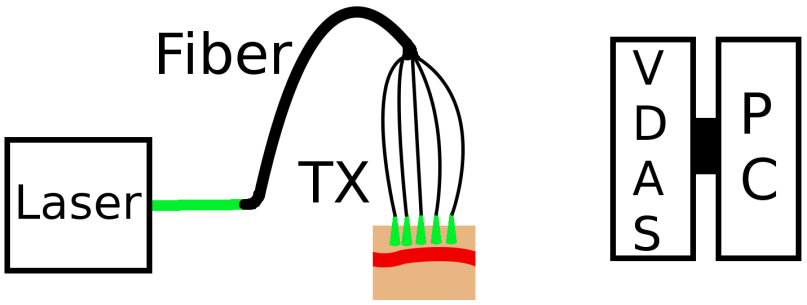

Figure 4.1: Basic system setup. Laser light is coupled into a multi-legged fiber-based light guide which is mechanically coupled to an array transducer (TX). The transducer is connected to a Verasonics data acquisition system (VDAS), controlled by a host PC.

of vessels due to the filtering characteristics of the ultrasound transducer. In most *in vivo* images, often only the top is visible due to optical attenuation through blood. By combining power Doppler, photoacousstic, and ultrasound imaging, we present a more complete vascular image with structural context.

4.2 System design

4.2.1 Image acquisition

The system setup is shown in figure 4.1. While we have an optical parametric oscillator and dye laser available, we have elected to use either the fundamental or frequency-doubled Nd:YAG output from our Continuum Surelite III laser for this work. This is simply due to a lack of power from those modes: the output end of the fiber results in about an 8 cm^2 roughly rectangular spot, so to achieve near-ANSI limited imaging, we require roughly 160 mJ/pulse for 532 nm or 800 mJ/pulse for 1064 nm at the output of the ten-legged light guide (custom fabricated by Ceramoptec Inc.). While the theoretical transmission through the light guide is in excess of 80% for both of those

wavelengths, damage to the input end has limited that to roughly 40-50%. For the experiments here, we used an output fluence of $\sim$ 5 mJ/cm^2 at 532 nm, and $\sim$ 40 mJ/cm^2 at 1064 nm.

The ultrasound transducer used is an HDI-5000 compatible L7-4 (5 MHz center frequency, 60% bandwidth from Broadsound Corporation). Lateral resolution has been characterized at $\sim$ 500 μm for flash ultrasound, and $\sim$ 600 μm for photoacoustic imaging.

Ultrasound acquisition is handled by the VDAS (Verasonics Inc.), which is controlled by the host PC. The VDAS is programmed with a user-specifiable event sequence which allows for interleaved capture of multiple imaging modes, coupled with real-time streaming to the host PC via PCI-Express. Image formation proceeds in real-time on the host computer.

The image acquisition sequence used here first captures a multiple-angle flash ultrasound image, then a full-frame PA image, then a power Doppler image. For multiple-angle flash imaging, we use 7 angles evenly distributed between -18°, and 18° (which are subsequently summed to form a higher-resolution image). The Doppler ensemble is comprised of 14 images at a transmit angle of 12°, and a PRF ranging from 50-3000 Hz depending on the flow rate. To eliminate the delay stemming from triggering the VDAS which results in missing photoacoustic data, we use a pulse-delay generator to operate the laser and trigger the photoacoustic data capture. Imaging rate is limited to 10 frames per second by the maximum laser repetition rate.

As data are being streamed to the host PC (over a direct PCI-E link to the VDAS), they are reconstructed. The multiple-angle flash and Doppler images are reconstructed using the Verasonics-provided software, while the photoacoustic images are delay-and-sum beamformed using a threaded MATLAB module written for that purpose. All three images are then passed to custom display code which overlays the images using a threshold defined by a

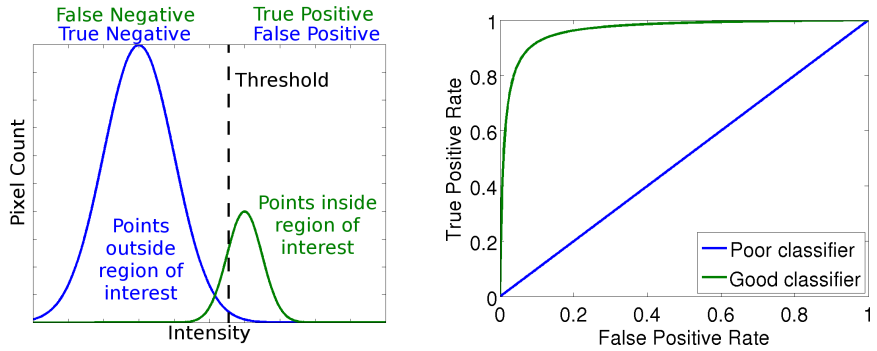

(a) (b)

Figure 4.2: Receiver operating characteristic (ROC) curve generation. The threshold in (a) is moved to generate a curve of false vs. true positive rates in (b).

rejection parameter, scales their colormaps according a compression parameter, and persists between frames based on a persistence parameter. The three parameters (reject, compress, and persist) are set independently for each imaging mode in the GUI. The display for each mode may also be toggled on and off. The availability of these options allows an operator to select an area of interest with Doppler turned off to avoid huge motion artifacts, then tweak each imaging mode to provide the best image possible.

4.2.2 Characterization

To compare the effectiveness of power Doppler and photoacoustic imaging, we use flowing blood as our target. We then identify a region of interest (ROI) where there is flowing blood. We then construct a receiver operating characteristic (ROC) curve, as is illustrated in figure 4.2. In brief: construct a distribution of pixels inside and outside the ROI, set a threshold, count true and false positives, then move the threshold and repeat. This will give a map of false versus true positive rates. A poor classifier will have identical distributions, and thus generate a line with slope of unity. A perfect classifier will have no overlap between the distributions, and be a line of slope zero and

y-intersect 1. ROC curves can be condensed into their integral, or area under the curve (AUC), where 0.5 is a poor classifier, 1 is a perfect classifier, and less than 0.5 means that the classifier seems to exhibit negative contrast (which is nonsensical for the imaging modes being tested here).

4.3 Experiments

4.3.1 Flow Phantoms

Performing ROC analysis *in vivo* is quite impractical. Motion artifacts will be abundant, especially if looking at high-flow regions such as the carotid. Tissue motion may also cause a slight change in imaging plane. There is also the difficulty of identifying an ROI properly. Blood is widely spread through tissues, and what may look like noise or spurious signal in a PA image may indeed be blood. For these reasons, we constructed a tissue-mimicking phantom comprised of 10% by weight of each 300-bloom gelatin and corn starch dissolved in water to provide similar mechanical properties and speckle patterns to real tissue. We embedded a length of both 3.0 mm and 0.86 mm inner diameter tubings at a depth of about 1 cm while this was setting. We used a syringe pump to provide flow for both a blood-mimicking fluid (5% corn starch in water mixed with ink to provide similar optical absorption at the target wavelength) and rabbit blood. We varied the flow from 1-40 mm/s, which was the fastest our syringe pump could manage for the 3.0 mm tubing. For each flow rate, the Doppler pulse-repetition-frequency (PRF) was modified such that the flow would be close to saturating the image using the blood-mimicking fluid.

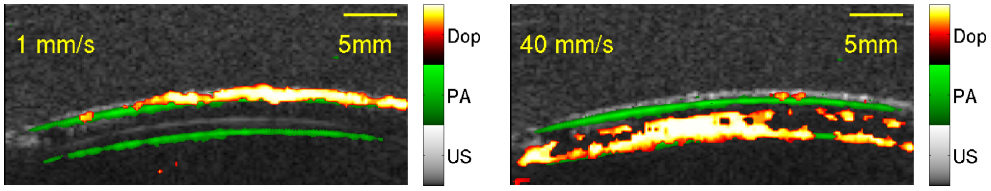

(a) (b)

Figure 4.3: Multimodal images at 532 nm for (a) 1 mm/s and (b) 40 mm/s with blood-mimicking fluid.

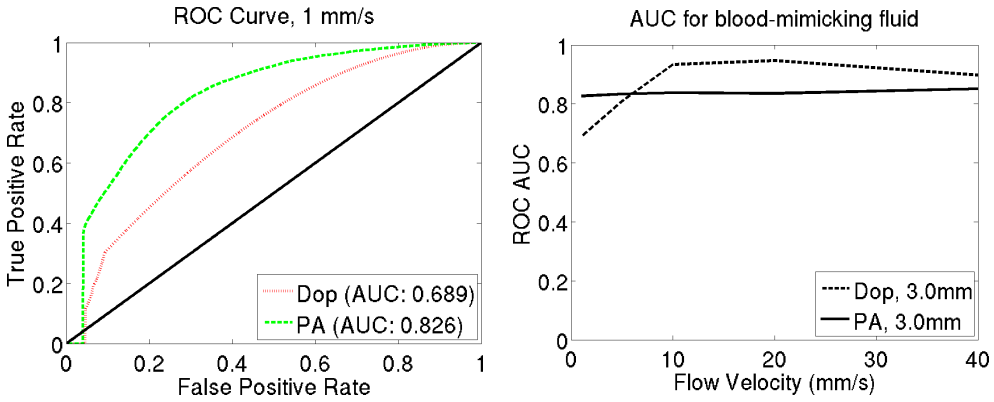

(a) (b)

Figure 4.4: (a) Sample ROC curves for 1 mm/s for blood-mimicking fluid, and (b) accompanying velocity vs. AUC (Dop = power Doppler, PA = photoacoustic).

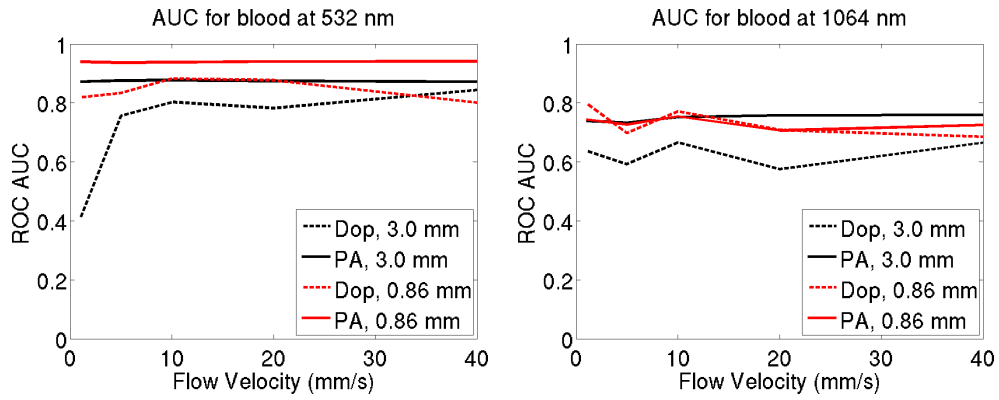

(a) (b)

Figure 4.5: Velocity vs. AUC for blood at (a) 532 and (b) 1064 nm.

Blood mimicking fluid

Figure 4.3 shows typical images captured at 1 and 40 mm/s flow at a wavelength of 532 nm. It is apparent that the Doppler image at low flow velocity is actually only picking up on the top of the tubing. This problem was much more pronounced in the smaller tubing. While it may appear that some of the PA signal may be due to the tubing itself, experiments with water show very little absorption at 532 nm, and none at 1064 nm. Figure 4.4 show a typical ROC curve (at 1 mm/s) and the measured AUC for both imaging modes.

Blood

The same experiment was repeated using rabbit blood in place of the blood-mimicking fluid. However, due to concerns over the penetration of 532 nm light *in vivo*, 1064 nm light was also used. The resulting AUC measurements for both wavelengths are shown in figure 4.5.

4.3.2 In Vivo

Finally, we imaged various targets in the human body. We focused on large vessels and synovial joints. The carotid is an excellent target due to the high

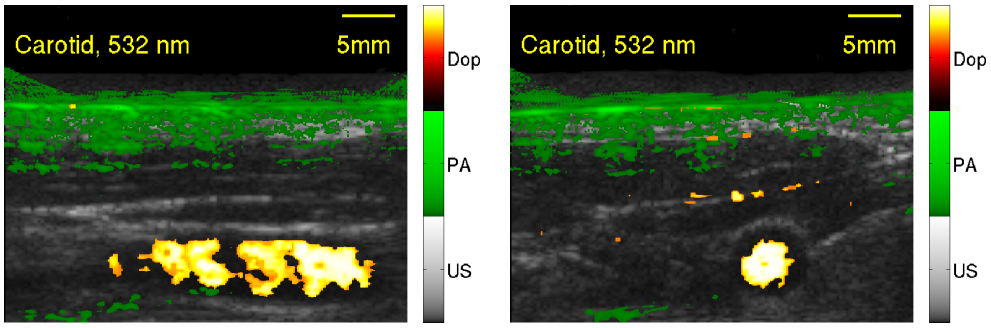

(a) (b)

Figure 4.6: (a) Longitudinal and (b) transverse carotid images at 532nm.

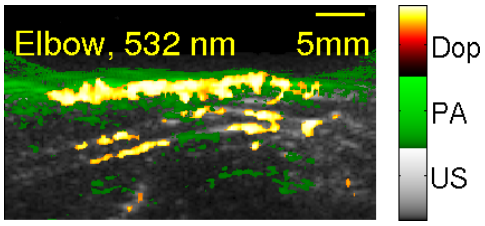

Figure 4.7: Elbow image at 532nm.

flow velocity, large blood volume, and ease of identification on the ultrasound image. Synovial joints were chosen due to the blood-rich areas and proximity to arteries through the limbs. For all the images presented here, a gelatin standoff approximately $\sim$ 1.5 cm thick was used to allow illumination under the transducer face.

Illumination at 532 nm

Figures 4.6 and 4.7 show images of the carotid and interior of the elbow of a healthy volunteer. The slow repetition rate of the laser made obtaining good Doppler images quite challenging, due not only to motion between frames, but also the inconsistent flow velocity. In fact, figure 4.7 is likely only showing areas of high ultrasound intensity rather than actual flow, though the coincident photoacoustic signal suggests the presence of blood. Figure 4.6 is much clearer. Though the penetration of the 532 nm light at the fluence we were able to use was not sufficient to reach the carotid, some surface vessels appear to be visible.

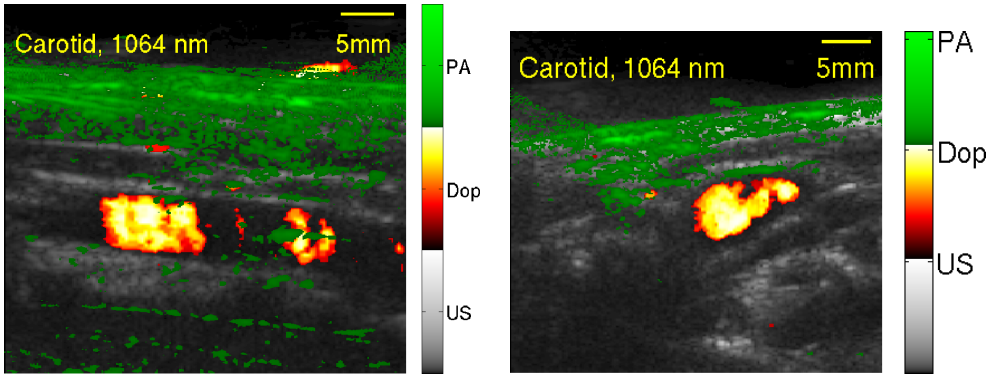

(a) (b)

Figure 4.8: (a) Longitudinal and (b) transverse carotid images at 1064nm.

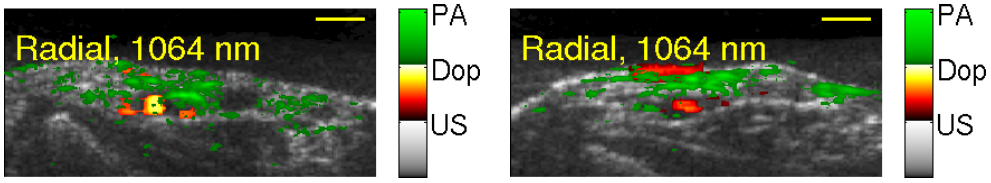

(a) (b)

Figure 4.9: In vivo imaging of radial artery at 1064nm.

Illumination at 1064 nm

Imaging at 1064 nm provides better images due to both the increased fluence used, and the lower optical absorption of both blood and melanin, leading to less shadowing of deeper vessels. Figure 4.8 shows transverse and lateral views of the carotid artery, where some photoacoustic signal may be seen. Figure 4.9 shows an image of the wrist, with the radial artery visible in both PA and Doppler imaging.

4.4 Discussion

Phantom studies are quite encouraging. The results shown in figure 4.4 are as expected: PA imaging performs virtually identically across all flow velocities, whereas Doppler has a noticeable performance drop below about 10 mm/s, even when the PRF is adjusted to account for slower flow. PA imaging remains

an excellent way to identify blood-mimicking fluid in the 3.0 mm tubing across all flow velocities. The tests with real blood at 532 nm from figure 4.5(a) are somewhat more encouraging, as the AUC for PA imaging is very high, and remains higher than the Doppler AUC for all flow velocities in both sets of tubing. In figure 4.5(b) the results are somewhat more confusing in that the performance in the small tubing shows almost the opposite behavior. As it turns out, the Doppler images in these experiments picked up far more of the tubing than is desirable. Nonetheless, PA imaging seems to do no worse in this set of experiments.

In vivo images in Figures 4.6 show that 532 nm is not well suited for imaging in highly vascular areas with deep tissue like the neck. Only some peripheral vessels can be seen, and the carotid is only visible in the Doppler image. However, for more peripheral structures, such as the interior of the elbow shown in figure 4.7, Doppler and PA imaging seem to show some similar structures, and so this wavelength may still be useful for some imaging targets. Imaging at 1064 nm does give the imaging depth required to reach the human carotid, seen in figure 4.8, and even more peripheral structures such as the radial artery can be imaged successfully. The radial artery structures actually proved to be difficult to image due to their size, but PA and US images were used to guide the transducer placement to maximize Doppler signal. Ultrasound image quality in this particular study is relatively low from a radiological perspective. This is largely due to the use of flash (pane-wave) imaging. For future studies, techniques such as synthetic aperture imaging will provide much better image quality. Higher frequency transducers will also improve image quality, and will certainly be very important for proper clinical studies. This preliminary study only motivates future clinical work by demonstrating the practicality of a clinical tri-mode system.

4.5 Conclusions

We have combined photoacoustic and Doppler imaging with more traditional ultrasound image to provide overlaid images of all three imaging modes. The strengths of photoacoustic imaging stem from the independence of flow velocity, and resilience to motion artifacts, whereas Doppler imaging shows the entire volume of flow. In this way, the two methods can be considered somewhat complementary, and indeed we find that even in a controlled phantom situation, power Doppler begins to perform more poorly below about 10 mm/s. *In vivo* imaging of these flow velocities would be quite difficult for power Doppler due to natural tissue motion creating large image artifacts, but photoacoustic imaging performs quite well, independently of flow velocity. While the filtering effects causing vessels to be outlined in photoacoustic imaging will impact performance on large vessels, it made little difference relative to power Doppler in terms of phantom performance. Both blood-imaging modes can be used to guide each other to form a better overall image, with the traditional ultrasound providing structural context. Future studies will focus on improving image quality for all three modes, with the potential of moving to a higher ultrasound frequency system.

References

[1] Lidai Wang et al. "Fast voice-coil scanning optical-resolution photoacoustic microscopy". In: *Opt. Lett.* 36.2 (Jan. 2011), pp. 139–141. DOI: 10.1364/OL.36.000139.

[2] Vasilis Ntziachristos and Daniel Razansky. "Molecular imaging by means of multispectral optoacoustic tomography (MSOT)". In: *Chemical reviews* 110.5 (2010), pp. 2783–2794.

[3] Parsin Hajireza et al. “Optical resolution photoacoustic microendoscopy with ultrasound-guided insertion and array system detection”. In: *Journal of Biomedical Optics* 18.9 (2013), pp. 090502–090502. DOI: 10.1117/1.JBO.18.9.090502.

[4] Tyler Harrison and Roger J Zemp. “The applicability of ultrasound dynamic receive beamformers to photoacoustic imaging.” In: *IEEE transactions on ultrasonics, ferroelectrics, and frequency control* 58.10 (Oct. 2011), pp. 2259–63. ISSN: 1525-8955. DOI: 10.1109/TUFFC.2011.2076.

[5] Tyler Harrison, Robert J. Paproski, and Roger J. Zemp. “In vivo imaging of inducible tyrosinase gene expression with an ultrasound array-based photoacoustic system”. In: vol. 8223. 2012, pages. DOI: 10.1117/12.908987.

[6] Chulhong Kim et al. “Handheld array-based photoacoustic probe for guiding needle biopsy of sentinel lymph nodes”. In: *Journal of Biomedical Optics* 15.4 (2010), pages. DOI: 10.1117/1.3469829.

[7] Tyler Harrison and Roger J Zemp. “Coregistered photoacoustic-ultrasound imaging applied to brachytherapy.” In: *Journal of biomedical optics* 16.8 (Aug. 2011), p. 080502. ISSN: 1560-2281. DOI: 10.1117/1.3606566.

[8] Guan Xu et al. “Photoacoustic and ultrasound dual-modality imaging of human peripheral joints”. In: *Journal of Biomedical Optics* 18.1 (2012), pp. 010502–010502. DOI: 10.1117/1.JBO.18.1.010502.

[9] Zhixing Xie et al. “Combined photoacoustic and ultrasound imaging of human breast in vivo in the mammographic geometry”. In: vol. 8581. 2013, pages. DOI: 10.1117/12.2004599.

Chapter 5

Optical-resolution photoacoustic micro-endoscopy with ultrasound array system detection

5.1 Introduction

Endoscopic imaging is an important tool for physicians that allows them to visually inspect the interior structures of the circulatory, respiratory, and digestive systems. However, traditional optical imaging techniques are limited in the types of information that they can provide. Simple camera systems can help identify areas of interest, but cannot often definitively identify the structure. For instance, in an investigation of atherosclerosis, it is beneficial to determine the makeup of a plaque: those with high lipid content are the

A version of this chapter has been published. Harrison et al. 2013. Proc SPIE. 8581: 85810C.

most dangerous and thus the most important to treat. Such an identification is possible with photoacoustic imaging using around 1200nm light [1]. Photoacoustic imaging also allows for assessment of blood oxygenation status, which would provide an invaluable tool for identifying the hypoxic, hyperoxic, and even angiogenic regions that are present in some cancers [2]. Optical-resolution photoacoustic microscopy (OR-PAM) offers visualization of structures down to the capillary level at up to 1mm deep in tissue which is better than many optical imaging techniques.

The motivation for photoacoustic endoscopy systems is clear. However, to make the technique practical, several concerns need to be addressed. In a photoacoustic system, there are two primary concerns: light delivery and ultrasound collection. We have used image guide fibers to accomplish light delivery - both with and without a lens for refocusing into tissue - with excellent results. This gives the endoscope a very small footprint, potentially allowing use in much smaller structures than previous endoscopy systems. That just leaves ultrasound detection. Most OR-PAM systems have used a single piezoelectric element, and focused on maximizing the ultrasound signal through careful alignment of the optical and ultrasound components [3, 4]. This is a tedious procedure that tightly couples the light delivery and ultrasound detection together in space, increasing the bulk of the probe to an extent that it is no longer useful for endoscopy, though hand-held applications are still viable [3]. Optical detection techniques based on Fabry-Perot interferometry would offer clear advantages in terms of footprint and sensitivity, but these require specialized coating of the end of the fiber and additional optical setup. These coatings intrinsically limit the wavelengths that can be used for photoacoustic imaging, and offer no advantage in terms of external guidance.

Ultrasound array transducers offer several advantages to other OR-PAM ultrasound detection techniques. First, the same transducer can be used for

endoscope guidance and data collection, eliminating the need for another system to guide the endoscope. Alignment between the optical and ultrasound components becomes much easier as the end of the fiber need only be near the elevational focus. In the imaging plane of the transducer, photoacoustic signals can be boosted by delay-and-sum beamforming. The potential difficulties with using an ultrasound transducer in this manner are three-fold: the sensitivity may be worse than is possible with a single-element, the signal-to-noise ratio (SNR) may be too low to make this technique practical, and alignment of the ultrasound transducer may prove difficult. In this work, we explore the possibility of using an ultrasound array transducer to collect photoacoustic data for OR-PAM endoscopy (OR-PAME). Using dynamic refocusing, we have created images of carbon fibers with a resolution of less than 6 μm and SNR of at least 40dB. Based on previous experience with this array system, we believe this SNR to be enough to detect an image at a minimum of 5 cm in tissue [5], proving that this detection scheme is appropriate for OR-PAME systems. Additionally, we have demonstrated guidance of the fiber through a tissue-mimicking phantom and successfully captured images from a hand-guided endoscope through 2cm of tissue.

5.2 System design

5.2.1 Basic setup

The basic setup is shown in Figure 5.1. A diode-pumped Ytterbium fiber laser (YPL-G, IPG Photonics Corporation) at 532nm ($\sim$1 ns pulse width, 20 μJ per pulse, up to 600kHz) running at 20 kHz is coupled via single-mode fiber, and refocused towards a pair of scanning mirrors (6203H, Cambridge Technology Inc.) controlled by a two-channel function generator (AFG3022B, Tektronix Inc.) outputting sinusoidal outputs at 5Hz and 0.05Hz at an appropriate

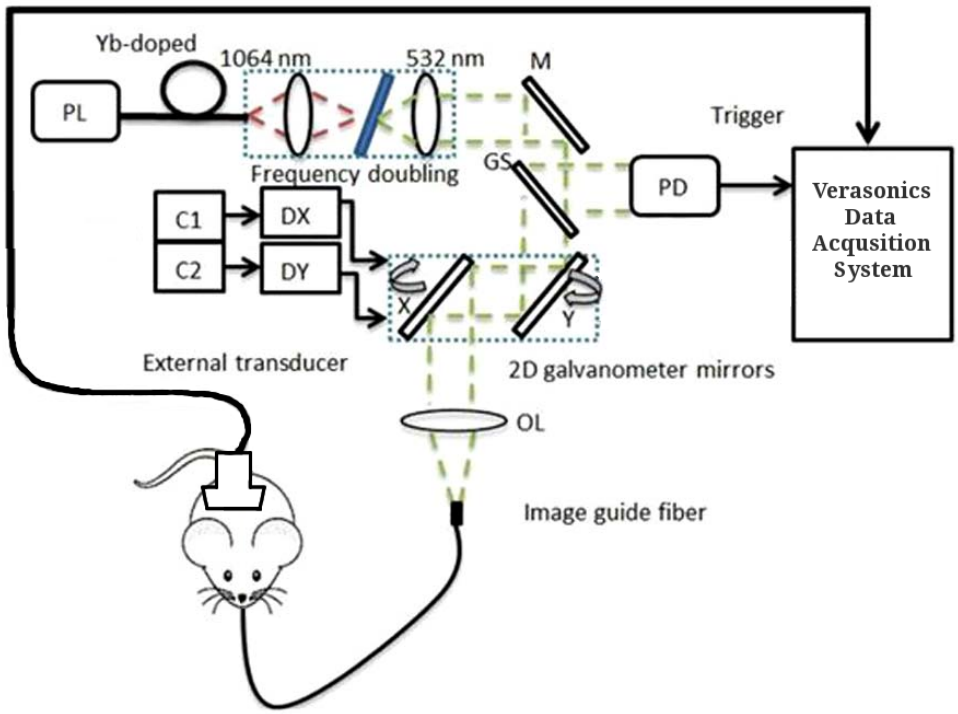

Figure 5.1: System setup. PL:pump laser, M: mirror, GS: glass slide, PD: photodiode, DX: X-axis mirror driver, DY: y-axis mirror driver, OL: objective lens.

peak-to-peak voltage for the desired field of view. Before the mirrors, part of the beam is picked off to trigger a photodiode that provides a trigger to the ultrasound acquisition system. The light from the mirrors is focused again by an objective lens (f = 18 mm) into the input end of the image guide fiber, consisting of 30000 individual fibers in a 0.8 mm bundle.

Ultrasound signals are collected by an L7-4 transducer connected to a Verasonics VDAS ultrasound acquisition system. This captures data across all 128 elements simultaneously at 1000 frames per second. Due to memory limitations in the system, we are only capable of capturing data at 10000 points, as each point consists of the 128 channels by about 1500 samples in depth.

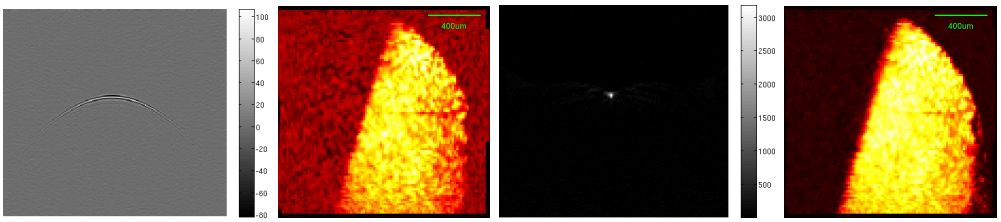

(a) (b) (c) (d)

Figure 5.2: The effects of using beamformed data to reconstruct images of black tape. (a) Received data traces for one image; (b) Maximum amplitude projection of received data (SNR=29 dB); (c) Beamformed data for one image; (d) Maximum amplitude projection of beamformed data (SNR = 50 dB).

5.2.2 Image reconstruction

Image reconstruction is accomplished by forming a maximum amplitude projection of the received data. All images shown in this paper are presented on a logarithmic color scale. While it is possible to form images from the raw data, there are significant advantages in terms of SNR using beamforming. While this can theoretically be done very quickly by only reconstructing an area around the fiber tip, we currently form the entire photoacoustic image using delay-and-sum beamforming, then take the maximum amplitude. Since we are using sinusoidal scanning, the images are re-interpolated on a square grid. The feedback signals are simulated based on the function generator parameters to simplify the data collection. Finally, a Gaussian filter is applied to provide some smoothing. Figure 5.2 shows images formed from both raw and beamformed data, along with representative images that show the raw and beamformed sources. The signal-to-noise ratio (SNR measured as 20 time the 10-base log of the ratio of the average signal to the standard deviation of the noise) improvement is quite dramatic, increasing by 11dB in this case.

5.3 Experiments

5.3.1 Design

Two sets of imaging experiments were performed: one in through mode with a setup similar to traditional OR-PAM systems, and another demonstrating real endoscopy with a phantom. The goals of these experiments were to: establish the feasibility of OR-PAM with array transducer detection; determine if SNR would be sufficient for *in vivo* OR-PAME; demonstrate endoscope guidance; and to show realistic endoscopy in a phantom.

5.3.2 Through-mode study

As mentioned previously, this setup is very similar to traditional OR-PAM systems. Similarly to figure 5.1, the main difference is in the particular setup of the imaging target, image guide fiber, and array transducer. We used an acrylic ring with a cling-wrap membrane to couple the array transducer to the target: black tape or carbon fibers placed at the bottom in contact with the membrane. The image guide was pointing upwards towards the transducer face. The challenges in this setup related to alignment, which was achieved by maximizing photoacoustic signal using a photoacoustic imaging mode. The black tape images were used to tweak reconstruction by slight changes to the simulated feedback waveforms, and these modifications were vetted by reconstructing more images of tape and carbon fibers to assess any issues. After this initial tweaking, no changes to the simulated feedback signals were made, and the images remained high quality. A representative image of black tape may be seen in the earlier Figure 5.2, and carbon fiber images are shown in Figure 5.3. All images exhibited excellent SNR, greater than 45dB. Contrast-to-noise ratio (CNR, defined as 20 times the 10-base log of the ratio of the difference of means of single and noise to the square root of the sum of signal

and noise variances) was also investigated. CNR measurements were highly dependent on the signal area chosen, as the signal variance appeared to be quite large. This could be due to hitting the edge between several fibers, damage to the fiber end, or simply dust on the fiber end. Regardless, we measured CNR values around 20 dB in several images.

5.3.3 Phantom study

This study was intended to show the practicality of OR-PAME with an external array transducer. A phantom was formed by creating a gelatin cylinder with 10% by weight of both gelatin and corn starch. This is a tissue-mimicking phantom commonly used in ultrasound studies that provides similar acoustic properties to human tissue. The phantom was formed in a mold (a disposable coffee cup) using two lifts, embedding carbon fibers at the end of a tunnel formed by the suspension of an 8 mm diameter cylinder (a pen). One hardened, the tunnel was filled with water, and imaged with ultrasound. In this study, the ultrasound transducer was fixed in place, and the endoscope was guided by hand. Figure 5.4 shows the ultrasound setup, as well as images of the tunnel as the fiber is being inserted. The end of the fiber actually fills the tunnel due to a connector attached to the end, but it could be removed to achieve an endoscope diameter of under 2 mm. After the fiber was guided to the embedded carbon fibers, several images were taken with different fields of view, shown in Figure 5.5. Again, SNR is excellent at around 40 dB, in spite of the 2 cm of ultrasound attenuation through the tissue phantom.

5.4 Discussion

While raw photoacoustic traces can be used to reconstruct OR-PAME images from array transducer data, Figure 5.2 clearly illustrates that beamforming is

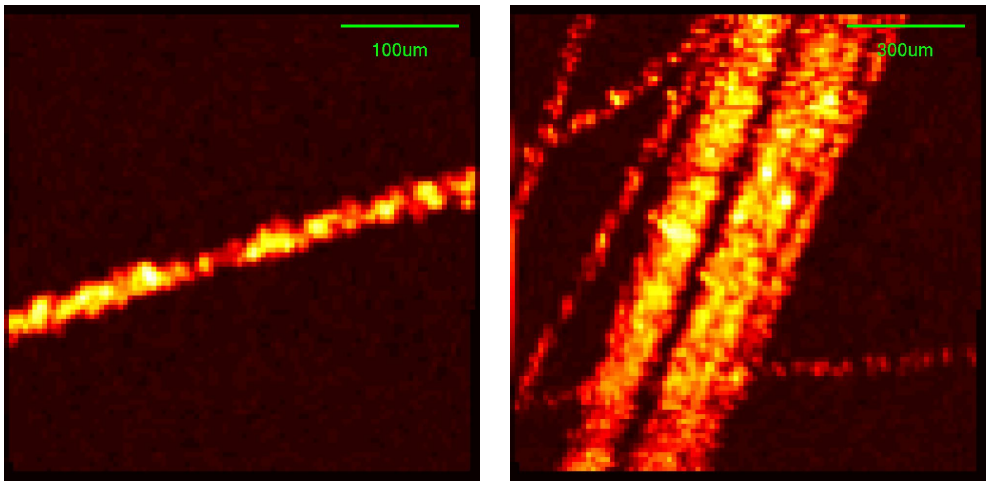

(a) (b)

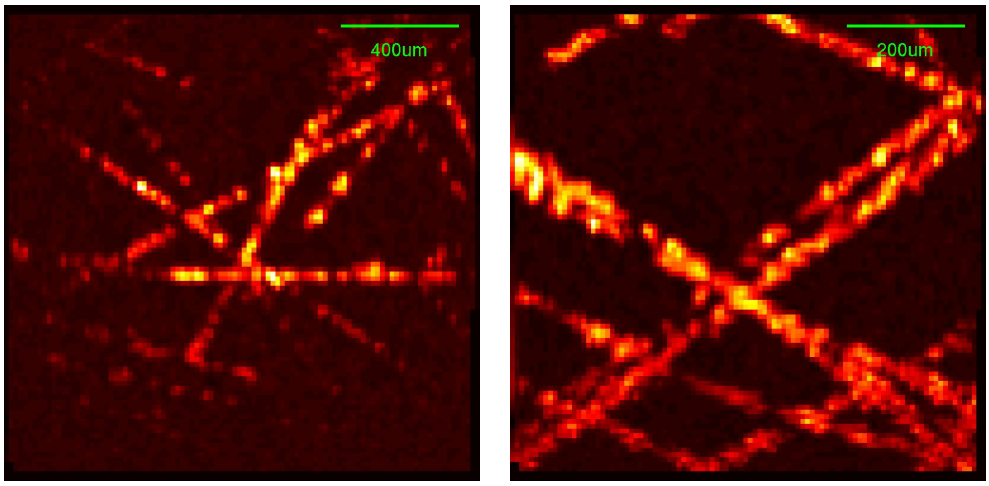

(c) (d)

Figure 5.3: Carbon fiber images captured in through-mode. (a) Single fiber; (b) Fiber bundle; (c) Fiber network with full field of view; (d) Fiber network limited field of view. SNR in these images is >45dB, CNR ∼20dB, full-width half-maximum was measured at 11 μm.

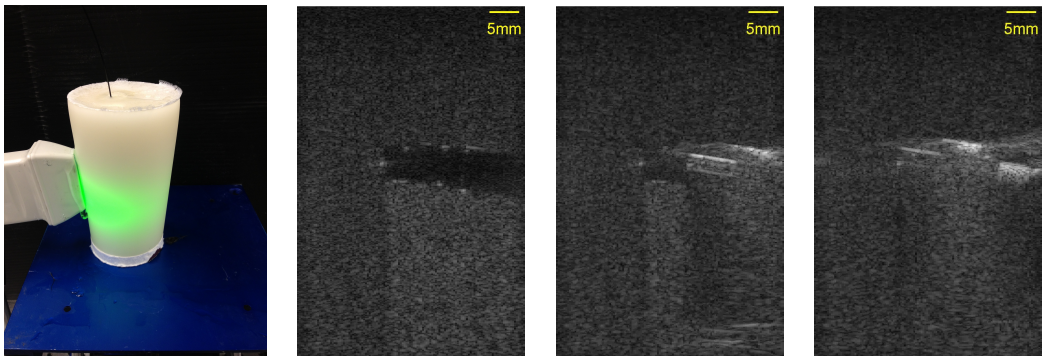

(a) (b) (c) (d)

Figure 5.4: (a) Phantom setup with ultrasound images of (b) before, (c) during, and (d) after insertion of endoscope.

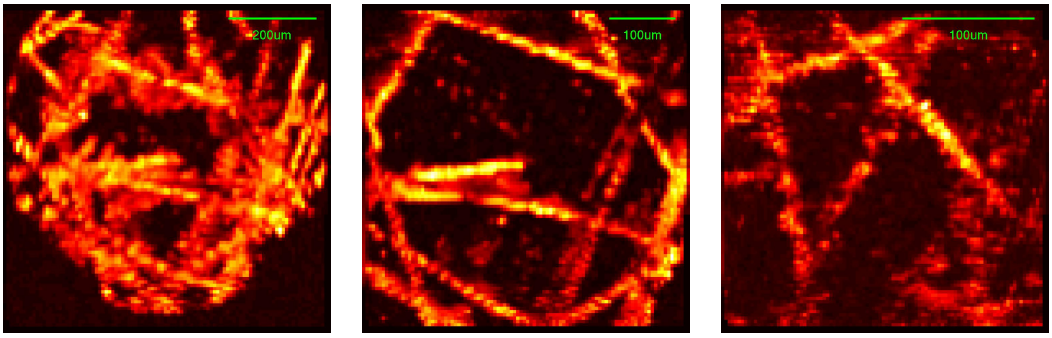

(a) (b) (c)

Figure 5.5: Carbon fiber images captured from tissue-mimicking phantom with three different fields of view. SNR in these images is ∼40dB, CNR ∼13dB, full-width half-maximum was measured at 10 μm.

required to achieve good image quality. Currently, our reconstruction performs full reconstruction of the all 10000 photoacoustic events which takes around 3 minutes, but the beamforming could easily be limited to an area near the fiber tip in order to speed reconstruction to real-time.

With the enhanced SNR offered by beamforming, we were able to capture the images in Figure 5.3 in through-mode, demonstrating that image quality with this system is very similar to other OR-PAM systems. Based on convolution measurements, the 11 μm full-width half-maximum corresponds to a resolution of roughly 9.4 μm, though we expect that better focusing could reduce that to around 7 μm which we have achieved with a similar setup [6].

The practicality of array OR-PAME is shown in Figures 5.4 and 5.5. While for this study, the ultrasound transducer was fixed in place, the endoscope itself was held by hand in contact with the carbon fibers, causing some motion of the phantom during image capture. This realistic endoscopy experiment was quite successful: the fiber is clearly visible for guidance in Figure 5.4 and the images in Figure 5.5 have very good image quality, the resolution for a 10 μm full-width half-maximum is roughly 8.4 μm. While the CNR seems low at 13 dB, CNR is highly dependent on the variance of the selected signal area. Based on similar reasoning from our previous work [5], we believe that with the SNR we have, detection at a tissue depth of 5 cm should be easily achievable. If necessary, CNR could be improved by averaging the raw photoacoustic data of multiple images.

5.5 Conclusions

We have successfully demonstrated external guidance and data capture of OR-PAME. Initial concerns over SNR and transducer alignment proved to be unfounded. Our initial through-mode experiments showed that capture of OR-

PAM data with an array transducer was possible with CNR of around 20 dB by using beamforming to collect received photoacoustic signals. Even through 2 cm of tissue mimicking phantom, images were successfully reconstructed with CNR of 13 dB. While 2 cm will be sufficient for small animal use, we believe that it should be possible to push the endoscope depth to at least 5 cm, though that may require averaging multiple images to achieve acceptable CNR. Photoacoustic endoscopy has great potential for cancer and other disease investigation, and array detection is a simple way to minimize the footprint of the endoscope allowing for greater system flexibility.

References

[1] Bo Wang et al. "Detection of lipid in atherosclerotic vessels using ultrasound-guided spectroscopic intravascular photoacoustic imaging". In: *Optics Express* 18.5 (Feb. 2010), p. 4889. ISSN: 1094-4087. DOI: 10.1364/OE.18.004889.

[2] R.I. Siphanto et al. "Serial noninvasive photoacoustic imaging of neovascularization in tumor angiogenesis". In: *Opt. Express* 13.1 (Jan. 2005), pp. 89–95. DOI: 10.1364/OPEX.13.000089.

[3] P. Hajireza, W. Shi, and R. J. Zemp. "Label-free in vivo fiber-based optical-resolution photoacoustic microscopy". In: *Opt. Lett.* 36.20 (Oct. 2011), pp. 4107–4109. DOI: 10.1364/OL.36.004107.

[4] Hao F Zhang et al. "Functional photoacoustic microscopy for high-resolution and noninvasive in vivo imaging". In: *Nat. Biotechnol.* 24.7 (July 2006), pp. 848–51. ISSN: 1087-0156. DOI: 10.1038/nbt1220.

[5] Tyler Harrison and Roger J Zemp. "Coregistered photoacoustic-ultrasound imaging applied to brachytherapy." In: *Journal of biomedical optics* 16.8 (Aug. 2011), p. 080502. ISSN: 1560-2281. DOI: 10.1117/1.3606566.

[6] Peng Shao et al. “Integrated micro-endoscopy system for simultaneous fluorescence and optical-resolution photoacoustic imaging”. In: *Journal of Biomedical Optics* 17.7 (2012), pages. DOI: 10.1117/1.JBO.17.7.076024.

Chapter 6

The Applicability of Ultrasound Dynamic Receive Beamformers to Photoacoustic Imaging

6.1 Introduction

Photoacoustic (PA) imaging is an emerging technology with many interesting applications stemming from the ability to image optical properties at significant depths with high spatial resolution. In PA imaging mechanical waves are produced in an optically absorbing sample in response to a pulse of light, and may be measured with an ultrasound (US) transducer. Mechanically-scanned single-element systems, while useful, are nonetheless prone to motion artifacts, do not allow for dynamic focusing, and typically require hundreds of laser pulses to form a single image. US array transducers are being explored for PA imaging, potentially allowing one dynamically-focused image to be formed

A version of this chapter has been published. Harrison and Zemp 2011. IEEE Transactions on Ultrasonics, Ferroelectrics, and Frequency Control. 58(10): 2259.

per laser pulse.

One way to accomplish PA imaging with US array transducers is by adapting existing commercial US systems. This approach allows a PA imaging system to be deployed quickly by manufacturers or system owners, but there are a few obstacles that face those that wish to do this. While triggering, data acquisition, disabling US transmission, and laser timing issues are non-trivial, PA image reconstruction is perhaps an even more important concern because of the effect it has on image quality.

US-style reconstruction using delay-and-sum beamforming has been proven appropriate for PA image reconstruction [1], and has been used in various previous works [2, 3, 4, 5, 6, 7, 8]. For instance, Zemp *et al.* [4] and Bitton *et al.* [7] used a custom high-frequency array system and demonstrated real-time beamforming and display based on a PA delay-and-sum beamformer run on commodity computing hardware. While the widely-used Fourier-based reconstruction [9] is more computationally efficient in software, beamforming approaches allow for sector-scanning, aperture growth, and apodization control which have been important in ultrasound imaging. Unfortunately, approaches to using US system beamformers for PA imaging seem to be poorly documented in the literature. Kolkman *et al.* [6], Neiederhauser *et al.* [2] and Park *et al.* [3, 1] all use modified US systems, but do not describe any beamformer modifications. Niederhauser *et al.* later used a system capable of parallel channel data acquisition with Fourier-based reconstruction to form PA images in real-time [10], similar to an approach by Erpelding *et al.* [11]. Parallel channel-data acquisition affords maximum flexibility, but few US systems offer this capability due to the extreme channel-data rates required. Thus, this paper proposes to use existing US array beamformers for PA imaging to decrease the difficulty of setting up PA array systems.

One motivation for attempting to adapt US beamformers for PA imaging

is to avoid extra hardware modification. Unfortunately US dynamic receive beamformers are designed for two-way (pulse-echo) rather than one-way US propagation as is the case in PA imaging. In the best case, it will be possible to get an exact PA beamformer by modifying the data or method of accessing a delay lookup table, but in the worst case the transducer channel data must be captured using additional hardware. Another motivation is to take advantage of the modern beamforming techniques implemented in US systems while avoiding the use of general purpose hardware, as is used in some systems[4, 5]. US beamformers are often implemented in hardware, using parallel beamforming capabilities to provide multiple reconstruction lines from a single excitation. Systems that offer massively parallel beamforming would be of benefit to PA imaging as one dynamically focused image per laser shot is ideally attainable.

This paper shows analytically and experimentally using a linear-array based ultrasound platform with parallel channel acquisition that one need only modify the speed of sound (c) of a US beamformer to properly focus PA images. This could speed adoption of PA imaging because many US systems permit software modification of c. Scaling c by a factor of $\sqrt{2}$ provides good focusing (optimal in the linear-scanned case) though image rescaling is required, a task readily implemented in software.

6.2 Theory

6.2.1 Ultrasound Beamforming

Delay-and-sum beamforming is based on time-of-flight calculations that are used to gather the energy originating from a particular image point. For each point on some predefined imaging plane, data are delayed and summed appropriately to focus at that point. For a US system, the distance to a

particular image point from the center of a reconstruction line is described as $R = \frac{ct}{2}$, with c being the speed of sound in the medium and t the pulse-echo time of flight. For array element n, located at a lateral distance x_n from a reconstruction line with a steering angle of θ, the time of flight t_n for each reconstruction point is described in equation 6.1.

$$t_n(R, x_n, \theta) = \frac{\sqrt{(x_n - Rsin\theta)^2 + R^2cos^2\theta}}{c} \tag{6.1}$$

A second-order approximation is typically used to compute the dynamic delays in terms of t instead of R, shown in equation 6.2.

$$\tau_n(t, x_n, \theta) = -\frac{x_n sin\theta}{c} + \frac{x_n^2 cos^2\theta}{c^2 t} \tag{6.2}$$

The two terms correspond to a steering and a focusing term respectively. At each radial point (described by t) along each reconstruction line (described by x_n and θ), data from transducer elements n are delayed according to $\tau_n(t, x_n, \theta)$, then summed across the elements to form an image point. There are two standard ways to select reconstruction lines: linear-scanned, where the reconstruction lines are perpendicular to the transducer and intersect it at different lateral locations (varying x_n, with $\theta = 0$); and sector-scanning, where all reconstruction lines start at some scanning center, but proceed at different angles (varying θ, usually with $x_n = 0$).

This reconstruction technique suffers in the near field where the delay approximation breaks down. It is common to use a constant f-number reconstruction [1], where the number of elements used at a distance d from the aperture is determined by an aperture width $w = \frac{d}{f_\#}$, where $f_\#$ is typically a constant greater than unity.

6.2.2 Photoacoustic beamforming

In PA imaging, excitation can be considered instantaneous, since light propagation is five orders of magnitude faster than ultrasonic propagation. Put another way, $R = ct$. Ultimately, this results in an approximation in equation 6.3, differing from a US beamformer by a factor of $\frac{1}{2}$ in the focusing term [4].

$$\tau_n(t, x_n, \theta) = -\frac{x_n sin\theta}{c} + \frac{x_n^2 cos^2\theta}{2c^2 t} \tag{6.3}$$

6.2.3 Applying ultrasound beamformers to photoacoustic imaging

In commercial US systems, the raw delays are inaccessible to the user, typically pre-programmed in a lookup table accessed by beamforming hardware. One way to work around this is to modify the speed of sound parameter (c) available on some US systems to form a better photoacoustic image. For the purpose of this discussion, $c = ac_0$ is the speed of sound used in a US beamformer, where a is a user-specifiable scaling factor and c_0 is the true speed of sound in the medium. When using a US beamformer for PA imaging, the depth scale reported will be improperly generated due to the differing calculation of R. Thus, three potential values of a will be explored for PA imaging, informed by the beamforming equations and depth-scaling concerns:

1. $a = 1$, where steering term will match a PA beamformer, but the focusing term will be off by a factor of $\frac{1}{2}$, resulting in sub-optimal focusing and incorrect depth-scaling.

2. $a = \sqrt{2}$, chosen to give the correct focusing term. For a linear-scanned approach ($\theta = 0$), this reduces equation 6.2 to equation 6.3, but for

sector-scanning, performance may degrade when the steering term becomes significant. Depth-scaling is off by a factor of $\frac{1}{\sqrt{2}}$.

3. $a = 2$, chosen to give correct depth-scaling. Neither the focusing nor the steering term are ideal.

There is no choice of a that will give an exact PA solution for the US beamformer. Thus, using $a = \sqrt{2}$, imaging quality will degrade at angles where the steering term is more significant. For linear-scanning, simple depth scaling by $\sqrt{2}$ can be used, but the difference in the steering term for sector-scanning causes some image warping. Conceptualizing equation 6.2 as a combination of steering and focusing effects, it may be appropriate to instead warp display coordinates by reconsidering the steering angle. This approach requires displaying the image using coordinates (r', θ'), where $r' = \frac{2}{a}r$ and $\theta' = sin^{-1}(\frac{sin\theta}{a})$.

6.3 Setup

6.3.1 Experiments

A simplified diagram of the system setup is shown in Figure6.1. Note that beamforming is accomplished by software on the host, whereas a typical ultrasound system would use hardware beamforming, providing only the m beamformed channels for display on the host, rather than the n raw data channels. This configuration allows us to compare a true PA beamformer to a scaled-c US beamformer.

A single human hair (diameter $\sim$100μm) was affixed to a rectangular acrylic frame which was rigidly attached to an optical table and immersed in a water bath. The hair was positioned such that incident light illuminated the hair from its axial direction. Light was provided at a wavelength of 700nm and a measured fluence of about 20mJ/cm^2 (the ANSI limit for human expo-

sure at this wavelength) with 2-4ns pulse duration from an optical parametric oscillator (Surelite OPO Plus, Continuum, Santa Clara, CA, USA) pumped by 532nm laser light provided by a frequency-doubled 1064nm laser (Surelite III, Continuum, Santa Clara, CA, USA) at a repetition rate of 10Hz. An ATL HDI-5000 compatible 128-element L7-4 38mm linear array transducer probe with 6mm elevation width (AT5L40B, Broadsound Corporation, Jupei City, Hsinchu, Taiwan) was affixed to a 3-axis translation stage so that the transducer array was positioned perpendicular to the hair to obtain a point-spread function. Data acquisition was accomplished using a VDAS-1 ultrasound acquisition system (Verasonics, Redmond, WA, USA) triggered by the synchronization output of the laser at 20MHz acquisition rate with 64-channel capture. Due to this limitation, two laser pulses were used in the formation of each image to get data across the full 128-channel aperture. Data from the VDAS system are transmitted to a six-core Intel core i7-980X-based host computer equipped with 12GB of RAM for processing and real-time display. This experimental setup allows us to quickly deploy different reconstruction methods in software at real-time display rates of up to 90 frames per second.

The transducer was moved relative to the hair and a minimum of 30 frames of data were captured at 9 positions every 5mm vertically and 5 positions every 5mm horizontally. Another experiment was done at the same depths with the lateral position of the hair centered for resolution measurements.

6.3.2 Reconstruction parameters

Reconstruction is done according to the beamforming described in section 6.2.1. For both sector and linear-scanned reconstruction, the constant f-number (with $f_{\#} = 1.3$) approach is applied. For the purposes of a fair comparison, the f-number used for ultrasound c-scaled reconstruction is scaled by $\frac{a}{2}$ to give the proper f-number in the PA image. All images use 512 recon-

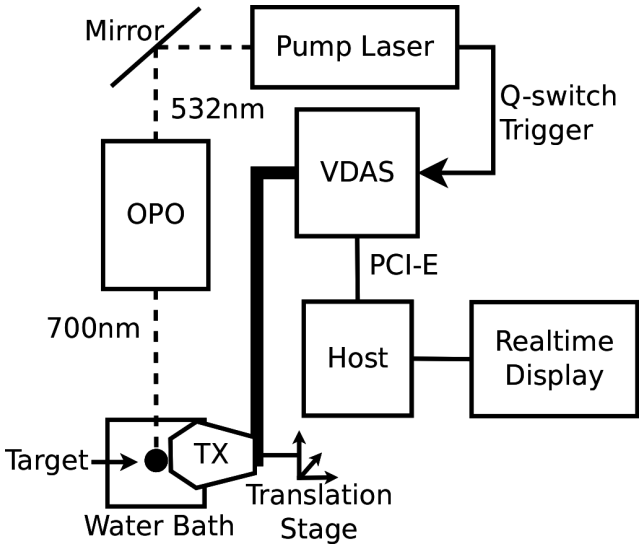

Figure 6.1: Simplified diagram of system setup showing: pump laser (including frequency doubler), optical parametric oscillator (OPO), ultrasound array transducer (TX), acquisition system (VDAS), host computer (Host), and real-time display. The target is a single hair glued across a rectangular acrylic frame.

struction lines: spaced equally along the 38mm aperture for linear-scanning; and distributed equally with $\frac{-\pi}{4} \leq \theta \leq \frac{\pi}{4}$ for sector-scanning. Since sampling in the VDAS-1 system is limited to four times the center frequency of the transducer, the channel data are interpolated by eight times in order to achieve the $\frac{\lambda}{32}$ delay accuracy required to give good focusing characteristics [12].

6.4 Results and Discussion

6.4.1 Resolution

Resolution was quantified by identifying a region of interest for each of the hair images from the centered experimental data set, and calculating the average full-width-half-maximum of 30 data frames measured as the width at the -6dB point. Errors are calculated as the standard deviation of the measurements taken. For the purpose of a conservative comparison, only simple depth-scaling

by $\frac{2}{a}$ is used for sector-scanned reconstruction, as resolution is much worse for the $a = 1$ and $a = 2$ cases with the polar coordinate scaling presented in section 6.2.3.

Results indicate that improvements in linear-scanned lateral resolution of at least 8 times are achievable compared to the unmodified beamformer: a 1 cm deep point compares quite favorably at 0.608±0.01 mm versus 5.0±0.3mm. At a depth of 5cm, the difference is even more apparent: 0.61±0.006mm versus 17.4±0.3mm. For sector-scanning, resolution ranges from 6.2±0.1 to 29.4±0.4mm with $a = 1$, and 0.58±0.01mm to 0.602±0.008mm, a minimum ratio of 10 that improves with depth. For a 16-element aperture, resolution in the non-ideal cases is somewhat better for a smaller active aperture, but $a = \sqrt{2}$ still provides a significant advantage. Small active apertures may explain the relative success that others have had applying unmodified ultrasound beamformers to photoacoustic imaging, as this is similar to using an unfocused transducer with a large $f_{\#}$. Figure6.2 presents typical point spread functions (PSFs) for linear-scanning to show how well the correctly c-scaled beamformer works in comparison to an unmodified and incorrectly-scaled beamformer, with sector-scanning yielding similar results. It should be noted that the PSF for the $a = \sqrt{2}$ case match exactly with that of a photoacoustic beamformer, and that optical turbidity should not impact spatial resolution.

6.4.2 Images

Images were formed by creating a composite image of the reconstructed experimental data. Regions of interest were identified by depth and the reconstructions from different data points are added to a total image. In each image area, the sum of 5 different images are used in each of the 9 areas of interest, for a total of 45 images used to form one composite. For the purposes of display, 30 frames worth of data were averaged before reconstruction.

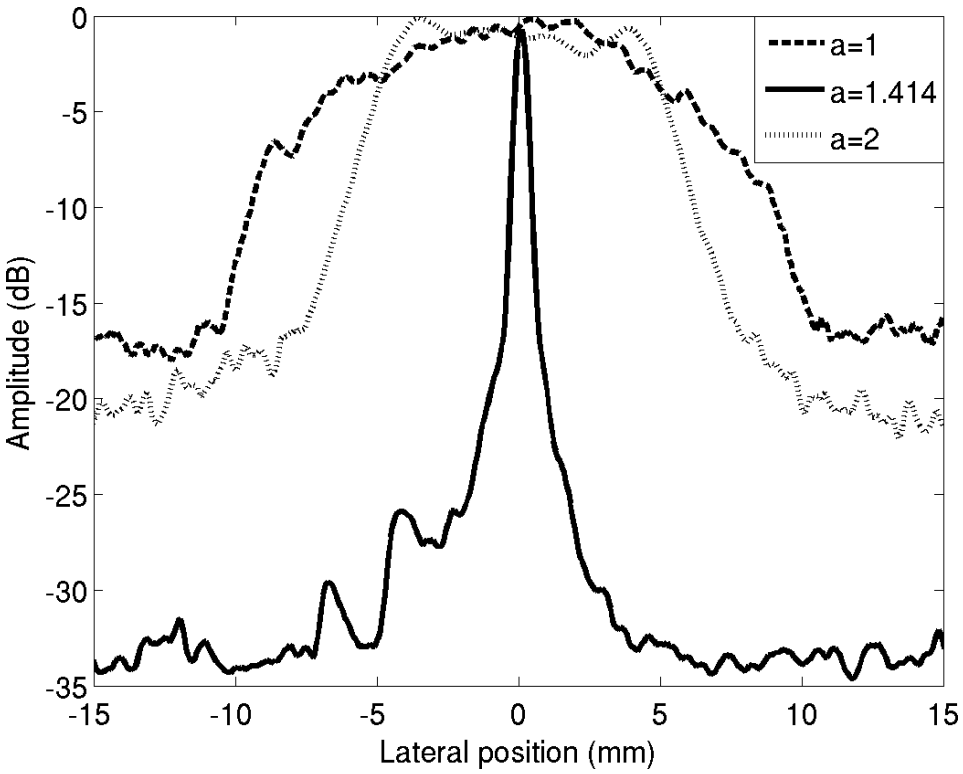

Figure 6.2: Sample linear-scanned point-spread functions for a centered point at 30mm depth for different values of a. Sidelobes in the $a = \sqrt{2}$ case are at about -18dB.

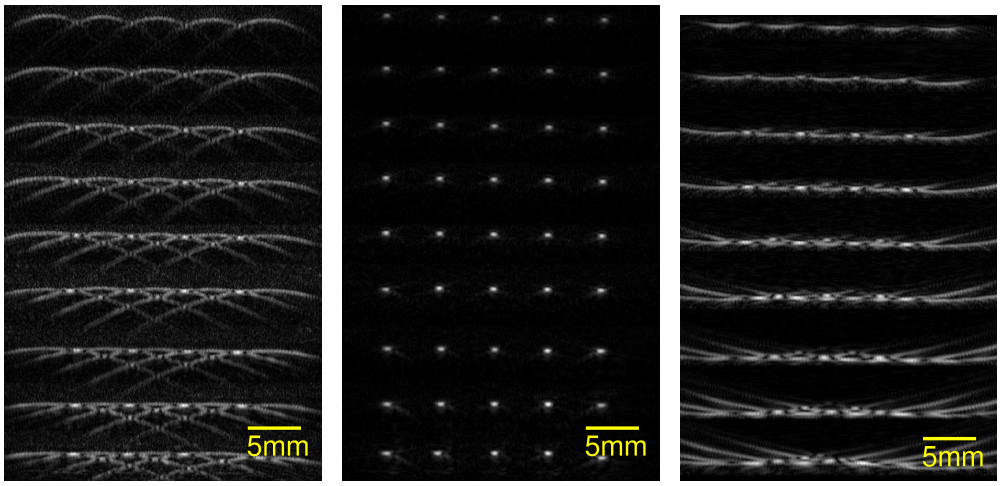

(a) (b) (c)

Figure 6.3: Composite ultrasonically-beamformed linear-scanned images from experimental data with (a) $a = 1$, (b) $a = \sqrt{2}$ (identical to PA beamformer), and (c) $a = 2$.

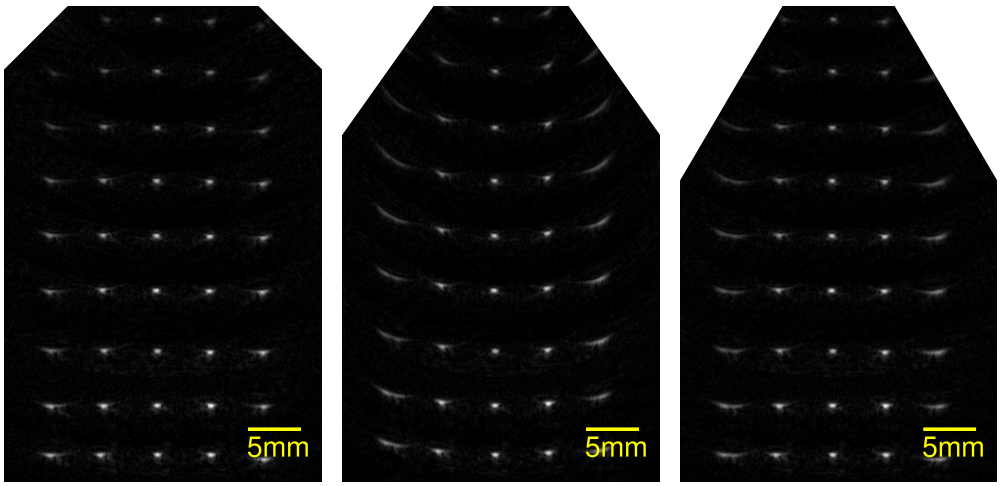

(a) (b) (c)

Figure 6.4: Composite sector-scanned images using (a) PA beamforming, and (b,c) scaled-c US beamformer with $a = \sqrt{2}$ using: (b) simple depth scaling and (c) coordinate re-mapping.

Figure6.3 shows linear-scanned images formed using varying values of a. The advantages of using an a-value of $\sqrt{2}$ seem quite apparent, even from a cursory inspection of the generated images. In fact, this case results in a pixel-by-pixel identical image to the PA beamformer. Resulting sector-scanned

images for the $a = 1$ and $a = 2$ case are similar to the linear-scanned images, so results from only the a=$\sqrt{2}$ case with depth-scaling and coordinate re-mapping are given in comparison to a photoacoustic beamformer in Figure6.4. The simply depth-scaled sector-scanned reconstruction is slightly different from the ideal PA beamformer, both in terms of depth-scaling, and in the performance for points off the center axis as in Figure6.4(b). Hairs located at a significant θ are not placed correctly in depth, and are not reconstructed ideally due to the influence of the steering term from equation 6.2. Displaying the image using warped coordinates (r', θ'), as described in section 6.2.3, gives a more satisfactory reconstruction as shown in Figure6.4(c).

6.5 Conclusions

The effect of using a speed of sound scaling parameter, a, on the reconstruction of PA images using a US beamformer based on an approximated time-of-flight calculation has been investigated. In the case of linear-scanned reconstruction where reconstruction lines are unsteered, use of $a = \sqrt{2}$ combined with depth-scaling by a factor of $\sqrt{2}$ can yield a reconstruction identical to that of a PA beamformer. For a sector-scanned approach, an exact match with PA beamforming is more difficult since the steering term plays a role. Warping the image post-beamforming by displaying it using polar coordinates (r', θ') where $r' = \frac{2}{a}r$ and $sin\theta' = \frac{sin\theta}{a}$ offers a correction for some of the positional inaccuracy resulting from the influence of the steering term. This does not exactly match a PA beamformer, but it gives images that are satisfactory for small reconstruction angles. The presented method may offer a means of implementing PA imaging in commercial US systems without significant hardware modification provided laser-US system trigger capabilities are present.

References

[1] Suhyun Park, Salavat R Aglyamov, and S. Emelianov. "Beamforming for Photoacoustic Imaging Using Linear Array Transducer". In: *IEEE Ultrasonics Symposium Proceedings*. Vol. 1. IEEE, Oct. 2007, pp. 856–859. ISBN: 978-1-4244-1383-6. DOI: 10.1109/ULTSYM.2007.219.

[2] Joel J. Niederhauser, Michael Jaeger, and Martin Frenz. "Comparision of laser-induced and classical ultasound". In: *Proc. SPIE* 4960 (2003), pp. 118–123. ISSN: 0277786X. DOI: 10.1117/12.483509.

[3] S Park. "Integrated system for ultrasonic, photoacoustic and elasticity imaging". In: *Proceedings of SPIE*. Vol. 6147. SPIE, 2006, pages. DOI: 10.1117/12.661508.

[4] Roger J Zemp et al. "Photoacoustic imaging of the microvasculature with a high-frequency ultrasound array transducer". In: *Journal of biomedical optics* 12.1 (2007), p. 010501. ISSN: 1083-3668. DOI: 10.1117/1.2709850.

[5] Liang Song et al. "Fast 3-D dark-field reflection-mode photoacoustic microscopy in vivo with a 30-MHz ultrasound linear array." In: *J. Biomed. Opt.* 13.5 (2008), p. 054028. ISSN: 1083-3668. DOI: 10.1117/1.2976141.

[6] Roy G M Kolkman et al. "Real-time in vivo photoacoustic and ultrasound imaging." In: *J. Biomed. Opt.* 13.5 (2008), p. 050510. ISSN: 1083-3668. DOI: 10.1117/1.3005421.

[7] Rachel Bitton et al. "A 3-D high-frequency array based 16 channel photoacoustic microscopy system for in vivo micro-vascular imaging". In: *IEEE Trans. Med. Imag.* 28.8 (Aug. 2009), pp. 1190–7. ISSN: 1558-0062. DOI: 10.1109/TMI.2008.2011899.

[8] S. Vaithilingam et al. “Three-dimensional photoacoustic imaging using a two-dimensional CMUT array”. In: *IEEE Trans. Ultrason., Ferroelectr., Freq. Control* 56.11 (2009), p. 2411.

[9] Komel P Köstli and Paul C Beard. “Two-dimensional photoacoustic imaging by use of Fourier-transform image reconstruction and a detector with an anisotropic response.” In: *Appl. Optics* 42.10 (Apr. 2003), pp. 1899–908. ISSN: 0003-6935.

[10] J.J. Niederhauser et al. “Combined ultrasound and optoacoustic system for real-time high-contrast vascular imaging in vivo”. In: *Medical Imaging, IEEE Transactions on* 24.4 (Apr. 2005), pp. 436–440. ISSN: 0278-0062. DOI: 10.1109/TMI.2004.843199.

[11] Todd N Erpelding et al. “Sentinel lymph nodes in the rat: noninvasive photoacoustic and US imaging with a clinical US system.” In: *Radiology* 256.1 (July 2010), pp. 102–10. ISSN: 1527-1315. DOI: 10.1148/radiol.10091772.

[12] S R Freeman et al. “Delta-sigma oversampled ultrasound beamformer with dynamic delays.” In: *IEEE Trans. Ultrason., Ferroelectr., Freq. Control* 46.2 (Jan. 1999), pp. 320–32. ISSN: 0885-3010. DOI: 10.1109/58.753020.

Chapter 7

A least-squares fixed-point iterative algorithm for multiple illumination photoacoustic tomography

7.1 Introduction

Photoacoustic tomography holds great promise for quantitative optical imaging as it provides high quality images deeper in tissue than other optical contrast techniques. The images recovered directly from the data are actually estimates of the initial pressure distribution, which is a well-understood problem [1, 2, 3]. However quantitatively estimating optical absorption can be very difficult [4], as fluence is related to both optical absorption and scattering, and the Grüneisen parameter cannot be measured directly. In fact, it is been sug-

A version of this chapter has been published. Harrison et al. 2013. Biomedical Optics Express. 4(10): 2224-2230.

gested by Bal and Ren that without multiple wavelengths, it is impossible to estimate more than two of the three contributing factors to initial pressure distribution (absorption, scattering, and the Grüneisen) uniquely [5].

Several attempts have been made at non-iterative solutions [6, 7, 8] , but due to the interrelation between absorption and local fluence, iterative approaches have also shown some success [9, 10]. However, experimental work by Jetzfellner et al. [11] concluded that errors in optical scattering estimates can result in non-convergence. Multiple wavelengths have been used by Cox et al. [12] to recover absorption and scattering, and Bal and Ren [13] have proposed a method for also reconstructing the Grüneisen parameter.

Bal and Uhllmann posited that diffusion coefficients can be stably reconstructed from internal data (i.e. photoacoustic images) corresponding to a number of well-chosen boundary conditions (i.e. illuminations) [14]. Zemp introduced a ratiometric non-iterative method for reconstructing absorption distributions using multiple-illumination photoacoustic tomography (MIPAT) [15]. We have also previously discussed reconstruction of absorption, scattering, and Grüneisen distributions, and showed that while single illumination photoacoustic tomography is plagued by absorption-scattering non-uniqueness, multiple illumination photoacoustic tomography (MIPAT) can alleviate absorption scattering non-uniqueness and lead to a less ill-posed and better conditioned inverse problem [16]. Unfortunately, the ratiometric non-iterative approach used for quantitative MIPAT image reconstruction [15, 16] was susceptible to noise and applicable only for linearized problems in the diffusion regime with weak perturbations where the first Born approximation is valid. Additionally, iterative algorithms for reconstructing absorption and scattering distributions, suffer from computational complexity, numerical instability, and convergence problems connected with computation and inversion of very large and potentially ill-conditioned Jacobian and Hessian matrices, a

problem that will become worse with larger datasets and with low signal-to-noise measurements. Shao et al. noted that non-ideal pressure reconstructions could lead to errors in quantitative photoacoustic tomography (PAT) and MI-PAT estimates, then proposed an iterative algorithm that uses transducer channel data as a starting point [17]. Cox et al. have extended their previous multiwavelength work to include multiple illuminations as well [4]. Gao et al. introduced a Bregman method for multiple-illumination quantitative PAT [18]. Ren et al. have recently proposed a hybrid method using diffuse optical tomography to establish boundary values for the diffusion coefficient [19]. Still, for all approaches, the aforementioned problems of computational complexity and numerical stability are non-trivial, especially if surrounding optical properties are not well-known.

In this manuscript, we extend the fixed point iteration approach used by both Cox et al. [9] and Jetzfellner et al. [11] to multiple illuminations using an iterative least-squares approach. As was done in those works, we restrict our attention to reconstruction of absorption heterogeneities. Our proposed approach does not require inversion of large ill-conditioned Hessian matrices, is computationally simple, and robust to noise and inaccurate starting parameters, and offers substantially improved convergence properties compared to previous work. We investigate this technique at varying estimates of optical scattering and assess its stability in different noise conditions.

7.2 Theory

7.2.1 Single illumination

Assuming that an initial pressure distribution p_0 has already been reconstructed using any of the various techniques available [1, 2, 3], the problem for a single illumination is to reconstruct the optical absorption μ_a by model-

ing the fluence distribution Φ. The initial pressure distribution is actually a combination of μ_a, Φ and the Grüneisen parameter Γ which for simplicity we assume is uniform and constant. p_0 takes the form in equation 7.1.

$$p_0 = \Gamma \Phi \mu_a \tag{7.1}$$

Reconstruction is complicated by Φ, which should properly be written as $\Phi(r, \mu_a, \mu_s')$: a function varying over spatial position $\boldsymbol{r}$, absorption $\mu_a(\boldsymbol{r})$, and the reduced scattering coefficient $\mu_s'(\boldsymbol{r})$. For the simple iterative technique we are interested in [11], μ_s' is taken to be uniform. As in that work, we assume the diffusion equation is applicable, and use the finite element method solver available in the TOAST toolkit [20] to calculate Φ.

Assuming an initial guess of $\hat{\mu}_a = 0$, the iterative method of [9] proceeds as follows over iterations i: use the forward model to estimate Φ^i; calculate an error parameter $\Delta p_0 = p_0 - \mu_a^{(i)} \Phi^{(i)}$; update $\hat{\mu}_a^{(i+1)} = \frac{p_0}{\Phi^{(i)} + \sigma}$ (where σ is a regularization parameter); and repeat with $i = i + 1$ until the error is within acceptable bounds, or the solution for $\hat{\mu}_a$ has converged.

7.2.2 Extension to multiple illuminations

A similar derivation can be used for multiple illuminations. Consider that a number of detectors are used to reconstruct the initial pressure distributions $\hat{p}_0^k(\boldsymbol{r})$ into an $N \times N$ image due to illuminations $k = 1, ..., S$. The reconstructed initial pressures can be modeled as $\hat{p}_0^k(\boldsymbol{r}) = \Gamma \hat{\Phi}_k(\boldsymbol{r}) \hat{\mu}_a(\boldsymbol{r})$. Here, $\hat{\Phi}_k(\boldsymbol{r})$ is the estimated fluence due to illumination k, and $\hat{\mu}_a(\boldsymbol{r})$ is the estimated optical absorption coefficient distribution. For simplicity, Γ is considered to be spatially constant. From the $M = N^2$ pixels of each of the S reconstructed images, one can form a vector of the observation data $\hat{\boldsymbol{p}}_0 = [\hat{p}_0^1(\boldsymbol{r}_1), ..., \hat{p}_0^1(\boldsymbol{r}_M) ... \hat{p}_0^S(\boldsymbol{r}_1), ..., \hat{p}_0^S(\boldsymbol{r}_M)]^T$.

A vector equation may be formed to model computed initial pressure vectors: $\hat{\boldsymbol{p}}_0 = \hat{\boldsymbol{A}}\hat{\boldsymbol{\mu}}_{\boldsymbol{a}}$, where $\hat{\boldsymbol{\mu}}_{\boldsymbol{a}} = [\hat{\mu}_a(\boldsymbol{r}_1), ..., \hat{\mu}_a(\boldsymbol{r}_M)]^T$ is an $M \times 1$ column vector of estimated optical absorption coefficients, and where $\hat{\boldsymbol{A}} = [\hat{\boldsymbol{A}}_1, ..., \hat{\boldsymbol{A}}_S]^T$ with $\hat{\boldsymbol{A}}_k = \Gamma \times \text{diag}(\hat{\boldsymbol{\Phi}}_k)$, where $\hat{\boldsymbol{\Phi}}_k = [\hat{\Phi}_k(\boldsymbol{r}_1), ..., \hat{\Phi}_k(\boldsymbol{r}_M)]^T$.

The objective is to find $\hat{\boldsymbol{\mu}}_{\boldsymbol{a}}$ such that the error between the observations and the computed images $\epsilon(\hat{\boldsymbol{\mu}}_{\boldsymbol{a}}) = ||\hat{\boldsymbol{p}}_0 - \hat{\boldsymbol{A}}\hat{\boldsymbol{\mu}}_{\boldsymbol{a}}||^2$ is a minimum. The least squares solution to this problem comes from solving $(\hat{\boldsymbol{A}}^T\hat{\boldsymbol{A}})\hat{\boldsymbol{\mu}}_{\boldsymbol{a}} = \hat{\boldsymbol{A}}^T\hat{\boldsymbol{p}}_0$ for the vector $\hat{\boldsymbol{\mu}}_{\boldsymbol{a}}$. Here $\hat{\boldsymbol{A}}^T\hat{\boldsymbol{A}} = \Sigma_k\hat{\boldsymbol{A}}_k^T\hat{\boldsymbol{A}}_k = \Gamma^2 \times \text{diag}(\Sigma_k\hat{\Phi}_k^2(\boldsymbol{r}_1), ..., \Sigma_k\hat{\Phi}_k^2(\boldsymbol{r}_M))$, and $\hat{\boldsymbol{A}}^T\hat{\boldsymbol{p}}_0 = \Sigma_k\hat{\boldsymbol{A}}_k^T\hat{\boldsymbol{p}}_0^k$ with $\hat{\boldsymbol{p}}_0^k = [\hat{p}_0^k(\boldsymbol{r}_1), ..., \hat{p}_0^k(\boldsymbol{r}_M)$. So, given the following form of the least-squares estimate: $\hat{\boldsymbol{\mu}}_{\boldsymbol{a}} = (\hat{\boldsymbol{A}}^T\hat{\boldsymbol{A}})^{-1}\hat{\boldsymbol{A}}^T\hat{\boldsymbol{p}}_0$, we have $\hat{\boldsymbol{\mu}}_{\boldsymbol{a}} = \frac{1}{\Gamma}\text{diag}(\frac{1}{\Sigma_k\hat{\Phi}_k^2(\boldsymbol{r}_1)}, ..., \frac{1}{\Sigma_k\hat{\Phi}_k^2(\boldsymbol{r}_M)})\boldsymbol{B}$ with $\boldsymbol{B} = [\Sigma_k\hat{\Phi}_k(\boldsymbol{r}_1)\hat{p}_0^k(\boldsymbol{r}_1), ..., \Sigma_k\hat{\Phi}_k(\boldsymbol{r}_M)\hat{p}_0^k(\boldsymbol{r}_M)]^T$ and thus we obtain Equation 7.2.

$$\hat{\mu}_a(\boldsymbol{r}) = \frac{1}{\Gamma}\frac{\Sigma_k\hat{\Phi}_k(\boldsymbol{r})\hat{p}_0^k(\boldsymbol{r})}{\Sigma_k\Phi_k^2(\boldsymbol{r})} \tag{7.2}$$

We can incorporate this into an iterative algorithm as follows: from initial fluence estimates $\hat{\Phi_k}^{(0)}(\boldsymbol{r}, \hat{\boldsymbol{\mu}}_a^{(0)})$ computed using a zeroth iteration approximation of optical absorption distribution $\hat{\mu}_a^{(0)}$, we can compute a new estimate of optical absorption coefficients $\hat{\mu}_a^{(1)}$ using the least-squares estimate above. This new estimate can be used to form a new fluence estimate using the diffusion equation or radiative transfer equation, and the process can be iterated until the error is sufficiently small. In order to avoid numerical instability, we introduce a regularization parameter β. β is intended only to ensure long-term convergence of the algorithm which may otherwise diverge due to noise effects, or in the case of experimental work, non-idealities. This results in equation 7.3 for iteration $i + 1$. For this equation, the absorption coefficients are guaranteed to be non-negative given that reconstructed initial pressures are themselves non-negative.

$$\hat{\mu}_a^{(i+1)}(\boldsymbol{r}) = \frac{1}{\Gamma}\frac{\Sigma_k \hat{\Phi}_k^{(i)}(\boldsymbol{r})\hat{p}_0^k(\boldsymbol{r})}{\Sigma_k[\Phi_k^{(i)}(\boldsymbol{r})]^2 + \beta^2} \tag{7.3}$$

7.3 Simulations

Simulations were run in MATLAB using the TOAST [20] finite element-based forward solver for light propagation. In order to verify the simulation code, a similar absorption profile to that used in the Jetzfellner work [11] was simulated. In order to mimic the circular illumination used, 512 point sources located at one transport mean free path within the absorbing body were used. For the multiple illumination simulations, these sources were partitioned to give the appropriate number of images.

In order to measure the accuracy and convergence of MIPAT, we use a normalized root-mean-squared error (NRMSE) of the reconstructed absorption profile. NRMSE is calculated as: $NRMSE = \sqrt{\frac{\sum\sum|\hat{\mu_a} - \hat{\mu_a}^{(i)}|^2}{\sum\sum|\hat{\mu_a}|^2}}$ where the summation is over the entire image, based on the ideally reconstructed absorption, $\hat{\mu_a} = \frac{\sum_k \hat{p_0}^k}{\sum_k \Phi_k}$ (using the known Φ_k from the forward simulation), and $\hat{\mu_a}^{(i)}$, the current quantitative image. This is the same measure as the second quality measure from the work of Jetzfellner et al. [11]. With this metric, we are interested in investigating three things: does increasing the number of sources improve convergence; what effect does the regularization parameter have; and how robust is the technique to noise. Convergence is not guaranteed to be a global minimum, only that the iteration will reach a stopping condition (i.e. further iteration no longer significantly changes the resulting reconstruction).

Our simulation of the experimental work provided very similar results using the same parameters used by Jetzfellner et al. [11] and a similar shaped phantom, shown in Fig. 7.1(a). That is, $\mu_s' = 20\text{cm}^{-1}$, $\mu_a = 1.5\text{cm}^{-1}$ for the inclusion, and $\mu_a = 0.2\text{cm}^{-1}$ for the main body of the phantom. With

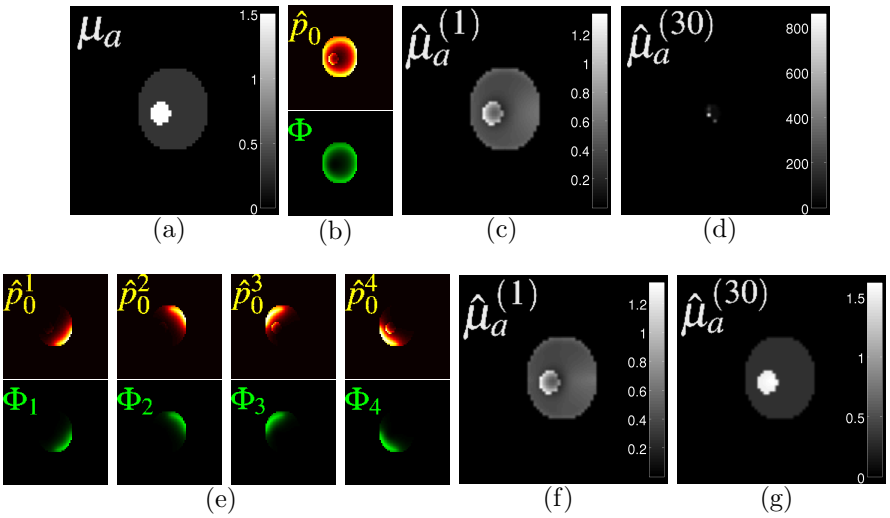

Figure 7.1: (a) μ_a phantom; Single uniform illumination: (b) PA image (top) and true Φ (bottom), (c) first iteration, and (d) 30th iteration. Four illumination MIPAT: (e) PA images (top) and true Φ (bottom), (f) first iteration, and (g) 30th iteration. μ_a in cm^{-1}.

$\sigma = 0.001$, we get very similar results as that work in terms of convergence with the varying estimates of μ_s' used for reconstruction. The most concerning aspect of the previous results is that the reconstruction does not converge even with the correct, uniform $\mu_s' = 20\text{cm}^{-1}$. Figure 7.1(b) shows the initial pressure estimate and true fluence for a single uniform illumination. The first iteration of the algorithm gives a reasonable but inaccurate result seen in Fig. 7.1(c), but after 30 iterations, the solution is clearly diverging as in Fig. 7.1(d). We can instead use the four images with resulting fluences given in 7.1(e). By applying the MIPAT technique detailed above, setting $\beta^2 = \sigma$, and keeping all other parameters the same, we obtain very similar results for the first iteration in Fig. 7.1(f) (this is expected since it is the case with an initial guess of a uniform μ_a), and a much improved estimate of μ_a after 30 iterations in Fig. 7.1(g).

Figure 7.2 shows more detailed results of the MIPAT simulation, comparing normalized root-mean-squared error (NRMSE) to the number of iterations for different numbers of illuminations. From this figure, we see that the previously

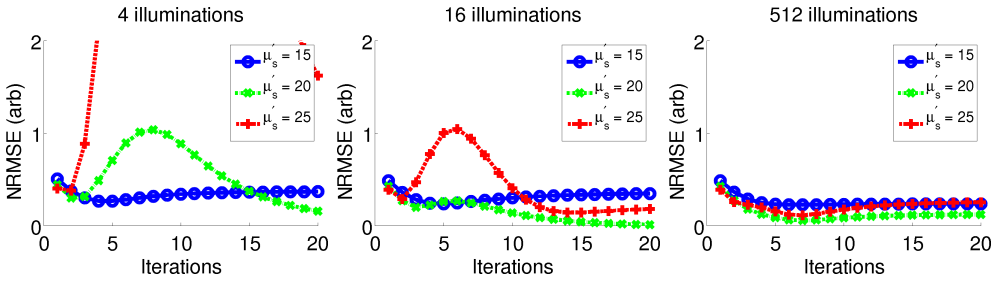

(a) (b) (c)

Figure 7.2: Simulated results of MIPAT with (a) 4, (b) 16, and (c) 512 illuminations with $\beta = 0.032$.

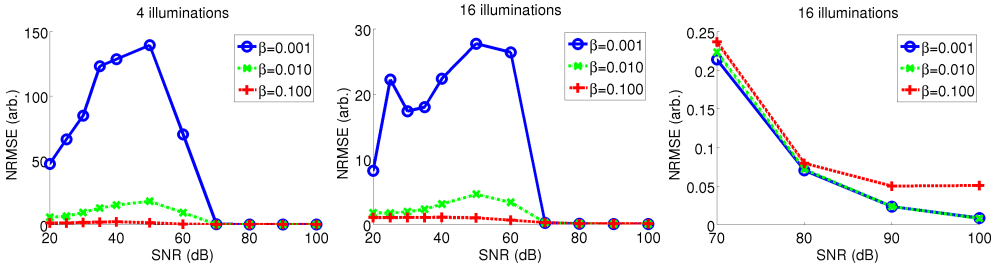

(a) (b) (c)

Figure 7.3: Simulated results of MIPAT after 30 iterations over different image signal-to-noise-ratios (SNR) and β values with (a) 4 and (b) 16 illuminations. The high SNR portion of (b) is presented in (c). Note that here, the standard deviation of the noise added to individual images is equal to that of the uniform illumination case.

non-convergent cases can be made to converge by increasing the number of illuminations using MIPAT techniques. Additionally, the speed of convergence improves with additional illuminations if not the absolute error.

Finally, we investigated the effect of noise on MIPAT reconstruction. As it turns out, β plays an important role in ensuring convergence in this case, so we explored the problem space in two dimensions: both over signal-to-noise ratio (SNR) and β. To make a fair comparison between different MIPAT illumination patterns, for each of S illuminations the total optical power delivered was $\frac{1}{S}$ the power used in the uniform illumination case (Fig. 7.1(b)) while noise levels per image remained the same. More precisely, the standard deviation of the noise added is based on the uniform illumination case at a

level to produce the SNR defined as twenty times the base-10 logarithm of a ratio of signal (maximum signal in this case) to the standard deviation of the noise. This results in an SNR that is lower for each individual image in the MIPAT technique than the uniform illumination image. This should be somewhat equivalent to an experimental setup where portions of the delivered light are blocked to achieve each unique illumination. In cases with convergent solutions, 30 iterations was typically more than enough to demonstrate that behavior, so the root-mean-square error was measured at the 30th iteration for varying values of β and σ. Figure 7.3 shows our results with 4 and 16 illuminations.

7.4 Discussion and conclusions

Figure 7.1(a-b) illustrates the problem that has been previously observed in experimental circumstances: even with a good estimate of μ_s', a simple iterative technique does not necessarily result in a convergent solution. Our simulated results are in very good agreement with experiments from Jetzfellner et al. [11]. Non-convergence with good knowledge of background optical properties is highly problematic, and combined with the non-uniqueness problem that has previously been explored may prevent this technique from being practical.

MIPAT has already been demonstrated as a practical solution to the non-uniqueness problem [16], and our simulated results in Fig. 7.1 and Fig. 7.2 show how introducing multiple images from different optical excitations improves convergence - even where μ_s' is not well-known. While the speed of convergence is similar for the cases presented here, this figure shows that in all cases, the root-mean-squared error is minimized with the correct estimate for μ_s' as one would expect. Figure 7.2 illustrates an interesting behavior of the numerical method: for all values of μ_s' used in the reconstruction, a lo-

cal minimum appears to be reached after two or three iterations before the error measure increases to eventually either diverge or converge to a different value. Indeed, fixed-point iteration numerical methods are not guaranteed to converge at a global minimum, and in fact are not guaranteed to converge at all.

While this improved convergence is an important result, the simulations in Fig. 7.1 and Fig. 7.2 do not include any noise or manipulation of the β regularization parameter. Figure 7.3 demonstrates the effects of SNR and β for 4 and 16 illuminations. In general, the trend that can be seen from these simulations is that increasing β can improve convergence in noisy situations, but that comes at the expense of reconstruction quality. The results seen in the figure are fairly intuitive, showing that low SNR hurts reconstruction quality, as does increasing β. However, there seems to be an ideal β for this set of simulations around 0.01 that provides reasonably accurate convergent solutions in low SNR conditions, while not significantly impacting reconstruction in high SNR conditions. While Fig. 7.3 demonstrates a range of SNR values, low SNR will be more typical of practical systems. In this case, more illuminations and larger regularization parameters are shown to be helpful. The choice of the regularization level using experimental data should be a topic of future work. A value of β that is too high will tend to cause the algorithm to converge in as little as a single iteration while providing inaccurate reconstruction. The choice of these regularization parameters (β for MIPAT and σ for the single illumination case) is certainly non-trivial, and in this work we were guided by the experimental work by Jetzfellner et al. [11], and we do find that the value of β that produced stable, yet accurate results is on the same order of magnitude as the $\sigma = 0.001$ used in that work if we use $\sigma = \beta^2$.

In comparing MIPAT with uniform illumination PAT, we chose to effectively divide the incident optical power into S sources each having $\frac{1}{S}$ of the

available laser power. Even better performance might be expected if all energy of the incident laser were directed to each illumination location, however ANSI standards might limit fluence at each location in practice.

Our proposed algorithm makes no assumptions of simplified models of light transport or weak optical property perturbations. However, for simplicity, the light-propagation simulations used in this manuscript presently use the diffusion approximation. Like the work of Cox et al. [21], future work should assess robustness to cases where optical absorption coefficients are large or comparable to scattering coefficients and cases close to the point of entry, where traditional diffusion-regime approaches fail.

In the present form of the algorithm, reconstructed initial pressure distributions are taken as relatively faithful reconstructions of true initial pressures and it is assumed that there are known calibration factors relating reconstructed signals to true initial pressures. Additionally, no attempt was presently made to account for transducer spatio-temporal impulse-response or to otherwise account for non-ideal initial pressure reconstruction, and is a topic that should be given careful consideration in future work. Despite these limitations, faithful reconstructions were obtained on data which was extremely similar to the experimental data of Jetzfellner et al. [11], offering significant promise.

In this work, we have shown that MIPAT reconstruction can improve convergence over single illumination techniques, even where μ_s' is not well known. Not only that, but our investigation has shown that MIPAT can be used even in realistic noisy images by appropriately selecting the regularization parameter. While this technique does require a somewhat more complicated experimental setup than a single illumination method, the benefits of applying multiple illuminations may outweigh the drawbacks. Compared to previous multiple illumination algorithms, the fixed-point method discussed here does not require inversion of large Jacobian matrices [17, 21] and hence is significantly more

computationally efficient and stable.

References

[1] Minghua Xu and Lihong V. Wang. "Analytic explanation of spatial resolution related to bandwidth and detector aperture size in thermoacoustic or photoacoustic reconstruction". In: *Phys. Rev. E* 67 (5 May 2003), p. 056605. DOI: 10.1103/PhysRevE.67.056605.

[2] L.V. Wang. "Tutorial on Photoacoustic Microscopy and Computed Tomography". In: *IEEE J. Sel. Top. Quant.* 14.1 (2008), pp. 171–179. ISSN: 1077-260X. DOI: 10.1109/JSTQE.2007.913398.

[3] Zijian Guo et al. "Compressed sensing in photoacoustic tomography in vivo". In: *J. Biomed. Opt.* 15.2 (2010), pages. DOI: 10.1117/1.3381187.

[4] Ben Cox et al. "Quantitative spectroscopic photoacoustic imaging: a review." In: *Journal of biomedical optics* 17.6 (June 2012), p. 061202. ISSN: 1560-2281. DOI: 10.1117/1.JBO.17.6.061202.

[5] Guillaume Bal and Kui Ren. "Multi-source quantitative photoacoustic tomography in a diffusive regime". In: *Inverse Probl.* 27.7 (2011), p. 075003.

[6] Jorge Ripoll and Vasilis Ntziachristos. "Quantitative point source photoacoustic inversion formulas for scattering and absorbing media". In: *Phys. Rev. E* 71 (3 Mar. 2005), p. 031912. DOI: 10.1103/PhysRevE.71.031912.

[7] Zhen Yuan and Huabei Jiang. "Quantitative photoacoustic tomography: Recovery of optical absorption coefficient maps of heterogeneous media". In: *Appl. Phys. Lett.* 88.23 (June 2006), pages. ISSN: 0003-6951. DOI: 10.1063/1.2209883.

[8] Biswanath Banerjee et al. “Quantitative photoacoustic tomography from boundary pressure measurements: noniterative recovery of optical absorption coefficient from the reconstructed absorbed energy map”. In: *J. Opt. Soc. Am. A* 25.9 (Sept. 2008), pp. 2347–2356. DOI: 10.1364/JOSAA.25.002347.

[9] Benjamin T. Cox et al. “Two-dimensional quantitative photoacoustic image reconstruction of absorption distributions in scattering media by use of a simple iterative method”. In: *Appl. Opt.* 45.8 (Mar. 2006), pp. 1866–1875. DOI: 10.1364/AO.45.001866.

[10] Lu Yin et al. “Tomographic imaging of absolute optical absorption coefficient in turbid media using combined photoacoustic and diffusing light measurements”. In: *Opt. Lett.* 32.17 (Sept. 2007), pp. 2556–2558. DOI: 10.1364/OL.32.002556.

[11] Thomas Jetzfellner et al. “Performance of iterative optoacoustic tomography with experimental data”. In: *Applied Physics Letters* 95.1 (2009), p. 013703. ISSN: 00036951. DOI: 10.1063/1.3167280.

[12] B. T. Cox, S. R. Arridge, and P. C. Beard. “Estimating chromophore distributions from multiwavelength photoacoustic images”. In: *J. Opt. Soc. Am. A* 26.2 (Feb. 2009), pp. 443–455. DOI: 10.1364/JOSAA.26.000443.

[13] Guillaume Bal and Kui Ren. “On multi-spectral quantitative photoacoustic tomography in diffusive regime”. In: *Inverse Probl.* 28.2 (2012), p. 025010.

[14] G. Bal and G. Uhlmann. “Inverse diffusion theory of photoacoustics”. In: *Inverse Probl.* 26.8, 085010 (Aug. 2010), p. 085010. DOI: 10.1088/0266-5611/26/8/085010.

[15] Roger J. Zemp. "Quantitative photoacoustic tomography with multiple optical sources". In: *Appl. Opt.* 49.18 (June 2010), pp. 3566–3572. DOI: 10.1364/AO.49.003566.

[16] Peng Shao, Ben Cox, and Roger J Zemp. "Estimating optical absorption, scattering, and Grueneisen distributions with multiple-illumination photoacoustic tomography." In: *Applied optics* 50.19 (July 2011), pp. 3145–54. ISSN: 1539-4522.

[17] Peng Shao, Tyler Harrison, and Roger J. Zemp. "Iterative algorithm for multiple illumination photoacoustic tomography (MIPAT) using ultrasound channel data". In: *Biomed. Opt. Express* 3.12 (Dec. 2012), pp. 3240–3249. DOI: 10.1364/BOE.3.003240.

[18] H. Gao, S. Osher, and H. Zhao. "Quantitative photoacoustic tomography". In: *Mathematical Modeling in Biomedical Imaging II: Optical, Ultrasound, and Opto-Acoustic Tomographiess*. Ed. by H. Ammari. Vol. 2035. Lecture Notes in Mathematics: Mathematical Biosciences Subseries. Berlin: Springer-Verlag, 2011, pp. 131–158.

[19] K. Ren, H. Gao, and H. Zhao. "A Hybrid Reconstruction Method for Quantitative PAT". In: *SIAM J. Imaging Sci.* 6.1 (2013), pp. 32–55.

[20] S R Arridge. "Optical tomography in medical imaging". In: *Inverse Probl.* 15.2 (1999), R41.

[21] B. Cox, T. Tarvainen, and S. Arridge. "Multiple Illumination Quantitative Photoacoustic Tomography using Transport and Diffusion Models". In: *Tomography and Inverse Transport Theory*. Ed. by G. Bal et al. Providence, RI, USA: American Mathematical Society, 2012, pp. 1–12.

Chapter 8

S-sequence spatially-encoded synthetic aperture ultrasound imaging

8.1 Introduction

For a given ultrasound imaging system with an array transducer, images may be formed using some combination of transmit or receive focusing. Transmit focusing is limited to a single focal point per transmission, while receive focusing can provide an image that is roughly focused throughout. However, away from the transmit focus the resolution is typically much worse than the ideal system performance. Synthetic transmit aperture imaging sacrifices transmit power for uniform high resolution by using a single element at a time for transmission which allows for a more precise reconstruction [1, 2].

Synthetic aperture imaging provides finer resolution throughout a given

A version of this chapter has been published. Harrison et al. 2014. IEEE Transactions on Ultrasonics, Ferroelectrics, and Frequency Control. 61(5):886-890.

field of view compared to many other ultrasound imaging techniques. However, it does suffer from a typically weak signal-to-noise ratio (SNR) compared to techniques that allow for more transmit power per transmission [3, 4]. One approach to the SNR problem is the use of virtual sources which allow for the use of more transducer elements at once as in the work of Bae and Jeong [5]. In parallel, Chiao et al. introduced spatially-encoded transmissions based on a Hadamard matrix [6], and later temporal encoding using orthogonal Golay codes [7]. Chirped signals have long been used in ultrasound after their introduction by O'Donnell [8], and have been applied to synthetic aperture imaging with some success by Nikolov and Jensen [9].

Temporal encoding has shown great promise, but the work of Nikolov and Jensen found that using Hadamard encoding actually worsened experimental performance [9]. Their explanation was that there may have been nonlinear effects due to the propagation of ultrasound through the water. Moreover, perfectly inverted pulses on a physical ultrasound system are difficult to achieve. With our experimental setup, Hadamard encoding provides yet another obstacle: while individual elements can be turned off or on during transmit, they must all use the same transmit waveform. This is quite limiting in terms of the types of coding that can be used. Techniques that use frequency division, such as those suggested by Gran and Jensen [10, 11], are simply impossible without control of the transmit waveform for each element.

To avoid the implications of asymmetrical transmissions and system limitations, we propose the use of S-sequences for spatial encoding as they do not require an inverted pulse. Our previous work includes simulations that proved this concept [12]. In this work, we show the experimental performance of an S-sequence encoded transmission compared to unencoded, and an approximation of Hadamard encoding using a wire phantom and *in vivo* human carotid as targets

8.2 Theory

The basic principle of spatial encoding for array ultrasound is the simple linear relation $\mathbf{p}^i(t) = \mathbf{E}(t)\mathbf{w}^i + \mathbf{n}(t)$, where: $\mathbf{p}^i(t)$ is a column vector of initial pressures; $\mathbf{E}(t)$ is a matrix composed of elements $e_{kj}(t)$ the received signal due to pulsing element j and receive element k; $\mathbf{w}^i = [w_1^i, w_2^i, ..., w_M^i]^T$ where w_j^i is the weighting applied to element j of M on the i-th transmission which takes a value from $[-1, 0, 1]$ for the encodings discussed here; and $\mathbf{n}(t)$ is a zero-mean additive noise processes. Extending this to a matrix form over M different weightings, $\mathbf{P}(t) = \mathbf{E}(t)\mathbf{W} + \mathbf{n}(t)$, where $\mathbf{P}(t)$ is a matrix with columns $\mathbf{p}^i(t)$, and $\mathbf{W}$ with columns $\mathbf{w}^i$.

It is desired to choose a $\mathbf{W}$ that will maximize signal-to-noise ratio (SNR) in the recovered $\hat{\mathbf{E}}$, while minimizing errors. It has been shown that these constraints require $\frac{\epsilon}{\sigma^2} = tr[\mathbf{W}^{-1}(\mathbf{W}^{-1})^T]$ to be as small as possible, where σ^2 is the noise variance, and $\epsilon = \langle(\hat{\mathbf{E}} - \mathbf{E})(\hat{\mathbf{E}} - \mathbf{E})^T\rangle$ [13].

8.2.1 Hadamard encoding

Hadamard encoding has been suggested as a possible solution[6]. With $\frac{\epsilon}{\sigma^2} = 1$, it theoretically provides improvement over an unencoded solution where $\mathbf{W} = \mathbf{I}$, and $\frac{\epsilon}{\sigma^2} = M + 1$ for an $M \times M$ matrix. Hadamard matrices of order 2^N may be easily constructed using Sylvester's construction given a hadamard matrix of order 2^{N-1}.

Hadamard matrices are easily inverted for decoding, as $\mathbf{H_{2^N}}^{-1} = \frac{1}{2^N}\mathbf{H_{2^N}}$. The rows of $\mathbf{H_{2^N}}$ when used as a set of apodizations will use every element on every transmit, providing up to 2^N times the transmit power. Under a zero-noise condition, this gives a theoretical SNR gain of $10log_{10}(M)$ in dB [6].

To use a Hadamard sequence for imaging, the rows are simply used as a set of apodization functions for the individual elements, requiring some excitation

waveform, and an inverted excitation waveform. Linearity is assumed, so decoding is as simple as applying the inverse matrix to the received data, $\hat{\mathbf{E}}(t) = \mathbf{P}(t)\mathbf{H_{2^N}}^{-1}$.

8.2.2 S-sequence encoding

S-sequences are digital sequences derived from Hadamard sequences. An s-sequence of order $M = 2^N - 1$, $\mathbf{S_{2^N-1}}$ is constructed by taking $\mathbf{H_{2^N}}$, replacing the instances of 1 with 0, -1 with 1, and removing the first row and column (which will be vectors of zeros). This results in a matrix with similar properties to the Hadamard matrix in that it is orthogonal and invertible by $\mathbf{S_{2^N-1}}^{-1} = \frac{1}{2^N}\left[2\mathbf{S_{2^N-1}}^T - \mathbf{J}\right]$, where $\mathbf{J}$ is an appropriately sized matrix of ones. There are three differences between these two encodings: S-sequences have one fewer rows and columns, s-sequences have only N non-zero elements, and s-sequences do not have any -1 components.

From the formulation of $\mathbf{S_{2^N-1}}$, it is clear that there are tradeoffs compared to using $\mathbf{H_{2^N}}$. One element will not be used for S-sequence imaging, and the amount of power that can be used per transmit event will be halved. In this case for an $M \times M$ S-sequence, $\frac{\epsilon}{\sigma^2} = \left[2 - \frac{2}{M+1}\right]^2$, which for a large M, approaches 4. Theoretically, the maximum noiseless SNR increase should be $\sqrt{\frac{M+1}{2}}$, or $10 \times log_{10}(M+1) - 1.5$. This is actually only 1.5 dB less than the SNR improvement that is expected in Hadamard encoding if the same N is used to generate $\mathbf{S_{2^N-1}}$ and $\mathbf{H_{2^N}}$. The tradeoff comes from the conditioning of the matrix inversion. The condition number, $\kappa_2(\mathbf{S_M}) = \sqrt{M+1}$, assuming L^2 norms. In contrast, $\kappa_2(\mathbf{H_M}) = \kappa_2(\mathbf{I}) = 1$. This may result in an increase in error using S-sequence encoding. Nevertheless, S-sequences are slightly easier to implement, faster to decode (since half the elements used for Hadamard encoding are inactive per transmission and thus do not need to be used in the decoding), and avoid the inverted pulses required for Hadamard encoding.

8.3 Setup

8.3.1 System details

We use a Verasonics VDAS I ultrasound acquisition system (Verasonics Inc, Redmond, WA) as the base system for our experiments. The system is capable of simultaneous transmission on up to 256 channels, and reception on 128. We couple this with an ATL L7-4 compatible transducer (Broadsound Corporation, Hsinchu, China) operating at a 5 MHz center frequency. The acquisition rate is set to 20 MHz (four times the transmission frequency) for these experiments.

Images for each of synthetic aperture, Hadamard spatially encoded synthetic aperture, and S-sequence encoded synthetic aperture techniques are captured in rapid succession. The imaging sequence used for each of these operates at approximately 8.5 kHz when imaging at a depth of 6cm, and 127 or 128 transmit/receive events are used. Imaging time is therefore $\sim$15 ms for synthetic aperture and s-sequence coded imaging. Due to the previously mentioned limitations on transmit waveforms, Hadamard encoding is achieved by transmitting the positive waveform on the appropriate array elements, then transmitting the negative waveform and combining the raw data from both transmissions. Thus, twice as many transmissions are used, and each frame is captured in $\sim$30 ms. Two cycles of a 5 MHz sinusoid are used as excitation. There is a delay set between each image capture event that limits the imaging frame rate to 5 fps, but this could be as fast as 66 fps for S-sequence or unencoded synthetic aperture imaging. Image degradation may occur due to tissue motions larger than a fraction of a wavelength, precluding the use of synthetic aperture methods for cardiac and other applications unless a sparse transmit scheme is considered.

Raw image data are stored and post-processed using MATLAB to decode

the received data where applicable. The resulting data are beamformed into 1024 scanlines perpendicular to and spanning the transducer face using the beamforming toolkit from Jensen and Nikolov [14].

8.3.2 Wire target

A wire target ($\varnothing \approx 200\mu$m) was fixed between posts, immersed in water, and attached to a 3-axis stage. The transducer was carefully aligned with the wire target such that the transducer face was perpendicular to the x-y plane of the stage. The stage was scanned vertically, and 10 frames of each imaging technique were captured at 5 mm intervals from $\sim 5 - 55$ mm in depth.

SNR is quantified as $SNR = 20 \times log_{10}\left(\frac{\max(\text{image})}{\sigma_{\text{noise}}}\right)$ with the noise region selected from the image of the wire at around the same depth as the point. Lateral resolution is characterize by the full-width-half maximum of the cross range maximum amplitude.

8.3.3 In vivo

For *in vivo* validation, a section of interest showing the carotid artery and surrounding structure was located using conventional ultrasound imaging. The three synthetic aperture techniques were then performed in rapid succession. Quality for the *in vivo* images is characterized by SNR using the carotid area as the noise region.

8.4 Results and Discussion

8.4.1 Wire target

Images produced by all three imaging procedures are visually very similar, as seen in the point images of Figure8.1.

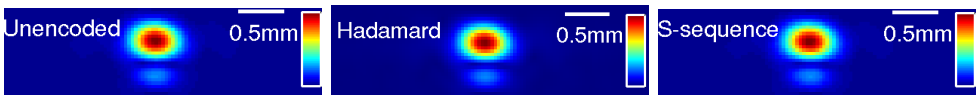

(a) (b) (c)

Figure 8.1: Wire target images at ∼55 mm depth for (a) Synthetic aperture, (b) Hadamard-encoded synthetic aperture, and (c) S-sequence-encoded synthetic aperture.

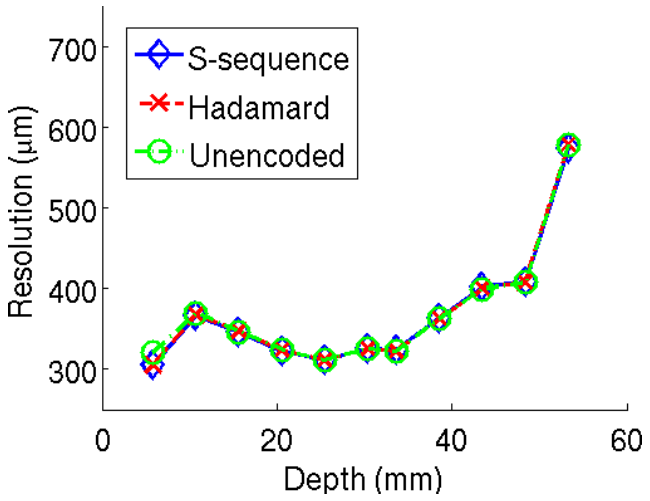

Figure 8.2: Lateral resolution for the three imaging methods.

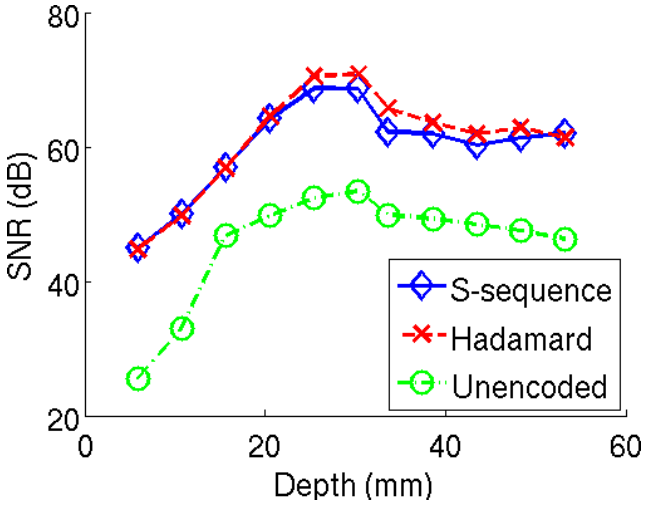

Figure 8.3: SNR for the three imaging methods.

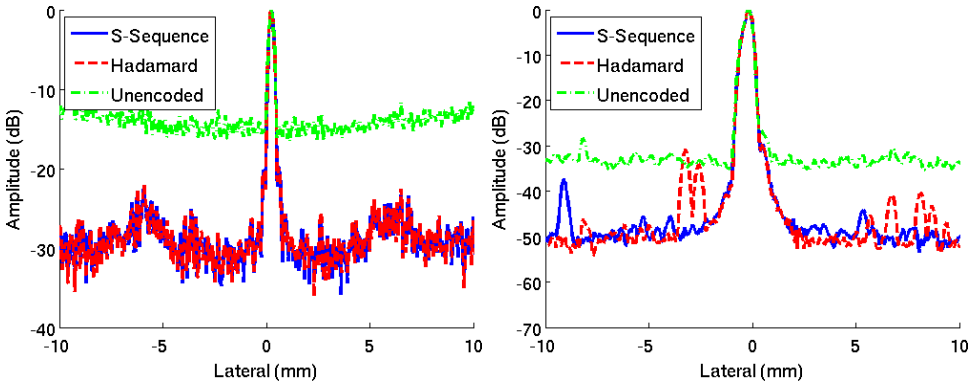

(a) (b)

Figure 8.4: Point-spread functions for wire target at (a) 5mm and (b) 55mm.

Figure8.2 shows that imaging the wire target yielded identical results in terms of resolution for synthetic aperture versus both the encoded methods. This is in agreement with the theory.

SNR results are shown in Figure8.3. In spite of the higher condition number and theoretical 1.5 dB drop in S-sequence encoding, it actually gives approximately the same SNR as Hadamard encoding until after the elevational focus at 25-30 mm. This may be due to the asymmetry of the inverted and non-inverted pulses causing errors to accumulate in the decoding of the Hadamard encoded data, or simply poor beamforming performance in the near-field. Near

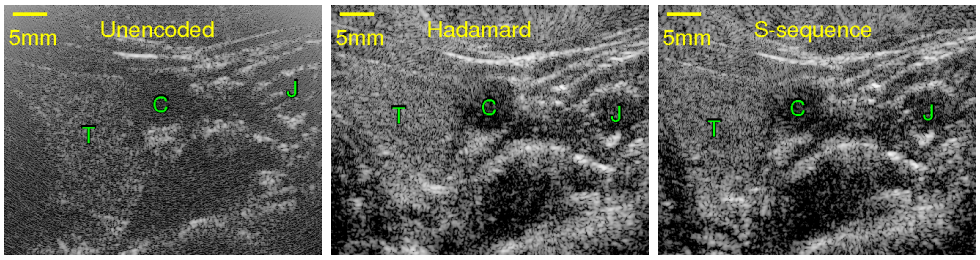

(a) (b) (c)

Figure 8.5: *In vivo* images of human carotid using (a) no spatial encoding (SNR = 36 dB), (b) Hadamard spatial encoding (SNR = 42 dB), and (c) S-sequence spatial encoding (SNR = 44 dB). All images are compressed to 40 dB of dynamic range and displayed on a logarithmic colormap. T: thyroid region, C: carotid artery, J: jugular vein.

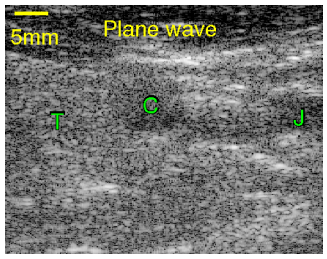

Figure 8.6: Plane wave image reconstructed from first Hadamard image (SNR=32 dB). Image is compressed to 40 dB of dynamic range and displayed on a logarithmic colormap. T: thyroid region, C: carotid artery, J: jugular vein.

the transducer face, the experimental SNR improvement approaches the theoretical improvement of $10 \times log_{10}(2^N) \approx 21$dB for Hadamard encoded imaging, and $10 \times log_{10}(2^N) - 1.5 \approx 19.5$dB for S-sequence encoding, and both give about 19 dB of gain. The SNR improvement for both encodings give at least 10 dB gain.

Point-spread functions are shown in Figure8.4. As noted before, performance for encoded transmission is better in the near field as in Figure8.4(a), but maintains a distinct advantage over unencoded transmission in the far field seen in Figure8.4(b).

8.4.2 In vivo

In vivo images of a human carotid are given in Figure8.5. For the basis of comparison, these have been compressed to the same 40 dB dynamic range and displayed on a logarithmic colormap. The encoded transmissions appear to show more details than the unencoded transmissions. The SNR for the unencoded transmission is 36 dB, compared to 42 dB for the Hadamard, and 44 for the S-sequence encoding. This result is somewhat surprising considering that theory indicates that Hadamard encoding should provide better SNR, but this small of an SNR difference could easily be due to slight motion between image capture events. Figure8.6 shows a plane-wave reconstruction from the first Hadamard sequence image. The SNR is 32 dB from a single excitation, but there is a clear tradeoff between the increased imaging speed and the image quality: many structures that are visible in the Hadamard image are not as well-defined as in the plane wave image.

8.5 Conclusions

We have demonstrated S-sequence spatially-encoded synthetic aperture imaging, a practical alternative to Hadamard encoding. S-sequence imaging does not rely on accurate pulse inversion, and does not require control of waveforms for individual transducer elements, making S-sequences more practical for ultrasound imaging. The performance of S-sequence encoding compares quite favorably to both unencoded and Hadamard encoded imaging. In terms of resolution, performance is virtually identical for all three methods, and in terms of SNR, S-sequence encoding gives approximately the same performance as Hadamard encoding. While Hadamard encoding theoretically gives a 1.5 dB increase and better conditioning, S-sequence imaging is easier to implement experimentally, faster to decode, and in our setup requires half the number of

excitations. While motion artifacts may still be an issue, our *in vivo* images show little indication of this problem due to the very fast imaging speed, and indeed compare quite favorably to plane wave imaging.

References

[1] M. O'Donnell and L.J. Thomas. "Efficient synthetic aperture imaging from a circular aperture with possible application to catheter-based imaging". In: *IEEE Transactions on Ultrasonics, Ferroelectrics and Frequency Control* 39.3 (1992), pp. 366–380. ISSN: 0885-3010. DOI: 10.1109/58.143171.

[2] Moo-Ho Bae et al. "Experimental study of transmit synthetic focusing combined with receive dynamic focusing in B-mode ultrasound imaging systems". In: *IEEE Ultrasonics Symposium*. Vol. 2. 1999, 1261–1264 vol.2. DOI: 10.1109/ULTSYM.1999.849226.

[3] G.R. Lockwood, J.R. Talman, and S.S. Brunke. "Real-time 3-D ultrasound imaging using sparse synthetic aperture beamforming". In: *IEEE Transactions on Ultrasonics, Ferroelectrics and Frequency Control* 45.4 (1998), pp. 980–988. ISSN: 0885-3010. DOI: 10.1109/58.710573.

[4] J. Ylitalo. "On the signal-to-noise ratio of a synthetic aperture ultrasound imaging method". In: *European Journal of Ultrasound* 3.3 (1996), pp. 277–281. ISSN: 0929-8266. DOI: 10.1016/0929-8266(95)00160-S.

[5] Moo-Ho Bae and Mok-Kun Jeong. "A study of synthetic-aperture imaging with virtual source elements in B-mode ultrasound imaging systems". In: *Ultrasonics, Ferroelectrics and Frequency Control, IEEE Transactions on* 47.6 (2000), pp. 1510–1519. ISSN: 0885-3010. DOI: 10.1109/58.883540.

[6] R.Y. Chiao, L.J. Thomas, and S.D. Silverstein. "Sparse array imaging with spatially-encoded transmits". In: *IEEE Ultrasonics Symposium*. Vol. 2. 1997, 1679–1682 vol.2. DOI: 10.1109/ULTSYM.1997.663318.

[7] R.Y. Chiao and L.J. Thomas. "Synthetic transmit aperture imaging using orthogonal Golay coded excitation". In: *IEEE Ultrasonics Symposium*. Vol. 2. 2000, pp. 1677–1680. DOI: 10.1109/ULTSYM.2000.921644.

[8] M. O'Donnell. "Coded excitation system for improving the penetration of real-time phased-array imaging systems". In: *IEEE Transactions on Ultrasonics, Ferroelectrics and Frequency Control* 39.3 (1992), pp. 341–351. ISSN: 0885-3010. DOI: 10.1109/58.143168.

[9] Svetoslav Nikolov and Joergen A. Jensen. "Comparison between different encoding schemes for synthetic aperture imaging". In: *Proc. SPIE* 4687 (2002), pp. 1–12. DOI: 10.1117/12.462151.

[10] F. Gran and J.A. Jensen. "Multi element synthetic aperture transmission using a frequency division approach". In: *IEEE Ultrasonics Symposium*. Vol. 2. 2003, pp. 1942–1946. DOI: 10.1109/ULTSYM.2003.1293297.

[11] Fredrik Gran and Jorgen A. Jensen. "Spatio-temporal encoding using narrow-band linear frequency modulated signals in synthetic aperture ultrasound imaging". In: *Proc. SPIE* 5750 (2005), pp. 405–416. DOI: 10.1117/12.592352.

[12] Roger J. Zemp, Alexander Sampaleanu, and Tyler Harrison. "S-Sequence Encoded Synthetic Aperture B-Scan Ultrasound Imaging". *IEEE International Ultrasonics Symposium*. 2013.

[13] N. J. A. Sloane et al. "Codes for Multiplex Spectrometry". In: *Appl. Opt.* 8.10 (Oct. 1969), pp. 2103–2106. DOI: 10.1364/AO.8.002103.

[14] J.A. Jensen and S.I. Nikolov. “Fast simulation of ultrasound images”. In: *IEEE Ultrasonics Symposium*. Vol. 2. 2000, 1721–1724 vol.2. DOI: 10.1109/ULTSYM.2000.921654.

Chapter 9

S-sequence spatial coding for iterative multiple illumination photoacoustic tomography

9.1 Introduction

One major goal of photoacoustic imaging is the recovery of the optical properties of an imaging subject. Of particular interest is optical absorption, which is directly proportional to the received pressures. However, the initial pressure distribution is determined by $p_0 = \Gamma \mu_a \Phi$, where Γ is the Grüneisen parameter, μ_a is the optical absorption, and Φ is the fluence. All of these may vary spatially, and to complicate matters, Φ depends on the propagation of light through turbid media with spatially varying absorption and scattering coefficients.

Analytical solutions have been attempted [1, 2, 3], but the inverse problem

A version of this chapter has been submitted for publication. Harrison et al. 2014. Journal of Biomedical Optics. 140294P.

is difficult, and the solutions are limited in scope. Iterative approaches show some promise [4, 5] as a more general solution, but suffer from the potential for over-iteration [6] and non-uniqueness [7] problems. We have introduced iterative techniques based on multiple illumination photoacoustic tomography (MIPAT) to tackle both of these problems [7, 8]. Fixed-point iterative techniques like that proposed by Cox et al. [4] and experimentally tried by Jetzfellner et al. are quite sensitive to noise and may diverge with overiteration. The difficulty in applying these iterative techniques may be exacerbated by a MIPAT setup using shutters, or where fluence is already at the ANSI safety limit. The regularization parameter common to these techniques can help ensure convergence under noisy conditions, but negatively impacts reconstruction accuracy.

An increase in the SNR of the initial pressure images provides more robust reconstruction of the optical absorption parameter by allowing a lower regularization parameter to be used. If increasing laser energy is not an option (due to system setup or safety concerns), then one possible solution is to use patterned illumination. We have recently shown that S-sequences can provide nearly the same SNR gain in synthetic transmit aperture ultrasound imaging as Hadamard encoding [9], but without the requirement of pulse inversion. This means that the technique can readily be adapted to photoacoustic imaging, which can only create an initial pressure distribution, and not its inverse. In this work, we apply S-sequences to fixed-point iterative MIPAT and show that the resilience to noise is greatly improved over unencoded imaging. The basic idea is that multiple sources can be used simultaneously and then after a complete set of illumination patterns has been applied, matrix inversion approaches can recover images effectively due to a single source, but with enhanced SNR. The enhanced SNR images can then be used for improved quantitative reconstruction.

9.2 Theory

9.2.1 Fixed-point iterative MIPAT

Fixed-point iteration for MIPAT is a fairly straightforward technique which we have previously proposed [8] based on the original work by Cox et al [4]. Those works may be consulted for a more thorough treatment of the technique. Briefly, the goal is to iteratively reconstruct an estimate of the optical absorption, $\hat{\mu}_a$. To do this, we use sources $k = 1...S$ (where the distribution and type of the sources may be arbitrary, but is known), resulting in reconstructed initial pressure estimates which we call $\hat{p}_0^k$. It is assumed that these pressure estimates (or images) are proportional to the optical absorption by $\hat{p_0}^k = \Gamma \hat{\mu_a} \hat{\Phi}_k$, where Γ is the Grüneisen parameter (taken to be uniform), and $\hat{\Phi}_k$ is an estimate of the fluence. We then iteratively update $\hat{\Phi}_k$ and $\hat{\mu}_a$ at each location $\boldsymbol{r}$ over several iterations i. The algorithm is described as follows:

1. Start with initial guess $\hat{\mu}_a^{(0)}(\boldsymbol{r}) = 0$ ($\cdot^{(i)}$ - iteration number i).

2. Using estimated absorption $\hat{\mu}_a^i(\boldsymbol{r})$, calculate $\hat{\Phi}_k^{(i)}(\boldsymbol{r})$ (in this case, using finite element modeling of optical diffusion from the TOAST toolkit [10]), assuming uniform guess of μ_s'.

3. Update the estimate of absorption coefficients by using a multiple illumination least squares iteration using reconstructed initail pressures and updated fluence estimates as inputs: $\hat{\mu}_a^{(i+1)}(\boldsymbol{r}) = \frac{1}{\Gamma} \frac{\Sigma_k \hat{\Phi}_k^{(i)}(\boldsymbol{r}) \hat{p}_0^k(\boldsymbol{r})}{\Sigma_k [\Phi_k^{(i)}(\boldsymbol{r})]^2 + \beta^2}$, where β^2 is added as a regularization parameter for numerical stability.

4. Repeat 2-4 with $i = i + 1$ until $\Delta \hat{p}_0^k(\boldsymbol{r}) = \hat{p}_0^k(\boldsymbol{r}) - \hat{\mu}_a^{(i)}(\boldsymbol{r}) \hat{\Phi}_k^{(i)}(\boldsymbol{r})$ is sufficiently small.

9.2.2 S-sequence encoding

Now we consider the images, $\hat{p_0}^k$. The previous assumption that the images are properly reconstructed is greatly complicated by concerns of SNR - our previous study showed that to keep a low $\beta = 0.001$, noise levels must be extremely low [8].

The simplest way to increase SNR in photoacoustic images is to increase the fluence used for imaging. This may not always be possible due to hardware or safety limitations. The use of multiple illumination sources opens up an opportunity to easily apply spatially encoded illuminations. To accomplish this, we borrow from previous work using encoded optical spectroscopy [11], and from our work on synthetic transmit aperture ultrasound [9]. In [9], we introduced an encoding scheme based on S-sequences, which has practical advantages over other encoding schemes. Most importantly, an S-matrix only contains binary digits (0 and 1), and thus does not depend on an inverted signal, which is impossible to generate in photoacoustic imaging, since we are constrained to positive fluence values.

The S-matrix used to encode illumination sources is derived from a similarly-sized Hadamard matrix by replacing all '1's with '0's, and all '-1's by '1's, then removing the first row and column (which will all be '0'). S-sequences are rows or columns of the S-matrix. Using the classic Hadamard construction, this constrains us to an $S \times S$ matrix, where $S = 2^n - 1$, $n > 0$,$n \in \mathbb{Z}$. We thus use S successive illumination patterns with S sources to reconstruct a single image. The S-matrix is easily inverted, and thus can be applied to encode, then decode the sources, resulting in a $\hat{p_0}^k$ with potentially up to $10\log_{10}(S+1) - 1.5$ dB improvement in intensity [9].

Thus, we simply add an encoding step before imaging, and a decoding step after imaging to produce higher-SNR $\hat{p_0}^k$ before using the iterative technique. Since all illumination sources and patterns are known, it is possible to directly

use the encoded images in the finite element solver to save some computation time. However, the problem becomes much less well-posed since each image will use $\frac{S+1}{2}$ sources. This results in an illumination that appears much more uniform, especially deep in scattering tissue. Previous analytical work by Bal and Ren similarly stress the importance of illumination choice through constraints on a vector field comparing two illuminations [12]. We therefore expect that the iterative technique will under-perform if the decoding step is not included.

9.3 Simulations

We begin by defining a phantom identical to that used in our previous work: an ellipse of approximately 1.7 by 1.4 cm where $\mu_a = 0.32$ cm^{-1}, with an inclusion of approximately 0.49 by 0.44 cm where $\mu_a = 1.5$ cm^{-1} in a non-absorbing background media. Over the entire field, $\mu_s' = 20$ cm^{-1}. We consider a 70×70 pixel area, representing a 5×5 cm field with incident ring illumination approximated by 315 point sources evenly distributed located one transport mean free path inside the phantom. These sources are simulated individually using the TOAST forward solver (using $n = 1.4$ with Dirichlet boundary conditions), and recombined to form a portion of a ring illumination according to $S = 3, 7, 15, 63$. These intermediate illuminations are either used directly, or recombined again according to the S-matrix to form images.

Noise is added to these images at a level equivalent to the SNR for the ring illumination case (i.e. using the maximum of the sum of image data from all sources to scale Gaussian noise to effectively reach the SNR when all sources are used). This is equivalent to selectively blocking unused sources in an experimental setup, while keeping all other factors the same. This situation might be appropriate when considering ANSI-limited exposure for each illumination.

We then apply the previously described iterative technique, and track the normalized root-mean-squared error defined as $NRMSE = \sqrt{\frac{\sum\sum|\hat{\mu_a}-\hat{\mu_a}^{(i)}|^2}{\sum\sum|\hat{\mu_a}|^2}}$, where $\hat{\mu_a} = \frac{\sum_k \hat{p_0}^k}{\sum_k \Phi_k}$.

9.3.1 Image quality

The first important question to answer is whether or not S-sequence coding confers an SNR advantage over unencoded imaging on a per-image basis. We look at three different scenarios: unencoded images (using multiple single-source illuminations), encoded images (using S-sequence patterned illumination), and images that have been decoded after encoding. Since we are using simulations, we can exactly model the reconstructed image free of noise. This is most important for the decoded signal, where the noise signal will be some linear combination of noise signals from all images and thus the noise signal is not directly available at the time of image formation. SNR can then be characterized for each intial pressure distribution as follows: $\text{SNR} = 20 \times \log_{10}\left(\frac{\max(\hat{p_0}^k)}{\sigma_{\text{noise}}}\right)$.

Figure 9.1 gives a qualitative look at SNR. The top row shows 3 single-source illuminations, while the middle row shows the S-sequence encoded images, both at 40 dB. The encoded images can be decoded to provide the bottom row, with visibly reduced noise compared to the top row. As a general rule, when more sources are used, the unencoded images lose SNR since an increasing amount of the incident fluence is discarded. The encoded images always use about half the available energy, and thus the SNR improvement approaches the added SNR level. One might expect that SNR should be slightly less than the target level which is added based on a uniform illumination, but our definition of SNR using the maximum value is easily achieved using only a few neighboring sources since sources on opposite sides of the phantom contribute little to their respective largest pixel value. The decoded images exhibit very

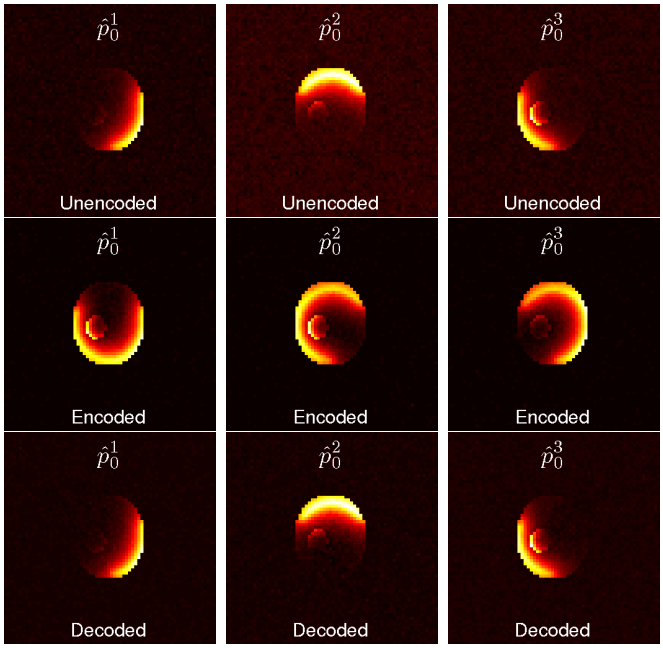

Figure 9.1: **Top:** 3 illumination MIPAT; **Middle:** Encoded 3 illumination case; **Bottom:** Decoded images from middle row, note the visibly reduced noise compare to the top row. Images in top and middle row have white noise of the same variance added (equivalent to ~ 40 dB in the encoded case).

good agreement with the SNR of the encoded images over a wide range of included noise variances, while the unencoded images show a reduction in SNR appropriate for the number of sources. For the 15 illumination case, we see a average SNR increase of ~ 10.3 dB, which is in very good agreement with the predicted increase of 10.5 dB.

9.3.2 Fixed-point iterative MIPAT

We next consider the algorithm performance in the same three cases: using unencoded, encoded, or decoded images in the iterative technique. Figure 9.2 illustrates the behaviour of the technique for the three examined scenarios over 30 iterations. While there is some similarity between the unencoded and decoded scenarios, it is clear that simply using the patterned illumination does not yield good results. Figure 9.3 illustrates the performance over many SNR

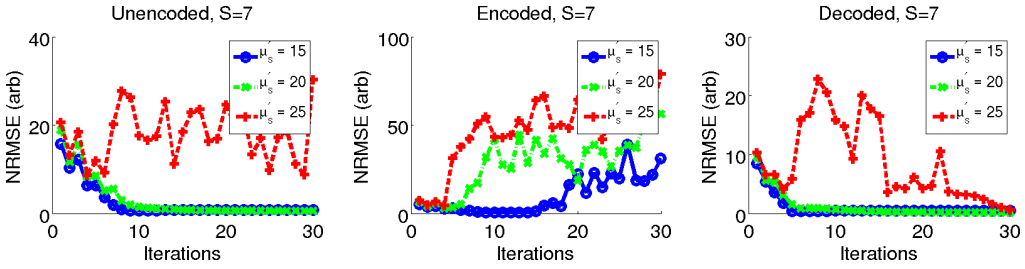

Figure 9.2: NRMSE over 30 iterations for iterative MIPAT with SNR = 50 dB, S = 7, and $\beta = 0.001$. **Left:** using multiple unencoded single-illumination images, **middle:** using S-sequence patterned illumination (no decoding), **right:** using decoded single-source images derived by decoding patterned illumination images.

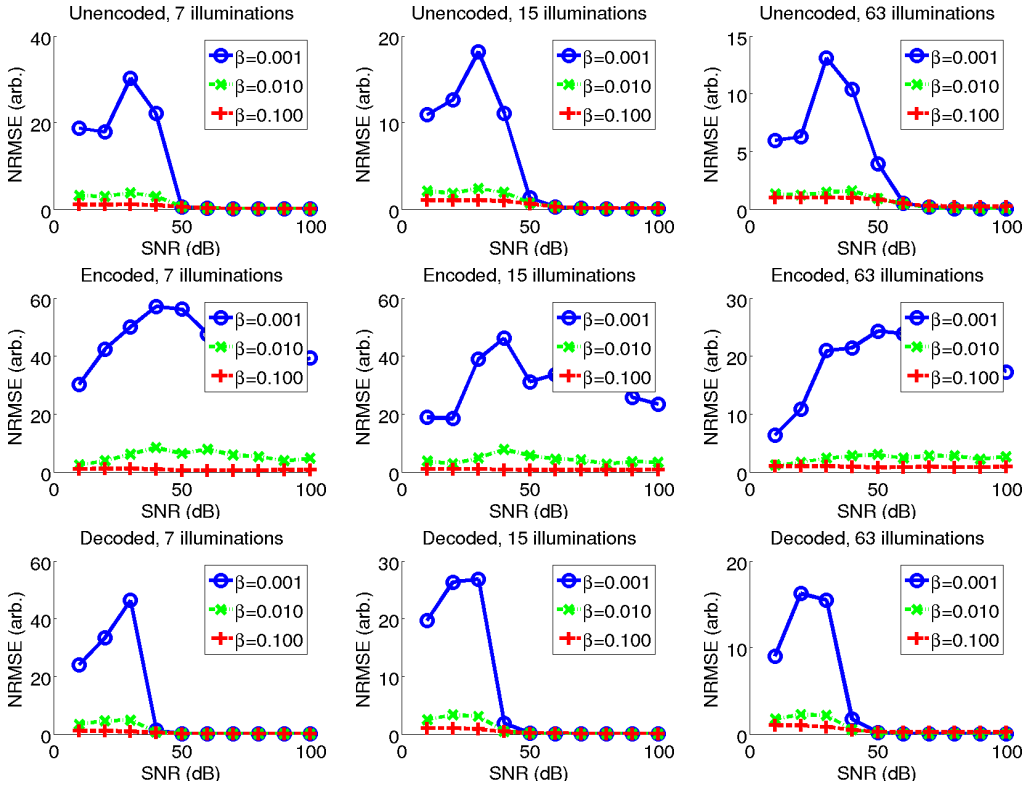

Figure 9.3: NRMSE after 30 iterations for $S = 7, 15, 63$ with $\hat{\mu_s'} = \mu_s' = 20\text{cm}^{-1}$. **Top:** Using unencoded single-illumination images; **Middle:** Using encoded (patterned illumination) images without decoding; **Bottom:** Using decoded patterned illumination images.

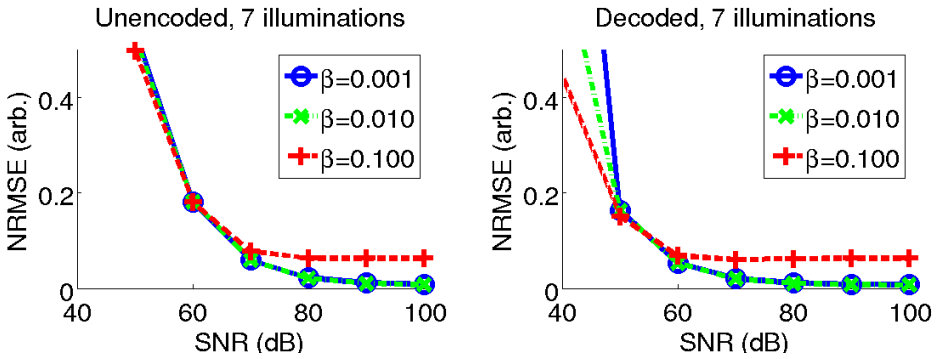

(a) (b)

Figure 9.4: Close-up of $S = 7$ case from figure 9.3 for (a) unencoded (single-source), and (b) decoded images (single-source from patterned illumination). Note the convergence to an inaccurate solution for both cases with $\beta = 0.1$.

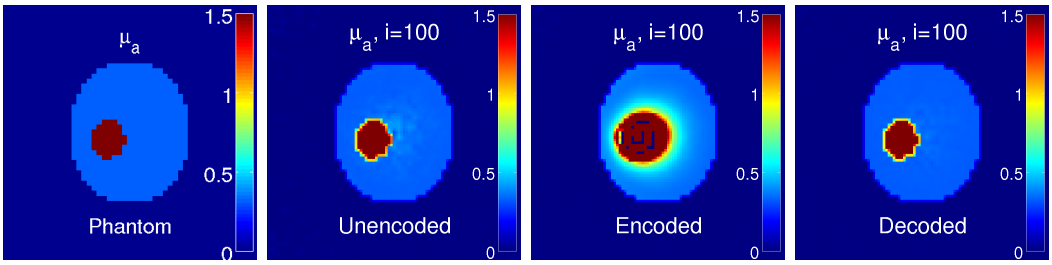

(a) (b) (c) (d)

Figure 9.5: (a) True phantom, and reconstructions after 100 iterations for (b) MIPAT with unencoded multiple illumination images, (c) MIPAT with encoded (patterned illumination) images, and (d) MIPAT with decoded single-source images derived from patterned illumination. SNR is added at 50 dB, $\beta = 0.001$, $S = 7$. Colormaps allowed to saturate beyond 1.5 cm^{-1}, but reach 4 cm^{-1} in (b), 1500 cm^{-1} in (c), and 1.8 cm^{-1} in (d), typically inside the inclusion. Viewable area is limited to $\sim 3.5 \times 3.5$ cm.

conditions. In particular, the $\beta = 0.001$ case is quite interesting. To ensure convergence, the unencoded images require an SNR that increases somewhat with S, requiring roughly 60 dB added SNR in the $S = 63$ case. Running the algorithm with the encoded images actually provides poor reconstruction in even the $\beta = 0.010$ case, which is unsurprising given the similarity in terms of incident fluence for the incident patterned illuminations. It may be difficult to tell from the figures, but the $\beta = 0.100$ case performs quite a bit worse in the encoded case than the other two. Finally, when the decoded images are used, the required SNR for convergence in the $\beta = 0.001$ case appears to be independent of S at around 50 dB. Figure 9.4 shows a closer view of of the unencoded and decoded views. The $\beta = 0.100$ case does appear to favor a less accurate reconstruction, though the other two cases have similar behavior.

An example of the different reconstructions can be seen in figure 9.5 for the different situations. While all figures saturate beyond the maximum true μ_a, the most faithful reconstruction is clearly the decoded image in 9.5(d).

9.4 Discussion and conclusions

Balancing regularization with performance is a difficult task for iterative techniques where single points in the image may introduce numerical instability. Starting with good initial pressure distributions with excellent SNR is one important factor for reducing β in our iterative multiple illumination technique. By applying S-sequence coding, we can recover higher quality images through decoding, as shown in figure 9.1. We find that the encoded and decoded images have similar SNR, and exhibit close to the expected theoretical SNR increase.

Figure 9.2 gives a sense of the speed and general trends of convergence, with the decoded case appearing to converge a bit faster, and possibly forcing convergence in the high μ_s' case. Figure 9.3 shows that we can improve con-

vergence in the $\beta = 0.001$ case by using the decoded images. As expected, the encoded images result in poor performance of the iterative technique, due to the relatively uniform fluence inside the phantom. Figure 9.4 shows the danger of a β that is too high in the $\beta = 0.100$ case, where a relatively poor solution appears to be favored. This raises the very important question of the selection of β. Unfortunately, it is not one that can be answered simply, especially based solely on simulations. Certainly, for a given set of images there is likely to be a value of β which will result in a convergent result, but its value may vary depending on the specifics of the object being imaged, and it may not be clear if the reconstruction is accurate. It is possible, though computationally inefficient to start with a very low β and increase it until numerical instability subsides. Experimental validation and exploration of β in phantom and *in vivo* studies will be required to put this method into practice.

Finally, figure 9.5 shows an example reconstructed $\hat{\mu_a}$ compared to the true μ_a. It is quite clear that the decoded images provide the most faithful reconstruction of the phantom. One thing that is not immediately clear from viewing the figure is that the unencoded and encoded reconstructions have small areas in the inclusion that exceed the true μ_a by orders of magnitude, whereas the use of decoded images results in a more true reconstruction.

We have demonstrated that patterned illumination provides a powerful tool to boost SNR in tomographic systems to a level where fixed-point iterative MI-PAT should be practical with little averaging required. While S-sequences are used here, any sort of binary coding scheme could be used, though other coding schemes may have a worse condition number, increasing the reconstruction error. Patterned illumination is applicable to any multiple-illumination technique, and provides all the advantages of averaging without increasing imaging time.

References

[1] Jorge Ripoll and Vasilis Ntziachristos. "Quantitative point source photoacoustic inversion formulas for scattering and absorbing media". In: *Phys. Rev. E* 71 (3 Mar. 2005), p. 031912. DOI: 10.1103/PhysRevE.71.031912.

[2] Zhen Yuan and Huabei Jiang. "Quantitative photoacoustic tomography: Recovery of optical absorption coefficient maps of heterogeneous media". In: *Appl. Phys. Lett.* 88.23 (June 2006), pages. ISSN: 0003-6951. DOI: 10.1063/1.2209883.

[3] Biswanath Banerjee et al. "Quantitative photoacoustic tomography from boundary pressure measurements: noniterative recovery of optical absorption coefficient from the reconstructed absorbed energy map". In: *J. Opt. Soc. Am. A* 25.9 (Sept. 2008), pp. 2347–2356. DOI: 10.1364/JOSAA.25.002347.

[4] Benjamin T. Cox et al. "Two-dimensional quantitative photoacoustic image reconstruction of absorption distributions in scattering media by use of a simple iterative method". In: *Appl. Opt.* 45.8 (Mar. 2006), pp. 1866–1875. DOI: 10.1364/AO.45.001866.

[5] Lu Yin et al. "Tomographic imaging of absolute optical absorption coefficient in turbid media using combined photoacoustic and diffusing light measurements". In: *Opt. Lett.* 32.17 (Sept. 2007), pp. 2556–2558. DOI: 10.1364/OL.32.002556.

[6] Thomas Jetzfellner et al. "Performance of iterative optoacoustic tomography with experimental data". In: *Applied Physics Letters* 95.1 (2009), p. 013703. ISSN: 00036951. DOI: 10.1063/1.3167280.

[7] Peng Shao, Ben Cox, and Roger J Zemp. "Estimating optical absorption, scattering, and Grueneisen distributions with multiple-illumination photoacoustic tomography." In: *Applied optics* 50.19 (July 2011), pp. 3145–54. ISSN: 1539-4522.

[8] Tyler Harrison, Peng Shao, and Roger J. Zemp. "A least-squares fixed-point iterative algorithm for multiple illumination photoacoustic tomography". In: *Biomed. Opt. Express* 4.10 (Oct. 2013), pp. 2224–2230. DOI: 10.1364/BOE.4.002224.

[9] Tyler Harrison, Alexander Sampaleanu, and Roger J. Zemp. "S-Sequence Spatially-Encoded Synthetic Aperture Ultrasound Imaging". In: 61.5 (2014), pp. 886–890. DOI: 10.1109/TUFFC.2014.2979.

[10] S R Arridge. "Optical tomography in medical imaging". In: *Inverse Probl.* 15.2 (1999), R41.

[11] N. J. A. Sloane et al. "Codes for Multiplex Spectrometry". In: *Appl. Opt.* 8.10 (Oct. 1969), pp. 2103–2106. DOI: 10.1364/AO.8.002103.

[12] Guillaume Bal and Kui Ren. "Multi-source quantitative photoacoustic tomography in a diffusive regime". In: *Inverse Probl.* 27.7 (2011), p. 075003.

Chapter 10

Co-registered photoacoustic-ultrasound imaging applied to brachytherapy

10.1 Introduction

Prostate cancer is a growing concern worldwide. While prostatectomy is a very effective method of treatment, the side-effects can be severe. One alternative treatment is brachytherapy, which is a targeted form of radiation therapy. Unlike traditional radiation therapies where a broad tissue area is exposed to a radioactive source, brachytherapy uses multiple sources to strongly target the tumor area with less impact to the surrounding tissue. The sources for brachytherapy take the form of tiny metallic seeds containing a radioisotope

A version of this chapter has been published. Harrison and Zemp 2011. Journal of Biomedical Optics. 16(8): 080502.

which are implanted in the body according to a treatment plan devised to deliver precise doses to the treatment area. Post-implantation, seed positions within the body relative to other tissues are ascertained in order to evaluate the success of the procedure. In some cases, additional seeds may need to be implanted [1].

Imaging plays a vital role in both seed implantation, and post-implantation dosimetry measures. Ultrasound is often used to guide needles for implantation because it can image the prostate well [1], but needle guidance can be difficult, as incident ultrasound waves may be reflected away from the transducer face, degrading image quality. This same difficulty is also present when imaging brachytherapy seeds. Han *et al.* attempted ultrasound-only dosimetry, and discovered that seeds could only be identified about 74% of the time, with some physicians identifying more seeds than had been implanted [2]. Mamou and Feleppa have attempted to enhance seed detectability with ultrasound, but still have a high false-positive rate [3]. Therefore, other technologies such as CT and MR imaging are used for post-placement verification, but require bulky setups and potentially ionizing radiation. While these imaging modes work well for post-placement verification, manual co-registration with ultrasound is required to allow clinicians to perform treatment adjustments by implantation of further seeds[1]. These modalities are thus ill-suited for realtime applications.

Photoacoustic imaging is a non-invasive imaging modality that provides optical contrast with ultrasonic resolution by measuring pressure waves resulting from localized heating of a sample due to an incident short pulse-duration light source. This modality can be used with multiple wavelengths to separate contrast agents, such as oxy- and deoxy-hemoglobin [4], the principal absorbers deep in tissue through visible wavelengths. While Erpelding *et al.* [5], and Su *et al.* [6] have done work that indicates that photoacoustic imaging may be appropriate for needle guidance at multiple-centimeter depths, the ability

to image smaller metallic objects like brachytherapy seeds has not been fully investigated, though the application has been proposed [6]. Brachytherapy seeds should have a broad absorption spectrum, so either multi-wavelength imaging, or a sufficiently long wavelength should provide good detection of these seeds. This would be a boon for both implantation and post-placement verification, potentially opening the door to realtime dosimetry calculations. Recent conference proceedings from our group and another lab have demonstrated brachytherapy seed imaging in chicken breast [7] and *ex vivo* dog prostate [8] respectively. In this work, we quantitatively asses the suitability of photoacoustic imaging as a complementary modality to ultrasound for the purpose of brachytherapy seed detection at multiple wavelengths.

10.2 Experimental Setup

We evaluated the ability of photoacoustic imaging to form images of titanium-shelled 4.5mm long by 0.8mm diameter brachytherapy seeds (IAI-125A non-radioactive seeds, IsoAid LLC, Port Richey, FL) by imaging at multiple wavelengths and optical penetration depths. Figure 10.1 shows the experimental setup. To compare the contrast of brachytherapy seeds to endogenous contrast, a tube (Intramedic^{TM}, BD, Franklin Lanes, New Jersey, USA) of inner diameter 0.86mm and length 4cm was filled with rabbit blood, placed to the right of the seed, and both were enclosed in chicken breast tissue. Seeds were moved to different positions to simulate various optical penetration depths. This sample was placed in a plastic sample bath containing $\sim$0.5cm of water to maintain moisture in the tissue sample. Resulting realtime (5 frames per second) interleaved photoacoustic and flash ultrasound data were captured using a research ultrasound system (VDAS-I, Verasonics, Redmond, WA) capable of 60MHz capture on 64 parallel channels streamed to a host PC via

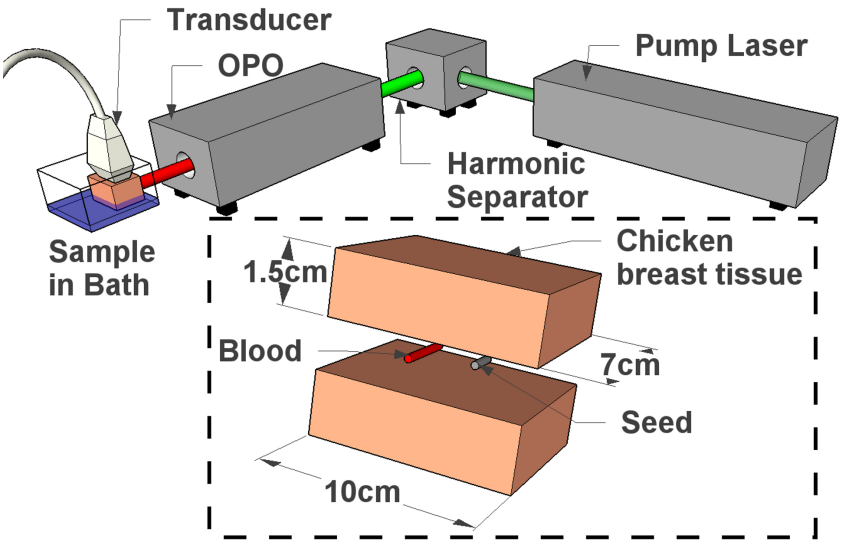

Figure 10.1: System setup. Surelite III pump laser pumps Surelite OPO Plus optical parametric oscillator (Continuum, Santa Clara, CA, USA) providing tunable light at 650-900nm. Incident light interrogates the sample which is in a water bath beneath the 128-element L7-4 38mm (5MHz center frequency, ∼70% fractional bandwidth) linear array transducer (AT5L40B, Broadsound Corporation, Jupei City, Hsinchu, Taiwan). Inset: blown up sample setup with relevant dimensions.

PCI-Express.

Images were then reconstructed using delay-and-sum beamformers on the host PC. Photoacoustic images were thresholded at 40% of maximum intensity, and overlaid in a separate color scale. By viewing combined images and varying this threshold to eliminate endogenous signals, clinicians may be able to identify brachytherapy seeds *in vivo*. Multiwavelength imaging can give clinicians valuable information about not only seed location, but also vasculature around the tumor region.

10.3 Results

Figures 10.2 (a) and (b) show how the seed can be seen with varying intensity levels compared to the blood sample at 760nm and 797nm. In these images, seed-to-blood contrast-to-noise (CNR) were 15dB and -0.5dB respectively. The

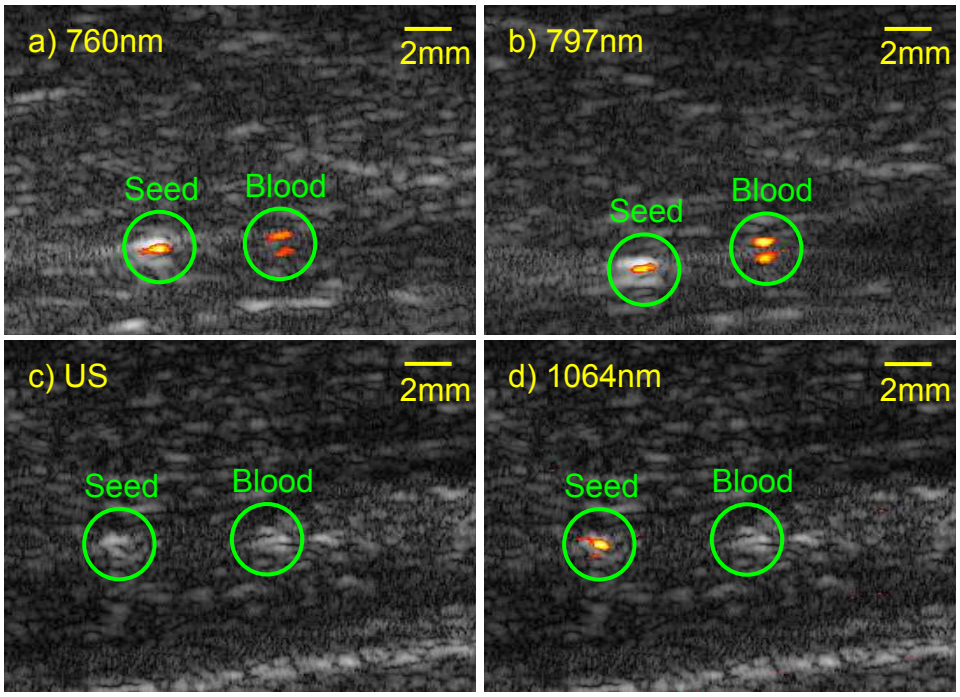

Figure 10.2: (a), (b) Combined ultrasound-photoacoustic images at a laser fluence of 20mJ/cm^2 and a laser penetration depth of 2cm. (c), (d) Ultrasound and combined ultrasound-photoacoustic images at a fluence of 100mJ/cm^2 and a laser penetration depth of 5cm (Video 1, MPEG, 1.1MB).

blood-filled tube appears as two surfaces in these images, whereas the seed appears as a continuous body. In the case of the blood-filled tube, signals are seen from the top and bottom surfaces: an effect in-part due to band-pass filtering effects of the ultrasound transducer. While this same effect should occur for the seed, the acoustic impedance mismatch of metal and tissue causes signals from the bottom surface propogating through the seed to be largely reflected by its top surface, reducing the signal received by the transducer.

Using the 1064nm fundamental output of the pump laser, the blood-filled tube was indistinguishable from noise, while the brachytherapy seed provided a strong signal. Figure 10.2 (c) and (d) illustrate this: while the brachytherapy seed is indistinguishable from the blood-filled tube in the ultrasound image, the overlaid photoacoustic signal correctly identifies the seed. We found that the brachytherapy seeds were detectable using the ANSI exposure limit for

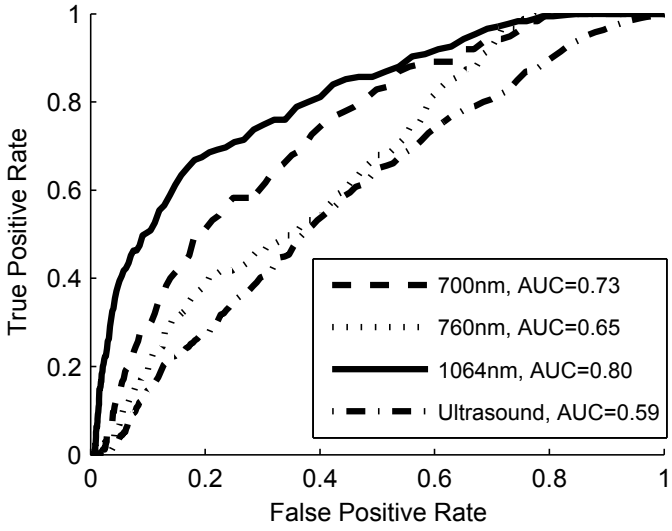

Figure 10.3: Receiver operating characteristic curves for photoacoustic imaging at several wavelengths compared to ultrasound with area under the curve (AUC) annotated in legend.

fluence of 100 mJ/cm^2 at 1064nm to a laser penetration of at least 5cm with a CNR of 26.5dB. Images are captured at a laser-repetition-rate-limited 5 frames per second and displayed in realtime.

As further proof of the effectiveness of photoacoustic imaging for brachytherapy seed imaging, we generated receiver operating characteristic (ROC) curves of representative images for a few of the more promising wavelengths, shown in Figure 10.3. ROC curves are formed by varying the threshold at which a seed is said to be detected, and measuring the true-positive and false-positive rates determined by fractions of pixels above the threshold within and without the seed region. The seed region is located by picking the maximum amplitude in an image and defining a true-scale seed mask around this region. The same mask is applied for both US and PA images. We verified that maximum signals were due to the seed by removal and re-imaging. Performance was characterized by the area under the curve (AUC), annotated in the legend.

10.4 Discussion

Figure 10.2 illustrates that brachytherapy seeds are visible at an intensity similar to endogenous optical contrast. This indicates that separating them using absorption-spectrum-based processing techniques should be possible. Even more promising is higher-fluence imaging at 1064nm, as in Figure 10.2(d), which we have demonstrated at a depth suitable for this application using a safe laser fluence with an excellent CNR. This means that a single wavelength could potentially be used to uniquely identify brachytherapy seeds. The real-time nature of our imaging technique will prove important in clinical settings and may enable continuous feedback for seed position planning. Finally, Figure 10.3 indicates that photoacoustic imaging at 1064nm can offer improved classification performance compared to ultrasound alone.

Chicken breast may not be an ideal tissue analogue for prostate tissue. Values for $\mu_a = 0.078$ mm^{-1} and $\mu_s' = 0.63$ mm^{-1} are typical for human prostate at 1064nm [9]. While we were unable to find literature detailing the optical properties of chicken tissue at 1064nm, values of $\mu_a \approx 0.2$ mm^{-1} and $\mu_s' \approx 0.05$ mm^{-1} have been reported for 1000nm [10]. Applying $\mu_{eff} = (3\mu_a + \mu_s')^{\frac{1}{2}}$ to each substance, we get $\mu_{eff} = 0.41$ mm^{-1} for human prostate at 1064nm and $\mu_{eff} = 0.39$ mm^{-1} for chicken tissue at 1000nm. Using Beer's law, and assuming that μ_{eff} is roughly the same at 1064nm and 1000nm for chicken tissue, we get an expected reduction in signal intensity of 8.7dB for a 5cm depth image in prostate tissue compared to chicken breast. This would result in an SNR of 17.8dB based on our prior measurement of 26.5dB: more than adequate for imaging. While differences in absorption will impact the maximum imaging depth and anisotropy may impact detectability, our preliminary data motivates *in vivo* studies.

10.5 Conclusions

While the application of photoacoustic imaging to brachytherapy seems quite promising based on the data presented here, there are still several hurdles to overcome before this technology can be used in a clinical setting. Heating of the seed region is poorly understood, though it is likely to be highly localized and fast to dissipate. Local laser fluence may be unknown due to optical heterogeneity, impairing image quantification and quality. Light delivery to the prostate is further complicated by its location, likely requiring a rectal delivery probe. In clinical situations, light fluence and US attenuation should be accounted for in image reconstruction. A more rigorous study of multi-wavelength imaging should be undertaken, as well as *in vivo* clinical studies.

References

[1] Donald B Fuller et al. "CT-ultrasound fusion prostate brachytherapy: A dynamic dosimetry feedback and improvement method. A report of 54 consecutive cases". In: *Brachytherapy* 4.3 (2005), pp. 207–216. ISSN: 1538-4721. DOI: 10.1016/j.brachy.2005.07.005.

[2] Ben H. Han et al. "Prostate brachytherapy seed identification on post-implant TRUS images". In: *Medical Physics* 30.5 (2003), p. 898. ISSN: 00942405. DOI: 10.1118/1.1568976.

[3] J. Mamou and E.J. Feleppa. "Ultrasonic Detection and Imaging of Brachytherapy Seeds Based on Singular Spectrum Analysis". In: *Acoustical Imaging*. Ed. by Iwaki Akiyama. Vol. 29. Acoustical Imaging. Springer Netherlands, 2009, pp. 127–132. ISBN: 978-1-4020-8822-3. DOI: 10.1007/978-1-4020-8823-0_18.

[4] Hao F Zhang et al. "Functional photoacoustic microscopy for high-resolution and noninvasive in vivo imaging". In: *Nat. Biotechnol.* 24.7 (July 2006), pp. 848–51. ISSN: 1087-0156. DOI: 10.1038/nbt1220.

[5] Todd N Erpelding et al. "Sentinel lymph nodes in the rat: noninvasive photoacoustic and US imaging with a clinical US system." In: *Radiology* 256.1 (July 2010), pp. 102–10. ISSN: 1527-1315. DOI: 10.1148/radiol.10091772.

[6] Jimmy Su et al. "Photoacoustic imaging of clinical metal needles in tissue." In: *Journal of biomedical optics* 15.2 (2010), p. 021309. ISSN: 1560-2281. DOI: 10.1117/1.3368686.

[7] Tyler Harrison and Roger J. Zemp. "Photoacoustic imaging of brachytherapy seeds using a channel-domain ultrasound array system". In: *Proc. SPIE*. Vol. 7899. 2011, pages. DOI: 10.1117/12.875550.

[8] Nathanael Kuo et al. "Photoacoustic imaging of prostate brachytherapy seeds in ex vivo prostate". In: *Proceedings of SPIE*. Vol. 7964. May. 2011, pages. DOI: 10.1117/12.878041.

[9] William H. Nau, Robert J. Roselli, and Douglas F. Milam. "Measurement of thermal effects on the optical properties of prostate tissue at wavelengths of 1,064 and 633 nm". In: *Lasers in Surgery and Medicine* 24.1 (1999), pp. 38–47. ISSN: 1096-9101. DOI: 10.1002/(SICI)1096-9101(1999)24:1<38::AID-LSM7>3.0.CO;2-G.

[10] K. Ishii et al. "Determination of optical property changes during laser therapies". In: *Lasers Electro Optics The Pacific Rim Conference on Lasers and Electro-Optics, 2009. CLEO/PACIFIC RIM '09. Conference on*. Aug. 2009, pp. 1–2. DOI: 10.1109/CLEOPR.2009.5292314.

Chapter 11

In vivo imaging of inducible tyrosinase gene expression with an ultrasound array-based photoacoustic system

11.1 Introduction

Reporter genes are an important tool for researchers in both the production of transgenic organisms, and the study of cellular pathways. By linking a gene that will cause an easily detectable visual clue with a protein of interest, one can potentially look at local expression levels and gain valuable insight into biology. Measuring localized gene expression deep in tissue is a very important issue in emerging technologies such as gene therapy. With microbubble-aided transfection techniques, it is possible to target microbubbles to specific tissues,

A version of this chapter has been published. Harrison et al. 2012. Proc SPIE. 8223: 82230S.

but it may be difficult to measure the transfection efficiency. It is desirable to be able to measure transfection levels in both target and non-target tissues. The commonly-used fluorescent-protein tagging approaches - while very useful for assessment of transfection on a cellular scale - fall short of being able to provide the image quality necessary for *in vivo* transfection. To this end, chromophore expression measured by photoacoustic imaging provides an attractive alternative: it can provide both the depth, and the sensitivity required to detect transfection, potentially even quantitatively.

While lacZ (which encodes for β-alactosidase) has been explored as a photoacoustic reporter gene, it requires the administration of X-Gal, which can cause irritation, and may be difficult to deliver (i.e. to xenograft tumors) [1]. While fluorescent proteins have also been explored for photoacoustic imaging, the signal strength is typically quite weak [2] due to lack of amplification, leading to imaging difficulties related to multiwavelength techniques in terms of fluence estimation. A better reporter gene would rely on something much more ubiquitous, ideally requiring no introduction of external products. Recently, tyrosinase has been proposed by two different groups as a viable alternative to lacZ [3, 4]. Tyrosinase is a key enzyme in the production of melanin - the natural pigment in human skin. The attractive feature is that tyrosinase acts on a simple amino acid: tyrosine. In fact, tyrosinase alone seems to be sufficient for the expression of melanin, as demonstrated recently in *E. Coli* [5].

Early results with stably transfected cell lines have been promising using a single-element scanning system [3] and optical-resolution photoacoustic microscopy (OR-PAM) [4], but these have not shown results with systems appropriate for deep tissue imaging. In this work, we demonstrate the feasibility of tyrosinase as a reporter gene for photoacoustic imaging with a clinically relevant (in terms of ultrasound frequency and depth penetration) combined ultrasound-photoacoustic array imaging system.

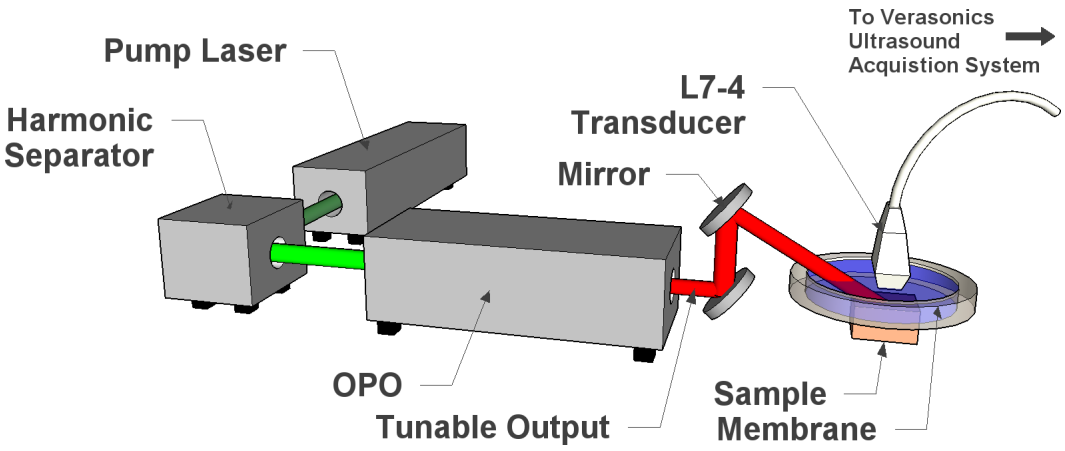

Figure 11.1: Pump laser provides excitation for an OPO, the tuned output of which is used to interrogate the sample photoacoustically, using a linear array transducer to collect resulting ultrasound data.

11.2 System design

11.2.1 Photoacoustic setup

Figure 11.1 shows the photoacoustic imaging setup. The Surelite III Nd:YAG laser with either a frequency doubling or tripling crystal (providing either 532nm or 355nm light) pumps a Surelite OPO Plus optical parametric oscillator (both Continuum, Santa Clara, CA, USA) providing tunable light either from 650-900nm or 410-680nm. The maximum pulse repetition rate of the laser is 10Hz, limiting photoacoustic imaging to a 5Hz frame rate due to limitations in the acquisition hardware. The ultrasound transducer is a 6mm elevation ATL HDI-5000 compatible L7-4 38mm array probe (AT5L40B, Broadsound Corporation, Jupei City, Hsinchu, Taiwan), limited to a lateral resolution of approximately 0.5mm by the center frequency of 5MHz.

11.2.2 Ultrasound acquisition

An ultrasound acquisition system (VDAS-I, Verasonics, Redmond, WA, US) provides programmable acquisition sequences, allowing multiple imaging modes.

We use a custom-programmed interlaced ultrasound-photoacoustic sequence to perform gene expression imaging. Ultrasound pulses are interlaced with photoacoustic acquisition to provide both the structural context of ultrasound and the optical contrast of photoacoustic imaging. In particular, we use ultrasound flash imaging: providing a single plane-wave excitation with only post-reception beamforming to provide focusing. This simplifies reconstruction, as a similar algorithm may be used in both imaging scenarios [6]. While the full 128 elements are available for transmission, only 64 are available at a time for receive, requiring 2 excitations per imaging mode to get a full-aperture image in both imaging modes. Data from the acquisition system are reconstructed in realtime by a combination of MATLAB scripts and complied C code on an Intel Core i7-980X-based host PC. In ultrasound-only imaging modes, display rates of 90-100fps are possible, though our custom reconstruction is currently limited by the 10Hz repetition rate of the laser. Without considering reconstruction, the acquisition system is theoretically capable of a PCI-E bus-limited ultrasound data capture rate at up to 3500fps at a 6cm imaging depth.

The combined imaging mode used in this study requires three steps: ultrasound and photoacoustic data are dynamically beamformed to provide focused images on individual color maps; then, photoacoustic images are interpolated to provide the same depth scale as the ultrasound images (this must be done due to one-way rather than two-way ultrasound propagation in the photoacoustic case); finally, the images are combined by putting the ultrasound images on a logarithmic colormap, and thresholding the photoacoustic images linearly (50% is used as a threshold in this work). In realtime, we typically use an imaging mode that shows ultrasound and photoacoustic data separately.

11.3 Experiments

11.3.1 Design

For all the cell cultures used in this study, the methods used are as described in our previous work [3]. In short, a tetracycline transactivator was attached to the tyrosinase-encoding gene in a line of MCF-7 cells causing expression of tyrosinase in the presence of doxycycline - a drug easily administered in an animal's drinking water. The reason for pursuing an inducible system is twofold: both to show the viability of tyrosinase as a reporter gene linked to a protein of interest, and to avoid the potential concern of cytotoxicity of melanin at high expression levels.

In the first stage of this work, interlaced photoacoustic/ultrasound images of cell suspensions in plastic tubes were imaged using both intralipid and chicken breast tissue to provide reasonable scattering and a rough approximation of *in vivo* tissue respectively. The transparent plastic tubes used were 0.86mm in inner diameter (BD Intramedic^{TM} Polyethylene Tubing PE 90, Franklin Lakes, NJ). Cellular suspensions of the tyrosinase expressing cells (+TYR) and a control line of regular MCF-7 cells (-TYR) were affixed to an acrylic holder, and imaged alongside tubes filled with phosphate buffered saline and rabbit blood. The cellular concentrations were at 10^8 cells/mL. Imaging proceeded at a depth of 2cm in a 1% intralipid solution (reduced scattering coefficient $\sim$10cm^{-1}. To ensure even illumination of each tube, the holder was scanned across the laser spot such that every tube was centered in the illumination, and a composite image was formed based on these data. For wavelengths below 680nm, a fluence of $\sim$7mJ/cm^2 was used, whereas a fluence of $\sim$20mJ/cm^2 was used. From this composite image data, a fluence-corrected comparison of relative absorption across many wavelengths was made. Identical tube preparation was used prior to imaging between layers of chicken breast

tissue (with water used to provide acoustic coupling and without compositing). The blood and tyrosinase-expressing cell culture tubes were placed at a depth of 2.8cm and imaged using the combined imaging mode described earlier in the paper. While the water tank with membrane setup shown in Figure 11.1 is used for animal imaging, it is replaced for the case of tube imaging by a bath of intralipid or nothing for the case of imaging between layers of chicken tissue.

The second stage of experimentation focused on *in vivo* studies. The -TYR and +TYR cells were injected subcutaneously in the left and right flanks of hairless SCID mice (Charles River, Wilmington, MA) after suspension in a 1:1 mixture of phenol red free growth medium and matrigel. After the tumors reached sufficient size for imaging (∼3mm diameter), the drinking water was changed to a 1mg/mL solution of doxycycline for a period of 14 days. After this activation period, animals were imaged. During imaging, the mice were anesthetized with isoflurane, and placed on top of a heating pad, with ultrasound gel providing coupling between the mouse and a gelatin standoff (prepared in the lab, ∼1.5cm thick of 10% 300 bloom gelatin) used to provide appropriate spacing between the mouse and the membrane. Post-imaging, the mouse was then recovered and switched to a drinking water with 0.5% weight/volume ferric citrate for 4 days (for magnetic resonance imaging experiments). After this period, mice were euthanized, and their tumors were excised and fixed in formalin for later visual examination.

11.3.2 Plastic tube experiments

Combined ultrasound/photoacoustic images of the plastic tubes with blood and phosphate-buffered saline (PBS) controls are shown in Figure 11.2, resulting in the corresponding relative signal levels as shown in Figure 11.3. For the presented images, the ultrasound images were used to find the center of

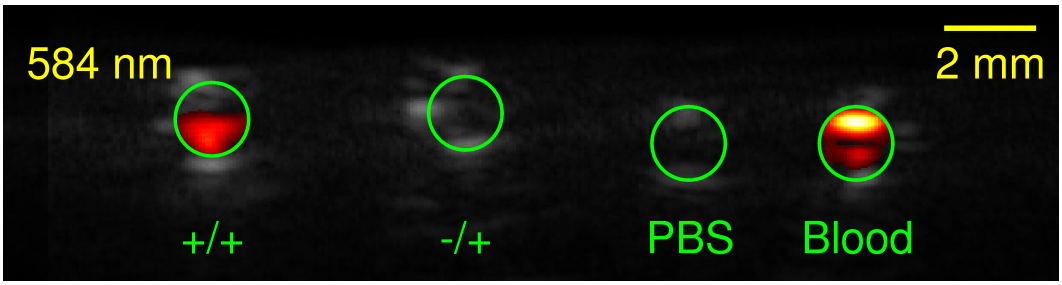

(a)

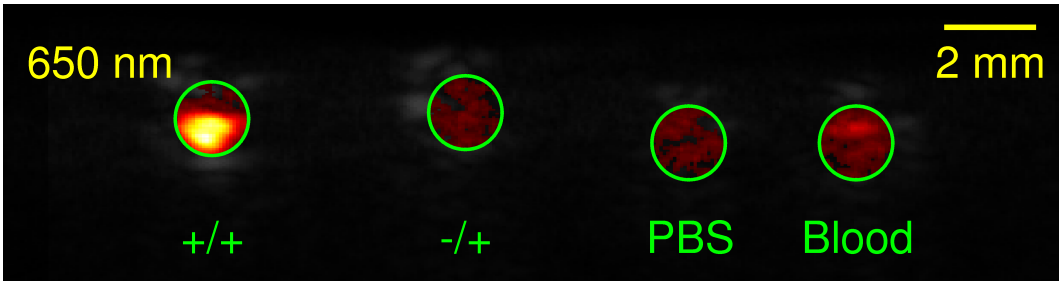

(b)

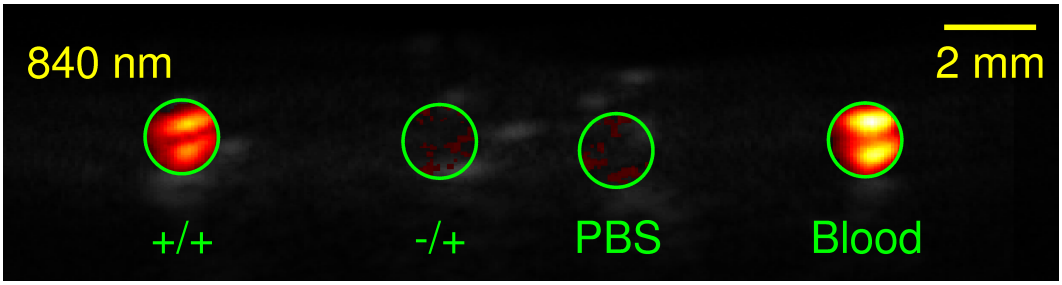

(c)

Figure 11.2: Composite ultrasound/photoacoustic images of tubes at multiple wavelengths suspended in intralipid. Tubes are labeled as blood or PBS controls, or by their Dox/TYR status respectively.

each tube, and the photoacoustic imaging regions were identified based on the known separation between images to form the composite. Quantitative data were taken as the mean of maxima over 50 frames with error bars as the standard deviation. The quantitative analysis in the tubes was followed up with chicken breast experiments at interesting wavelengths, as in figure 11.4. In this case, no compositing was necessary, due to the scattering of the tissue and relative centering of the tubes.

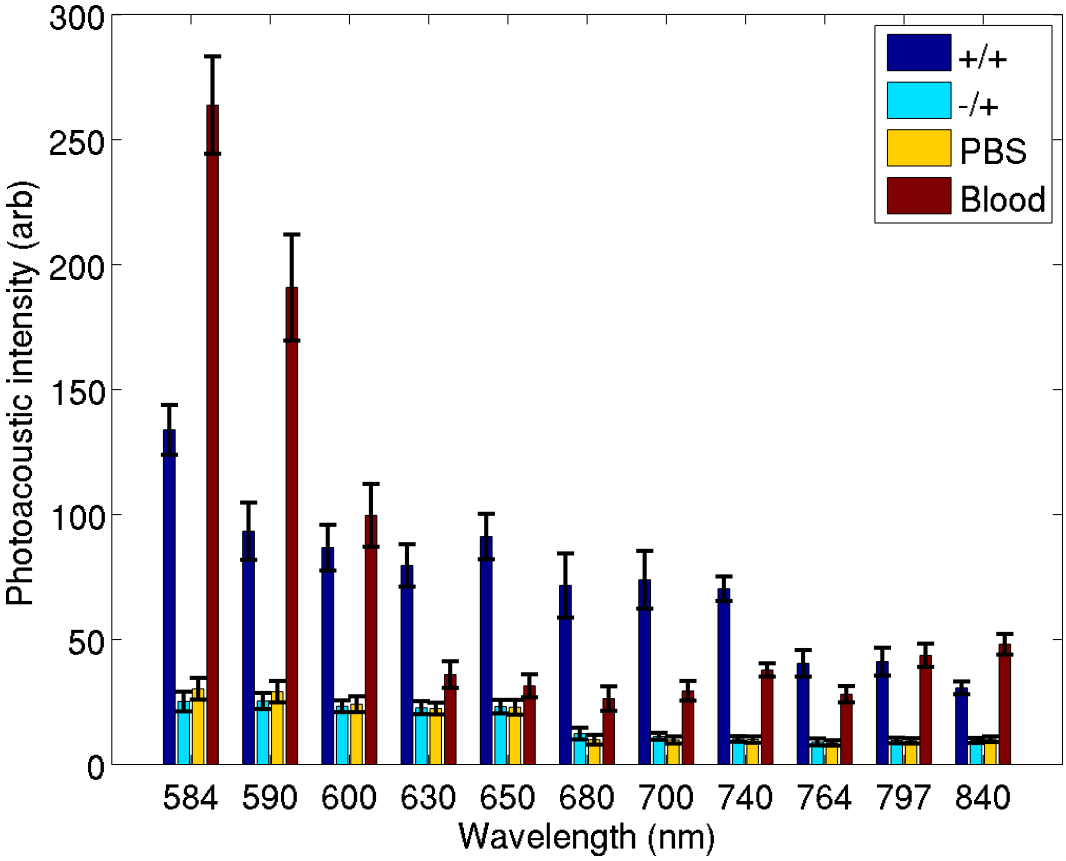

Figure 11.3: Quantitative measures (based on maximum received signal) of Dox/TYR tubes with rabbit blood and PBS controls.

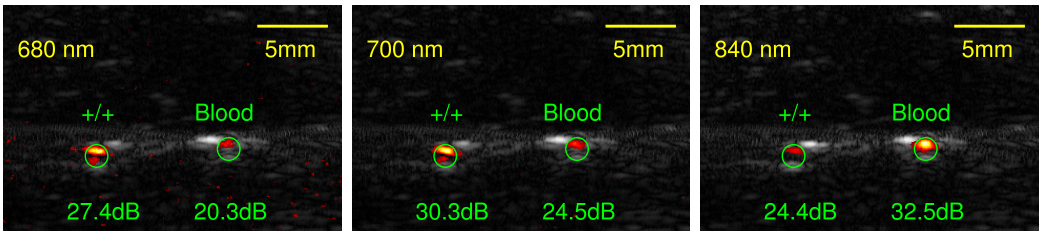

(a) (b) (c)

Figure 11.4: Combined ultrasound/photoacoustic images of +TYR/+Dox tubes in chicken breast with rabbit blood control at a depth of 2.8cm at wavelengths of (a)680, (b)700, and (c)840nm. Signal to noise ratio (SNR) numbers are given as the intensity in the area of interest divided by the standard deviation of an image noise area, presented in decibels.

11.3.3 Mouse experiments

From the previous studies, 680nm and 700nm seemed the most promising prospective wavelengths for *in vivo* imaging. We imaged mice as described above in 0.5mm slices to form a full 3-D image set. Maximum amplitude projections through all slices for 3 mice are shown in Figure 11.5. In all cases, save mouse C, the mouse was repositioned between acquisitions. The ellipses corresponding to tumor locations were positioned based on the location of the maximum amplitude of each image, with the diameter informed by the excised tumor size. The signal-to-noise ratios (SNR) presented in that figure correspond to the maximum SNR measure at each image slice (i.e. B-scan image rather than maximum amplitude projection). It is quite encouraging to note, from Figure 11.6, that the tumors need not be dark to the human eye to detect photoacoustically, and that even highly-vascularized tumors can be differentiated from tyrosinase-expressing tumors by simple thresholding, as was the case in mouse B. It should be noted that there was a significant size difference in the different cell lines with the +TYR tumors tending to be much smaller. There are a number of potential reasons for this, likely stemming from the selection process used to produce the stably transfected cell line, but in general, both tumors took several months to reach a size suitable for imaging.

11.4 Discussion

Quantitative results in Figure 11.3 follow the expected trends, with a roughly exponential decay of the signal from the +TYR cells. The -TYR cell line provided a signal level comparable to the negative control (PBS). To provide the best imaging of +TYR cells, a signal level above that of blood is desirable, provided at a wavelength of 650-700nm. Signal levels for these wavelengths measured the +TYR cells at 2.5-2.7 times that of blood for these wavelengths.

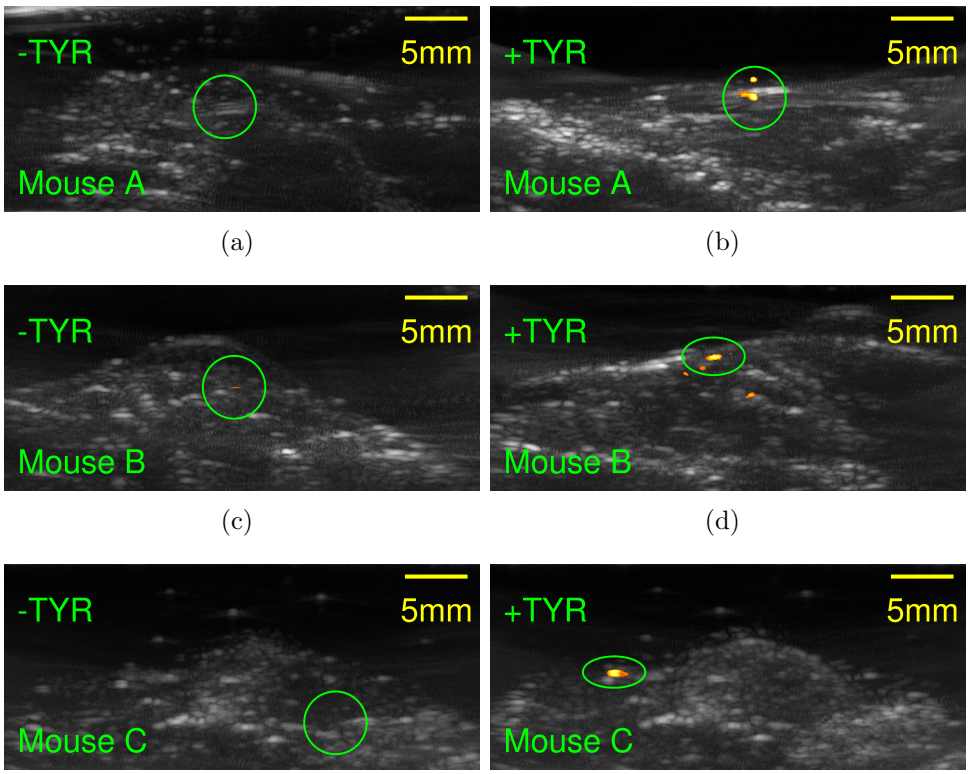

(a) (b) (c) (d) (e) (f)

Figure 11.5: +TYR and -TYR tumors in 3 mice. SNR: (a) A/-TYR 31.2dB; (b) A/+TYR 43.6dB; (c) B/-TYR 32.4dB; (d) B/+TYR 41.9dB; (e) C/-TYR 28.8dB; (f) C/+TYR 44.0dB. Mouse A/B were imaged at 700nm, mouse C at 680nm.

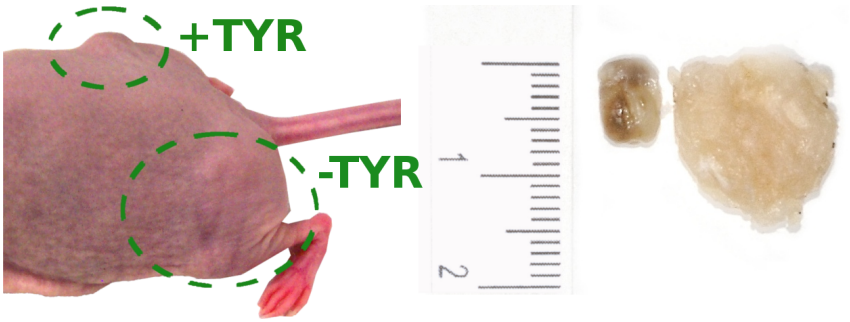

(a)

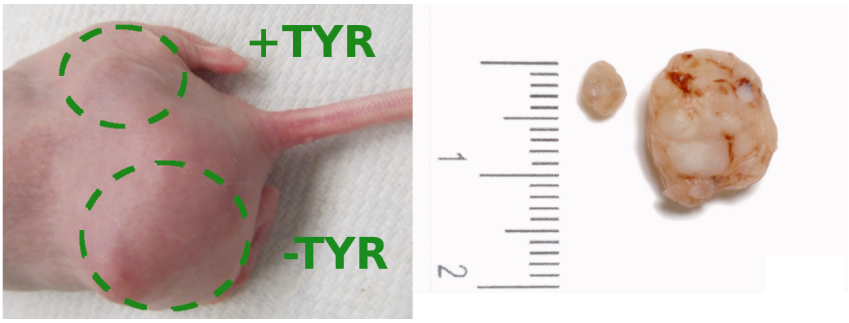

(b)

Figure 11.6: Images of (a) mouse A and (b) mouse B with their accompanying excised tumors (scale in cm).

While the results of OR-PAM imaging of tyrosinase expressing cells suggest that signal levels should be much higher compared to those in figure 11.3 [4], this is likely due to higher melanin concentration, differences in the cell line, and potentially even effective hemoglobin concentration.

Based on the results from this imaging study, calculation of the focal volume at 3.2×10^{-4}cm^3 yields 12000 cells/voxel required to detect melanin-expression, given 10^8 cells/mL in the tube samples with a contrast ratio of 1 relative to blood. Assuming tightly-packed 10μm cells (packing factor of 0.74), this requires roughly a 2.6% transfection rate to detect cells at the same signal level as blood.

Results in Figure 11.4 support the results from the intralipid experiments, though imaging at 680nm provided a contrast compared to blood of only 1.97 times. This may be due to uneven settling of cells in the tubes, or simply

a poorly centered illumination source. Regardless, this is still sufficient for simple thresholding, or multispectral techniques to pick out low concentrations of TYR-expressing cells. About 10000 cells (2.2% transfection) are required to give a contrast ratio of 1 with blood in this figure. However, if only detection is required, in 2.8cm of chicken breast tissue, only about 1000 cells/voxel are required for detection above the noise floor (or only 0.2% transfection).

The most encouraging result of this series of experiments stems from the xenograft tumors, which not only exhibited Dox-induced melanin expression, but did so at levels detectable photoacoustically. In terms of raw signal level, the +TYR tumors provided 4.9, 1.9, and 2.1 times (for mouse A, B, and C respectively) the signal level of the -TYR tumor, easily exceeding the 50% threshold set in this experiment, save for a small portion of the highly-vascular tumor in mouse B. Interestingly, upon dissection of the tumors, it was found that generally only the outer edges of visible dark spots within the tumors were dark, suggesting that the tumors may not have effectively absorbed the doxycycline, or were prevented from expressing melanin in some other way.

11.5 Conclusions

Combining ultrasound and photoacoustic imaging for the application of gene expression imaging will provide a valuable tool for both clinical and preclinical applications. Imaging sensitivity can be enhanced through averaging techniques, and specificity can be improved through multi-wavelength approaches (though such techniques can be difficult to do correctly). The transfection rates we calculate are required for detection - a maximum of 2.6% - are well within the realm of *in vivo* transfection rates, pointing to the application of this imaging technique for assessing gene expression *in vivo* at clinically relevant depths. We have shown photoacoustic imaging of gene expression using

a tyrosinase reporter both *in vivo* superficially, and at a depth of 2.8cm in chicken breast.

References

[1] Li Li et al. "Photoacoustic imaging of lacZ gene expression in vivo". In: *Journal of Biomedical Optics* 12.April (2007), p. 020504. DOI: 10.1117/1.2717531.

[2] D. Razansky et al. "Multispectral opto-acoustic tomography of deep-seated fluorescent proteins in vivo". In: *Nature Photonics* 3 (7 2009), pp. 412–417.

[3] Robert J Paproski et al. "Tyrosinase as a dual reporter gene for both photoacoustic and magnetic resonance imaging." In: *Biomedical optics express* 2.4 (Jan. 2011), pp. 771–80. ISSN: 2156-7085. DOI: 10.1364/BOE.2.000771.

[4] Arie Krumholz et al. "Photoacoustic microscopy of tyrosinase reporter gene in vivo". In: *Journal of Biomedical Optics* 16.8 (2011), p. 080503. ISSN: 10833668. DOI: 10.1117/1.3606568.

[5] Christine Nicole S. Santos and Gregory Stephanopoulos. "Melanin-Based High-Throughput Screen for l-Tyrosine Production in Escherichia coli". In: *Applied and Environmental Microbiology* 74.4 (2008), pp. 1190–1197. DOI: 10.1128/AEM.02448-07.

[6] Tyler Harrison and Roger J Zemp. "The applicability of ultrasound dynamic receive beamformers to photoacoustic imaging." In: *IEEE transactions on ultrasonics, ferroelectrics, and frequency control* 58.10 (Oct. 2011), pp. 2259–63. ISSN: 1525-8955. DOI: 10.1109/TUFFC.2011.2076.

Chapter 12

General Discussion and Conclusions

12.1 Motivation

Ultimately, the thrust of this thesis work has been developing combined ultrasound-photoacoustic systems for clinical use. The combination of the two modes is an important step towards the practical use of photoacoustic imaging, as ultrasound can act as a complementary modality and as validation. For instance, blood vessels may be identified in some cases by negative ultrasound contrast and positive contrast in photoacoustics, or they may be visualized based on Doppler ultrasound techniques. Another motivation for the inclusion of ultrasound with photoacoustic imaging is that with the appropriate system setup, interlacing ultrasound is straightforward. A final advantage that has not seen much exploration is the use of ultrasound motion tracking to correct photoacoustic images. Tissue motion between laser shots may create a lot of blur in images averaged over several frames. Tracking this motion with ultrasound and applying a correction allows the photoacoustic reconstruction to take advantage of the greater SNR provided by averaging without the introduction of

artifacts.

All of this aside, there are three major reasons why clinical use of photoacoustic imaging has not yet become widespread: system development is ongoing, boosting image quality is challenging, and there are few papers motivating clinical applications, all of which have been explored in this thesis.

12.2 System development

Photoacoustic systems are slowly becoming available commercially, but there are a few drawbacks to any commercial system, particularly for the research community. Commercial systems tend to be expensive, are often limited in their capabilities, and may be encumbered by intellectual property concerns.

Our first effort at system design was a single-element system based on a confocal dark-field design, described in chapter 3, which was the first high-frequency system of this type. This style of system is inexpensive to set up, and suitable for a variety of experiments. However, mechanical scanning can lead to motion artifacts, and single-element transducers require many laser shots to create a single image.

We also explored the idea of multimode imaging with an array system, showing a realtime system for combined photoacoustic, ultrasound, and Doppler ultrasound in chapter 4. This was the first array system to combine all three modes required for functional imaging in realtime.

Concurrent to the prior work, other members of my lab worked to develop OR-PAM endoscopy systems. There are two difficulties with photoacoustic endoscopy: the need for a compact detector, and guidance of the endoscope through the imaging subject. We came up with the idea to detect photoacoustic signals remotely with the array transducer, which is described in full detail in chapter 5. Thanks to the flexibility of the acquisition system, we

demonstrated the first combined ultrasound and photoacoustic endoscopy system which used the array for collection of OR-PAM data. This could be an invaluable tool for inspecting atherosclerotic plaques and colon and throat cancers.

12.3 Image quality improvement

The use of current clinical ultrasound systems for photoacoustic imaging requires some modification to the reconstruction that is used. We explored the idea of using ultrasound array systems with few modifications, as outlined in Chapter 6. In general, array systems - while more expensive than scanning systems - offer considerable imaging speed advantages. However, many commercially available systems offer little access to raw data, making adaptation for photoacoustic imaging difficult. The intent behind this work was to demonstrate a novel way of modifying an ultrasound system to take advantage of existing beamforming hardware through a simple adjustment of the speed of sound.

In photoacoustic imaging, especially in tomographic setups, light is often distributed by the use of a light guide. In our case, we use a ten-legged fibre bundle. To form a high-SNR photoacoustic image, one might average over a few images using all the sources. However, if you want to recover quantitative optical information, that is not sufficient due to the dependence of initial pressure on multiple optical parameters. This has been shown experimentally using an iterative approach to reconstruction [1]. Thus, the problem is to provide several images that will allow unique reconstruction of the optical parameters. This may be done using multiple wavelengths [2], but may also be done using multiple sources. We have come up with a few techniques based on this idea, and see excellent performance in tomographic simulations. Chapter

7 shows how an extension of the iterative approach improves in convergence by using multiple sources.

One interesting ultrasound technique is synthetic transmit aperture imaging. Synthetic aperture imaging typically uses one source at a time as a source of spherical waves, creates many low-resolution images with multiple sources, and adds them to create a single, high resolution image. While image quality is nearly ideal, there are SNR disadvantages since less transmit power is being used. SNR may be boosted by using temporal [3] or spatial encoding [4], or using virtual sources by transmitting focused beams [5]. In Chapter 8, we introduced S-sequence codes to the realm of spatial encoding, which provide similar performance to Hadamard codes, but without the need for ultrasound pulse inversion.

We see the same sort of SNR issues present in ultrasound synthetic aperture imaging in our multiple illumination photoacoustic tomography system. The large lasers typically used for clinical imaging will not allow temporal encoding, and it may be possible to create a virtual source using lasers, but this is very difficult in a scattering medium. Spatial encoding is actually quite easy to do by selectively blocking sources. Thanks to the need for only one source polarity, we can extend the S-sequences that we introduced for synthetic aperture imaging to our MIPAT technique. Chapter 9 shows how this novel encoded patterned illumination technique results in better resilience to low-SNR conditions.

12.4 Novel Applications

Finally, the last ongoing theme of my work has been the investigation of novel applications for photoacoustic imaging. The objective is to demonstrate the value of photoacoustic methods to scientists in the medical field for both pre-

clinical and clinical work. To that end, I have performed imaging for several projects: brachytherapy seed imaging, tyrosinase reporter gene imaging, and thyroid imaging.

Brachytherapy imaging is explained fully in chapter 10. The general idea is that metallic seeds containing a radioisotope may be implanted near a tumor area to provide constant, low-dose radiation. Since these seeds are metallic, they actually exhibit a strong photoacoustic signal. This is a somewhat surprising result, since relatively little light should be absorbed, but the same effect has been used for guiding a biopsy needle [6]. This work was the first to image these seeds in comparison to blood at several wavelengths under several centimeters of chicken breast tissue. The most important result from this study was that a longer wavelength is better for imaging metallic objects since the optical absorption of endogenous contrast tends to drop off, allowing for both better penetration, and easy identification of brachytherapy seeds. Further work in this area has been undertaken by other groups [7, 8, 9].

Reporter genes are valuable tools for preclinical and animal studies, and play an important role in studying metabolic pathways, drug delivery, and even novel cancer treatments. We developed and characterized an entirely new reporter gene based on tyrosinase in Chapter 11. Photoacoustic reporter genes, such as our tyrosinase-based system, are attractive because they can be detected and localized with ultrasonic precision deep in tissue. Traditional fluorescence-based reporter genes are often hard to detect, and sometimes lost in the background. More recent work has explored fluorescent proteins with low quantum yield, which means that they absorb light quite well at some peak wavelength, making them well-suited for multiwavelength photoacoustic imaging [10].

To revisit a previously mentioned work, Chapter 4 covers our preliminary work on thyroid imaging. We are among the first to identify it as a target of

interest, and the first to show combined Doppler and photoacoustic imaging results using a handheld array system. Ultrasound is currently the standard for imaging the thyroid as it is capable of detecting lesions. However, post-biopsy most of these features are determined to be benign. Photoacoustic imaging may allow the visualization, or at least measurement of vascularity in the thyroid region. This may allow malignant growths to be identified, as they often exhibit increased vascularity and tortuous capillary networks. If the growth is large enough, multiwavelength imaging may even allow the visualization of a necrotic core.

All of these applications are early in their development, but show great promise. Photoacoustic imaging is a very fast moving field, and the preliminary work detailed here is an important stepping stone towards clinical applications of photoacoustic imaging.

12.5 Conclusions

Photoacoustic imaging is quickly becoming a practical clinical technology. The work described on system development, reconstruction techniques, and clinical applications has yielded a number of publications. More importantly, the instrumentation that has been developed is ready for use in more clinically-oriented studies, which was the ultimate goal of this thesis.

Future development in photoacoustic imaging is likely to continue in all the areas covered in this thesis. System development is likely to include the further integration of CMUTs and optical detection technologies. Improved laser technology in terms of energy and repetition rate will provide better SNR and frame rates, allowing for better imaging of tissue dynamics. Faster tuning for multiwavelength imaging would be a boon for functional imaging. Different array geometries and illumination patterns are an interesting area for tomo-

graphic imaging. In fact, if multiple wavelengths are available simultaneously, illumination patterning may reduce the number of illuminations required for high quality functional imaging. Image quality will be directly impacted by detector and laser improvements, but refinement of reconstruction techniques will continue, improving accuracy and reducing the need for regularization in the case of iterative techniques. Ultrasound techniques like minimum variance or short-lag-spatial coherence are already being applied, and any advances in ultrasound imaging are likely to have photoacoustic applications as well. Clinical photoacoustic applications will be the most exciting area to watch. The promise for longitudinal preclinical studies on drug efficacy alone justifies further system development. Brachytherapy seed imaging has been rapidly advancing, and there is a great deal of funding going towards cancer applications.

References

[1] Thomas Jetzfellner et al. "Performance of iterative optoacoustic tomography with experimental data". In: *Applied Physics Letters* 95.1 (2009), p. 013703. ISSN: 00036951. DOI: 10.1063/1.3167280.

[2] Guillaume Bal and Kui Ren. "Multi-source quantitative photoacoustic tomography in a diffusive regime". In: *Inverse Probl.* 27.7 (2011), p. 075003.

[3] R.Y. Chiao, L.J. Thomas, and S.D. Silverstein. "Sparse array imaging with spatially-encoded transmits". In: *IEEE Ultrasonics Symposium.* Vol. 2. 1997, 1679–1682 vol.2. DOI: 10.1109/ULTSYM.1997.663318.

[4] R.Y. Chiao and L.J. Thomas. "Synthetic transmit aperture imaging using orthogonal Golay coded excitation". In: *IEEE Ultrasonics Symposium.* Vol. 2. 2000, pp. 1677–1680. DOI: 10.1109/ULTSYM.2000.921644.

[5] Moo-Ho Bae and Mok-Kun Jeong. "A study of synthetic-aperture imaging with virtual source elements in B-mode ultrasound imaging systems". In: *Ultrasonics, Ferroelectrics and Frequency Control, IEEE Transactions on* 47.6 (2000), pp. 1510–1519. ISSN: 0885-3010. DOI: 10.1109/58.883540.

[6] Chulhong Kim et al. "Handheld array-based photoacoustic probe for guiding needle biopsy of sentinel lymph nodes". In: *Journal of Biomedical Optics* 15.4 (2010), pages. DOI: 10.1117/1.3469829.

[7] Nathanael Kuo et al. "Real-time photoacoustic imaging of prostate brachytherapy seeds using a clinical ultrasound system". In: *Journal of Biomedical Optics* 17.6 (2012), pages. DOI: 10.1117/1.JBO.17.6.066005.

[8] Muyinatu A. Lediju Bell et al. "In vivo photoacoustic imaging of prostate brachytherapy seeds". In: vol. 8943. 2014, pages. DOI: 10.1117/12.2040817.

[9] Leo Pan et al. "Improving photoacoustic imaging contrast of brachytherapy seeds". In: vol. 8581. 2013, pages. DOI: 10.1117/12.2005787.

[10] Grigory S. Filonov et al. "Deep-Tissue Photoacoustic Tomography of a Genetically Encoded Near-Infrared Fluorescent Probe". In: *Angewandte Chemie* 124.6 (2012), pp. 1477–1480. ISSN: 1521-3757. DOI: 10.1002/ange.201107026.

Bibliography

Note that this is simply a bibliography containing all references in alphabetical order, as detailed by the formatting requirements. Each chapter has an individual bibliography containing the relevant sources for that chapter.

- Thomas J Allen et al. "Spectroscopic photoacoustic imaging of lipid-rich plaques in the human aorta in the 740 to 1400 nm wavelength range". In: *Journal of biomedical optics* 17.6 (June 2012), p. 061209. ISSN: 1560-2281. DOI: 10.1117/1.JBO.17.6.061209.
- R.R. Anderson and J.A. Parrish. "The optics of human skin". In: *Journal of Investigative Dermatology* 77.1 (1981), pp. 13–19.
- S R Arridge. "Optical tomography in medical imaging". In: *Inverse Probl.* 15.2 (1999), R41.
- J.P. Asen et al. "Implementing Capon beamforming on the GPU for real time cardiac ultrasound imaging". In: *Ultrasonics Symposium (IUS), 2012 IEEE International*. Oct. 2012, pp. 2133–2136. DOI: 10.1109/ULTSYM.2012.0532.
- Babak Mohammadzadeh Asl and Ali Mahloojifar. "Minimum variance beamforming combined with adaptive coherence weighting applied to medical ultrasound imaging." In: *IEEE transactions on ultrasonics, ferroelectrics, and frequency control* 56.9 (Sept. 2009), pp. 1923–31. ISSN: 1525-8955. DOI: 10.1109/TUFFC.2009.1268.

- Haim Azhari. "Appendix A: Typical Acoustic Properties of Tissues". In: *Basics of Biomedical Ultrasound for Engineers*. John Wiley & Sons, Inc., 2010, pp. 313–314. ISBN: 9780470561478. DOI: 10.1002/9780470561478.app1.
- Moo-Ho Bae and Mok-Kun Jeong. "A study of synthetic-aperture imaging with virtual source elements in B-mode ultrasound imaging systems". In: *Ultrasonics, Ferroelectrics and Frequency Control, IEEE Transactions on* 47.6 (2000), pp. 1510–1519. ISSN: 0885-3010. DOI: 10.1109/58.883540.
- Moo-Ho Bae et al. "Experimental study of transmit synthetic focusing combined with receive dynamic focusing in B-mode ultrasound imaging systems". In: *IEEE Ultrasonics Symposium*. Vol. 2. 1999, 1261–1264 vol.2. DOI: 10.1109/ULTSYM.1999.849226.
- G. Bal and G. Uhlmann. "Inverse diffusion theory of photoacoustics". In: *Inverse Probl.* 26.8, 085010 (Aug. 2010), p. 085010. DOI: 10.1088/0266-5611/26/8/085010.
- Guillaume Bal and Kui Ren. "Multi-source quantitative photoacoustic tomography in a diffusive regime". In: *Inverse Probl.* 27.7 (2011), p. 075003.
- Guillaume Bal and Kui Ren. "On multi-spectral quantitative photoacoustic tomography in diffusive regime". In: *Inverse Probl.* 28.2 (2012), p. 025010.
- Biswanath Banerjee et al. "Quantitative photoacoustic tomography from boundary pressure measurements: noniterative recovery of optical absorption coefficient from the reconstructed absorbed energy map". In: *J. Opt. Soc. Am. A* 25.9 (Sept. 2008), pp. 2347–2356. DOI: 10.1364/JOSAA.25.002347.

- J. Bercoff, M. Tanter, and Mathias Fink. "Supersonic shear imaging: a new technique for soft tissue elasticity mapping". In: *IEEE Transactions on Ultrasonics, Ferroelectrics and Frequency Control* 51.4 (Apr. 2004), pp. 396–409. ISSN: 0885-3010. DOI: 10.1109/TUFFC.2004.1295425.
- Rachel Bitton et al. "Design of a High Frequency Array Based Photoacoustic Microscopy System for Micro-Vascular Imaging in vivo". In: *Proceedings of IEEE EMBS*. Lyon, 2007, pp. 2175–2178.
- Rachel Bitton et al. "A 3-D high-frequency array based 16 channel photoacoustic microscopy system for in vivo micro-vascular imaging". In: *IEEE Trans. Med. Imag.* 28.8 (Aug. 2009), pp. 1190–7. ISSN: 1558-0062. DOI: 10.1109/TMI.2008.2011899.
- Andreas Buehler et al. "Video rate optoacoustic tomography of mouse kidney perfusion". In: *Optics Letters* 35.14 (July 2010), p. 2475. ISSN: 0146-9592. DOI: 10.1364/OL.35.002475.
- Peter Caravan. "Strategies for increasing the sensitivity of gadolinium based MRI contrast agents." In: *Chemical Society reviews* 35.6 (June 2006), pp. 512–23. ISSN: 0306-0012. DOI: 10.1039/b510982p.
- B Chance et al. "Phase measurement of light absorption and scatter in human tissue". In: *Review of Scientific Instruments* 69.10 (1998), pp. 3457–3481.
- WF Cheong, SA Prahl, and AJ Welch. "A review of the optical properties of biological tissues". In: *IEEE Journal of Quantum Electronics* 26.12 (1990), pp. 2166–2185.
- R.Y. Chiao and L.J. Thomas. "Synthetic transmit aperture imaging using orthogonal Golay coded excitation". In: *IEEE Ultrasonics Symposium*. Vol. 2. 2000, pp. 1677–1680. DOI: 10.1109/ULTSYM.2000.921644.

- R.Y. Chiao, L.J. Thomas, and S.D. Silverstein. "Sparse array imaging with spatially-encoded transmits". In: *IEEE Ultrasonics Symposium*. Vol. 2. 1997, 1679–1682 vol.2. DOI: 10.1109/ULTSYM.1997.663318.
- B. T. Cox, S. R. Arridge, and P. C. Beard. "Estimating chromophore distributions from multiwavelength photoacoustic images". In: *J. Opt. Soc. Am. A* 26.2 (Feb. 2009), pp. 443–455. DOI: 10.1364/JOSAA.26.000443.
- B. Cox, T. Tarvainen, and S. Arridge. "Multiple Illumination Quantitative Photoacoustic Tomography using Transport and Diffusion Models". In: *Tomography and Inverse Transport Theory*. Ed. by G. Bal et al. Providence, RI, USA: American Mathematical Society, 2012, pp. 1–12.
- Benjamin T. Cox et al. "Two-dimensional quantitative photoacoustic image reconstruction of absorption distributions in scattering media by use of a simple iterative method". In: *Appl. Opt.* 45.8 (Mar. 2006), pp. 1866–1875. DOI: 10.1364/AO.45.001866.
- Ben Cox et al. "Quantitative spectroscopic photoacoustic imaging: a review." In: *Journal of biomedical optics* 17.6 (June 2012), p. 061202. ISSN: 1560-2281. DOI: 10.1117/1.JBO.17.6.061202.
- Jeremy J. Dahl et al. "Lesion Detectability in Diagnostic Ultrasound with Short-Lag Spatial Coherence Imaging". In: *Ultrasonic Imaging* 33.2 (2011), pp. 119–133. DOI: 10.1177/016173461103300203.
- JB Dawson et al. "A theoretical and experimental study of light absorption and scattering by in vivo skin". In: *Phys. Med. Biol.* 25.4 (1980), pp. 695–709.
- A Devaney. "A filtered backpropagation algorithm for diffraction tomography". In: *Ultrasonic Imaging* 4.4 (Oct. 1982), pp. 336–350. ISSN: 01617346. DOI: 10.1016/0161-7346(82)90017-7.

- Todd N Erpelding et al. "Sentinel lymph nodes in the rat: noninvasive photoacoustic and US imaging with a clinical US system." In: *Radiology* 256.1 (July 2010), pp. 102–10. ISSN: 1527-1315. DOI: 10.1148/radiol.10091772.
- Grigory S. Filonov et al. "Deep-Tissue Photoacoustic Tomography of a Genetically Encoded Near-Infrared Fluorescent Probe". In: *Angewandte Chemie* 124.6 (2012), pp. 1477–1480. ISSN: 1521-3757. DOI: 10.1002/ange.201107026.
- A.E. Forbrich et al. "Realtime flash-difference ultrasound imaging of phase-change perfluorocarbon nanodroplet activation". In: *Ultrasonics Symposium (IUS), 2012 IEEE International*. Oct. 2012, pp. 687–690. DOI: 10.1109/ULTSYM.2012.0171.
- F.S. Foster et al. "A new ultrasound instrument for in vivo microimaging of mice". In: *Ultrasound in Medicine and Biology* 28.9 (2002), pp. 1165–1172. ISSN: 0301-5629. DOI: 10.1016/S0301-5629(02)00567-7.
- S R Freeman et al. "Delta-sigma oversampled ultrasound beamformer with dynamic delays." In: *IEEE Trans. Ultrason., Ferroelectr., Freq. Control* 46.2 (Jan. 1999), pp. 320–32. ISSN: 0885-3010. DOI: 10.1109/58.753020.
- S.R. Freeman et al. "An ultrasound beamformer using oversampling". In: *IEEE Ultrasonics Symposium Proceedings*. IEEE, 1997, pp. 1687–1690. ISBN: 0-7803-4153-8. DOI: 10.1109/ULTSYM.1997.663335.
- Matthew P Fronheiser et al. "Real-time optoacoustic monitoring and three- dimensional mapping of a human arm vasculature". In: *J. Biomed. Opt.* 15.April (2010), pp. 1–7. DOI: 10.1117/1.3370336.

- Donald B Fuller et al. "CT-ultrasound fusion prostate brachytherapy: A dynamic dosimetry feedback and improvement method. A report of 54 consecutive cases". In: *Brachytherapy* 4.3 (2005), pp. 207–216. ISSN: 1538-4721. DOI: 10.1016/j.brachy.2005.07.005.

- John Gamelin et al. "A real-time photoacoustic tomography system for small animals". In: *Opt. Express* 17.13 (2009), pp. 10489–10498.

- H. Gao, S. Osher, and H. Zhao. "Quantitative photoacoustic tomography". In: *Mathematical Modeling in Biomedical Imaging II: Optical, Ultrasound, and Opto-Acoustic Tomographiess*. Ed. by H. Ammari. Vol. 2035. Lecture Notes in Mathematics: Mathematical Biosciences Subseries. Berlin: Springer-Verlag, 2011, pp. 131–158.

- F. Gran and J.A. Jensen. "Multi element synthetic aperture transmission using a frequency division approach". In: *IEEE Ultrasonics Symposium*. Vol. 2. 2003, pp. 1942–1946. DOI: 10.1109/ULTSYM.2003.1293297.

- Fredrik Gran and Jorgen A. Jensen. "Spatio-temporal encoding using narrow-band linear frequency modulated signals in synthetic aperture ultrasound imaging". In: *Proc. SPIE* 5750 (2005), pp. 405–416. DOI: 10.1117/12.592352.

- Zijian Guo et al. "Compressed sensing in photoacoustic tomography in vivo". In: *J. Biomed. Opt.* 15.2 (2010), pages. DOI: 10.1117/1.3381187.

- C Haisch et al. "OPUS - Optoacoustic imaging combined with conventional ultrasound for breast cancer detection". In: *Proc. of SPIE-OSA Biomed. Opt.* 6631 (2007), pages. DOI: 10.1117/12.727971.

- P. Hajireza, W. Shi, and R. J. Zemp. "Label-free in vivo fiber-based optical-resolution photoacoustic microscopy". In: *Opt. Lett.* 36.20 (Oct. 2011), pp. 4107–4109. DOI: 10.1364/OL.36.004107.

- Parsin Hajireza, Wei Shi, and Roger J Zemp. "Real-time handheld optical-resolution photoacoustic microscopy". In: *Optics Express* 19.21 (Sept. 2011), p. 20097. ISSN: 1094-4087. DOI: 10.1364/OE.19.020097.
- Parsin Hajireza et al. "Optical resolution photoacoustic microendoscopy with ultrasound-guided insertion and array system detection". In: *Journal of Biomedical Optics* 18.9 (2013), pp. 090502–090502. DOI: 10.1117/1.JBO.18.9.090502.
- Ben H. Han et al. "Prostate brachytherapy seed identification on post-implant TRUS images". In: *Medical Physics* 30.5 (2003), p. 898. ISSN: 00942405. DOI: 10.1118/1.1568976.
- Tyler Harrison, Robert J. Paproski, and Roger J. Zemp. "In vivo imaging of inducible tyrosinase gene expression with an ultrasound array-based photoacoustic system". In: vol. 8223. 2012, pages. DOI: 10.1117/12.908987.
- Tyler Harrison, Alexander Sampaleanu, and Roger J. Zemp. "S-Sequence Spatially-Encoded Synthetic Aperture Ultrasound Imaging". In: 61.5 (2014), pp. 886–890. DOI: 10.1109/TUFFC.2014.2979.
- Tyler Harrison, Peng Shao, and Roger Zemp. "S-sequence patterned illumination for fixed-point iterative multiple illumination photoacoustic tomography". In: vol. 8943. 2014, pages. DOI: 10.1117/12.2040580.
- Tyler Harrison, Peng Shao, and Roger J. Zemp. "A least-squares fixed-point iterative algorithm for multiple illumination photoacoustic tomography". In: *Biomed. Opt. Express* 4.10 (Oct. 2013), pp. 2224–2230. DOI: 10.1364/BOE.4.002224.
- Tyler Harrison, Peng Shao, and Roger J. Zemp. "S-sequence spatial coding for iterative multiple illumination photoacoustic tomography".

Manuscript submitted for publication (Journal of Biomedical Optics, 140294P). 2014.

- Tyler Harrison and Roger J Zemp. "Coregistered photoacoustic-ultrasound imaging applied to brachytherapy." In: *Journal of biomedical optics* 16.8 (Aug. 2011), p. 080502. ISSN: 1560-2281. DOI: 10.1117/1.3606566.
- Tyler Harrison and Roger J. Zemp. "Interlaced realtime channel-domain photoacoustic and ultrasound imaging". In: *Proceedings of SPIE*. Vol. 7899. 2011, pages. DOI: 10.1117/12.875507.
- Tyler Harrison and Roger J. Zemp. "Photoacoustic imaging of brachytherapy seeds using a channel-domain ultrasound array system". In: *Proc. SPIE*. Vol. 7899. 2011, pages. DOI: 10.1117/12.875550.
- Tyler Harrison and Roger J Zemp. "The applicability of ultrasound dynamic receive beamformers to photoacoustic imaging." In: *IEEE transactions on ultrasonics, ferroelectrics, and frequency control* 58.10 (Oct. 2011), pp. 2259–63. ISSN: 1525-8955. DOI: 10.1109/TUFFC.2011.2076.
- Tyler Harrison et al. "Combined photoacoustic and ultrasound biomicroscopy". In: *Optics Express* 17.24 (2009), pp. 22041–22046. DOI: 10.1063/1.2195024.2..
- Tyler Harrison et al. "Optical-resolution photoacoustic micro-endoscopy with ultrasound array system detection". In: vol. 8581. 2013, pages. DOI: 10.1117/12.2004887.
- Tyler Harrison et al. "Real-time clinically oriented array-based in vivo combined photoacoustic and power Doppler imaging". In: vol. 8943. 2014, pages. DOI: 10.1117/12.2040609.
- I K Holfort, F Gran, and J A Jensen. "Plane wave medical ultrasound imaging using adaptive beamforming". In: *Sensor Array and Multichan-*

nel Signal Processing Workshop, 2008. SAM 2008. 5th IEEE. July 2008, pp. 288–292. DOI: 10.1109/SAM.2008.4606874.

- I K Holfort, F Gran, and J A Jensen. "Plane wave medical ultrasound imaging using adaptive beamforming". In: *Sensor Array and Multichannel Signal Processing Workshop, 2008. SAM 2008. 5th IEEE*. July 2008, pp. 288–292. DOI: 10.1109/SAM.2008.4606874.
- IK Holfort, Fredrik Gran, and JA Jensen. "Broadband minimum variance beamforming for ultrasound imaging". In: *IEEE Transactions on Ultrasonics, Ferroelectrics and Frequency Control* 56.2 (2009), pp. 314–325.
- Song Hu et al. "Functional transcranial brain imaging by optical-resolution photoacoustic microscopy". In: *Journal of Biomedical Optics* 14.4 (2009), pages. DOI: 10.1117/1.3194136.
- K. Ishii et al. "Determination of optical property changes during laser therapies". In: *Lasers Electro Optics The Pacific Rim Conference on Lasers and Electro-Optics, 2009. CLEO/PACIFIC RIM '09. Conference on*. Aug. 2009, pp. 1–2. DOI: 10.1109/CLEOPR.2009.5292314.
- J.A. Jensen and S.I. Nikolov. "Fast simulation of ultrasound images". In: *IEEE Ultrasonics Symposium*. Vol. 2. 2000, 1721–1724 vol.2. DOI: 10.1109/ULTSYM.2000.921654.
- Thomas Jetzfellner et al. "Performance of iterative optoacoustic tomography with experimental data". In: *Applied Physics Letters* 95.1 (2009), p. 013703. ISSN: 00036951. DOI: 10.1063/1.3167280.
- Yan Jiang et al. "Combined photoacoustic and high-frequency power Doppler ultrasound imaging". In: *Photons Plus Ultrasound: Imaging and Sensing 2010*. Ed. by Alexander A Oraevsky and Lihong V Wang. Vol. 7564. 1. SPIE, 2010, p. 756404. DOI: 10.1117/12.841044.

- Yan Jiang et al. "Photoacoustic and high-frequency power Doppler ultrasound biomicroscopy: a comparative study". In: *J. Biomed. Opt.* 15.5 (2010), p. 056008. ISSN: 10833668. DOI: 10.1117/1.3491126.
- Yan Jiang et al. "Blood oxygen flux estimation with a combined photoacoustic and high-frequency ultrasound microscopy system: a phantom study." In: *Journal of biomedical optics* 17.3 (Mar. 2012), p. 036012. ISSN: 1560-2281. DOI: 10.1117/1.JBO.17.3.036012.
- Chulhong Kim et al. "Deeply penetrating in vivo photoacoustic imaging using a clinical ultrasound array system". In: *Biomedical Optics Express* 1.1 (July 2010), pp. 278–284. ISSN: 2156-7085. DOI: 10.1364/BOE.1.000278.
- Chulhong Kim et al. "Handheld array-based photoacoustic probe for guiding needle biopsy of sentinel lymph nodes". In: *Journal of Biomedical Optics* 15.4 (2010), pages. DOI: 10.1117/1.3469829.
- Myung K Kim. "Principles and techniques of digital holographic microscopy". In: *SPIE Reviews* 1.1 (2010), p. 018005. ISSN: 19463251. DOI: 10.1117/6.0000006.
- Roy G M Kolkman et al. "Real-time in vivo photoacoustic and ultrasound imaging." In: *J. Biomed. Opt.* 13.5 (2008), p. 050510. ISSN: 1083-3668. DOI: 10.1117/1.3005421.
- K P Köstli et al. "Temporal backward projection of optoacoustic pressure transients using fourier transform methods". In: *Phys. Med. Biol.* 46.7 (July 2001), pp. 1863–72. ISSN: 0031-9155.
- Komel P Köstli and Paul C Beard. "Two-dimensional photoacoustic imaging by use of Fourier-transform image reconstruction and a detector with an anisotropic response." In: *Appl. Optics* 42.10 (Apr. 2003), pp. 1899–908. ISSN: 0003-6935.

- Murali C. Krishna et al. "Electron Paramagnetic Resonance for Small Animal Imaging Applications". In: *ILAR Journal* 42.3 (2001), pp. 209–218. DOI: 10.1093/ilar.42.3.209.
- Robert A. Kruger et al. "Photoacoustic ultrasound (PAUS)-Reconstruction tomography". In: *Medical Physics* 22.10 (1995), pp. 1605–1609. DOI: 10.1118/1.597429.
- Arie Krumholz et al. "Photoacoustic microscopy of tyrosinase reporter gene in vivo". In: *Journal of Biomedical Optics* 16.8 (2011), p. 080503. ISSN: 10833668. DOI: 10.1117/1.3606568.
- Arie Krumholz et al. "Photoacoustic imaging of the near-infrared fluorescent protein iRFP in vivo". In: vol. 8223. 2012, pages. DOI: 10.1117/12.908927.
- Nathanael Kuo et al. "Photoacoustic imaging of prostate brachytherapy seeds in ex vivo prostate". In: *Proceedings of SPIE*. Vol. 7964. May. 2011, pages. DOI: 10.1117/12.878041.
- Nathanael Kuo et al. "Real-time photoacoustic imaging of prostate brachytherapy seeds using a clinical ultrasound system". In: *Journal of Biomedical Optics* 17.6 (2012), pages. DOI: 10.1117/1.JBO.17.6.066005.
- Periannan Kuppusamy et al. "In vivo electron paramagnetic resonance imaging of tumor heterogeneity and oxygenation in a murine model". In: *Cancer Research* 58.7 (1998), pp. 1562–1568.
- B Larrat et al. "MR-guided transcranial brain HIFU in small animal models." In: *Physics in medicine and biology* 55.2 (Jan. 2010), pp. 365–88. ISSN: 1361-6560. DOI: 10.1088/0031-9155/55/2/003.
- Muyinatu A. Lediju Bell, Danny Y. Song, and Emad M. Boctor. "Coherence-based photoacoustic imaging of brachytherapy seeds implanted in a canine prostate". In: vol. 9040. 2014, pages. DOI: 10.1117/12.2043901.

- Muyinatu A. Lediju Bell et al. "In vivo photoacoustic imaging of prostate brachytherapy seeds". In: vol. 8943. 2014, pages. DOI: 10.1117/12.2040817.
- Muyinatu a. Lediju et al. "Short-lag spatial coherence imaging". In: *2010 IEEE International Ultrasonics Symposium*. IEEE, Oct. 2010, pp. 987–990. ISBN: 978-1-4577-0382-9. DOI: 10.1109/ULTSYM.2010.5935711.
- Li Li et al. "Photoacoustic imaging of lacZ gene expression in vivo". In: *Journal of Biomedical Optics* 12.April (2007), p. 020504. DOI: 10.1117/1.2717531.
- Li Li et al. "Simultaneous imaging of a lacZ-marked tumor and microvasculature morphology in vivo by dual-wavelength photoacoustic microscopy". In: *Journal of Innovative Optical Health Sciences* 01.02 (2008), pp. 207–215. DOI: 10.1142/S1793545808000212.
- Meng-Lin Li et al. "Improved in vivo photoacoustic microscopy based on a virtual-detector concept". In: *Opt. Lett.* 31.4 (Feb. 2006), pp. 474–6. ISSN: 0146-9592.
- Pai-Chi Li and Meng-Lin Li. "Adaptive imaging using the generalized coherence factor". In: *IEEE Trans. Ultrason., Ferroelectr., Freq. Control* 50.2 (Feb. 2003), pp. 128–41. ISSN: 0885-3010.
- C K Liao, M L Li, and P C Li. "Optoacoustic imaging with synthetic aperture focusing and coherence weighting". In: *Opt. Lett.* 29.21 (Nov. 2004), pp. 2506–8. ISSN: 0146-9592.
- Lun-De Liao et al. "Transcranial imaging of functional cerebral hemodynamic changes in single blood vessels using in vivo photoacoustic microscopy." In: *Journal of cerebral blood flow and metabolism : official journal of the International Society of Cerebral Blood Flow and*

Metabolism 32.6 (June 2012), pp. 938–51. ISSN: 1559-7016. DOI: 10.1038/jcbfm.2012.42.

- G.R. Lockwood, J.R. Talman, and S.S. Brunke. "Real-time 3-D ultrasound imaging using sparse synthetic aperture beamforming". In: *IEEE Transactions on Ultrasonics, Ferroelectrics and Frequency Control* 45.4 (1998), pp. 980–988. ISSN: 0885-3010. DOI: 10.1109/58.710573.
- Jonathan F. Lovell et al. "Porphysome nanovesicles generated by porphyrin bilayers for use as multimodal biophotonic contrast agents". In: *Nat Mater* 10.4 (Apr. 2011), pp. 324–332. ISSN: 1476-1122. DOI: 10.1038/nmat2986.
- Huihong Lu et al. "Improved depth-of-field photoacoustic microscopy with a custom high-frequency annular array transducer". In: *Proceedings of SPIE*. Vol. 7899. 2011, pages. DOI: 10.1117/12.875601.
- Emilie Mace et al. "High sensitivity brain angiography using Ultrafast Doppler". In: *2010 IEEE International Ultrasonics Symposium*. IEEE, Oct. 2010, pp. 1194–1197. ISBN: 978-1-4577-0382-9. DOI: 10.1109/ULTSYM.2010.5935810.
- Srivalleesha Mallidi et al. "Multiwavelength Photoacoustic Imaging and Plasmon Resonance Coupling of Gold Nanoparticles for Selective Detection of Cancer". In: *Nano Letters* 9.8 (2009). PMID: 19572747, pp. 2825–2831. DOI: 10.1021/nl802929u.
- J. Mamou and E.J. Feleppa. "Ultrasonic Detection and Imaging of Brachytherapy Seeds Based on Singular Spectrum Analysis". In: *Acoustical Imaging*. Ed. by Iwaki Akiyama. Vol. 29. Acoustical Imaging. Springer Netherlands, 2009, pp. 127–132. ISBN: 978-1-4020-8822-3. DOI: 10.1007/978-1-4020-8823-0_18.

- K Maslov, G Stoica, and L.V. Wang. "In vivo dark-field reflection-mode photoacoustic microscopy". In: *Opt. Lett.* 30.6 (2005), pp. 625–627.
- Konstantin Maslov, Hao F Zhang, and Lihong V Wang. "Effects of wavelength-dependent fluence attenuation on the noninvasive photoacoustic imaging of hemoglobin oxygen saturation in subcutaneous vasculature in vivo". In: *Inverse Problems* 23.6 (2007), S113.
- Konstantin Maslov et al. "Optical-resolution photoacoustic microscopy for in vivo imaging of single capillaries". In: *Optics Letters* 33.9 (2008), pp. 929–931.
- MA Mintun et al. "Brain oxygen utilization measured with O-15 radiotracers and positron emission tomography". In: *Journal of Nuclear Medicine* 25.2 (1984), pp. 177–187.
- William H. Nau, Robert J. Roselli, and Douglas F. Milam. "Measurement of thermal effects on the optical properties of prostate tissue at wavelengths of 1,064 and 633 nm". In: *Lasers in Surgery and Medicine* 24.1 (1999), pp. 38–47. ISSN: 1096-9101. DOI: 10.1002/(SICI)1096-9101(1999)24:1<38::AID-LSM7>3.0.CO;2-G.
- J.J. Niederhauser et al. "Combined ultrasound and optoacoustic system for real-time high-contrast vascular imaging in vivo". In: *Medical Imaging, IEEE Transactions on* 24.4 (Apr. 2005), pp. 436–440. ISSN: 0278-0062. DOI: 10.1109/TMI.2004.843199.
- Joel J. Niederhauser, Michael Jaeger, and Martin Frenz. "Comparision of laser-induced and classical ultasound". In: *Proc. SPIE* 4960 (2003), pp. 118–123. ISSN: 0277786X. DOI: 10.1117/12.483509.
- Svetoslav Nikolov and Joergen A. Jensen. "Comparison between different encoding schemes for synthetic aperture imaging". In: *Proc. SPIE* 4687 (2002), pp. 1–12. DOI: 10.1117/12.462151.

- Carl-Inge Nilsen and Sverre Holm. "Wiener beamforming and the coherence factor in ultrasound imaging." In: *IEEE Trans. Ultrason., Ferroelectr., Freq. Control* 57.6 (June 2010), pp. 1329–46. ISSN: 1525-8955. DOI: 10.1109/TUFFC.2010.1553.

- C.F Njeh et al. "Assessment of bone status using speed of sound at multiple anatomical sites". In: *Ultrasound in Medicine & Biology* 27.10 (Oct. 2001), pp. 1337–1345. ISSN: 03015629. DOI: 10.1016/S0301-5629(01)00437-9.

- Vasilis Ntziachristos and Daniel Razansky. "Molecular imaging by means of multispectral optoacoustic tomography (MSOT)". In: *Chemical reviews* 110.5 (2010), pp. 2783–2794.

- M. O'Donnell. "Coded excitation system for improving the penetration of real-time phased-array imaging systems". In: *IEEE Transactions on Ultrasonics, Ferroelectrics and Frequency Control* 39.3 (1992), pp. 341–351. ISSN: 0885-3010. DOI: 10.1109/58.143168.

- M. O'Donnell and L.J. Thomas. "Efficient synthetic aperture imaging from a circular aperture with possible application to catheter-based imaging". In: *IEEE Transactions on Ultrasonics, Ferroelectrics and Frequency Control* 39.3 (1992), pp. 366–380. ISSN: 0885-3010. DOI: 10.1109/58.143171.

- S. Ogawa et al. "Oxygenation-Sensitive Contrast in Magnetic Resonance Image of Rodent Brain at High Magnetic Fields". In: *Magnetic Resonance in Medicine* 14.1 (2005), pp. 68–78.

- Alexander A Oraevsky, Steven L Jacques, and Frank K Tittel. "Measurement of tissue optical properties by time-resolved detection of laser-induced transient stress". In: *Appl. Optics* 36.1 (Jan. 1997), pp. 402–415. ISSN: 0003-6935. DOI: 10.1364/AO.36.000402.

- Alexander A Oraevsky, Steven L Jacques, and Frank K Tittel. "Measurement of tissue optical properties by time-resolved detection of laser-induced transient stress". In: *Appl. Opt.* 36.1 (1997), pp. 402–415.
- Leo Pan et al. "Improving photoacoustic imaging contrast of brachytherapy seeds". In: vol. 8581. 2013, pages. DOI: 10.1117/12.2005787.
- Robert J Paproski et al. "Tyrosinase as a dual reporter gene for both photoacoustic and magnetic resonance imaging." In: *Biomedical optics express* 2.4 (Jan. 2011), pp. 771–80. ISSN: 2156-7085. DOI: 10.1364/BOE.2.000771.
- S Park. "Integrated system for ultrasonic, photoacoustic and elasticity imaging". In: *Proceedings of SPIE*. Vol. 6147. SPIE, 2006, pages. DOI: 10.1117/12.661508.
- Suhyun Park, Salavat R Aglyamov, and S. Emelianov. "Beamforming for Photoacoustic Imaging Using Linear Array Transducer". In: *IEEE Ultrasonics Symposium Proceedings*. Vol. 1. IEEE, Oct. 2007, pp. 856–859. ISBN: 978-1-4244-1383-6. DOI: 10.1109/ULTSYM.2007.219.
- Suhyun Park et al. "Adaptive beamforming for photoacoustic imaging". In: *Opt. Lett.* 33.12 (June 2008), pp. 1291–3. ISSN: 0146-9592.
- Suhyun Park et al. "Adaptive beamforming for photoacoustic imaging using linear array transducer". In: *IEEE Ultrasonics Symposium Proceedings*. IEEE, Nov. 2008, pp. 1088–1091. ISBN: 978-1-4244-2428-3. DOI: 10.1109/ULTSYM.2008.0262.
- Christian Passmann and Helmut Ermert. "A 100-MHz ultrasound imaging system for dermatologic and ophthalmologic diagnostics". In: *IEEE Trans. Ultrason., Ferroelectr., Freq. Control* 43.4 (1996), pp. 545–552.

- SK Patch and A Greenleaf. "Ultrasound attenuation and thermo/photo/opto-acoustic tomography: theoretical foundation". In: *Proceedings of SPIE*. Vol. 6437. 414. 2007, p. 643726. DOI: 10.1117/12.701161.
- M J Paulus et al. "High resolution X-ray computed tomography: an emerging tool for small animal cancer research." In: *Neoplasia* 2.1-2 (2000), pp. 62–70. ISSN: 1522-8002.
- Daniel Razansky, Claudio Vinegoni, and Vasilis Ntziachristos. "Multispectral photoacoustic imaging of fluorochromes in small animals". In: *Opt. Lett.* 32.19 (Oct. 2007), pp. 2891–2893. DOI: 10.1364/OL.32.002891.
- D. Razansky et al. "Multispectral opto-acoustic tomography of deep-seated fluorescent proteins in vivo". In: *Nature Photonics* 3 (7 2009), pp. 412–417.
- K. Ren, H. Gao, and H. Zhao. "A Hybrid Reconstruction Method for Quantitative PAT". In: *SIAM J. Imaging Sci.* 6.1 (2013), pp. 32–55.
- Jorge Ripoll and Vasilis Ntziachristos. "Quantitative point source photoacoustic inversion formulas for scattering and absorbing media". In: *Phys. Rev. E* 71 (3 Mar. 2005), p. 031912. DOI: 10.1103/PhysRevE.71.031912.
- U Sabatini et al. "Quantitative assessment of cerebral blood volume by single-photon emission computed tomography". In: *Stroke* 22.3 (1991), pp. 324–330.
- Christine Nicole S. Santos and Gregory Stephanopoulos. "Melanin-Based High-Throughput Screen for l-Tyrosine Production in Escherichia coli". In: *Applied and Environmental Microbiology* 74.4 (2008), pp. 1190–1197. DOI: 10.1128/AEM.02448-07.

- Magali Sasso and Claude Cohen-Bacrie. "Medical ultrasound imaging using the fully adaptive beamformer". In: *IEEE International Conference on Acoustics, Speech, and Signal Processing*. 4. IEEE, 2005, pp. 489–492. ISBN: 0-7803-8874-7. DOI: 10.1109/ICASSP.2005.1415448.

- Peng Shao, Ben Cox, and Roger J Zemp. "Estimating optical absorption, scattering, and Grueneisen distributions with multiple-illumination photoacoustic tomography." In: *Applied optics* 50.19 (July 2011), pp. 3145–54. ISSN: 1539-4522.

- Peng Shao, Tyler Harrison, and Roger J. Zemp. "Iterative algorithm for multiple illumination photoacoustic tomography (MIPAT) using ultrasound channel data". In: *Biomed. Opt. Express* 3.12 (Dec. 2012), pp. 3240–3249. DOI: 10.1364/BOE.3.003240.

- Peng Shao et al. "Integrated micro-endoscopy system for simultaneous fluorescence and optical-resolution photoacoustic imaging". In: *Journal of Biomedical Optics* 17.7 (2012), pages. DOI: 10.1117/1.JBO.17.7.076024.

- Peng Shao et al. "Mosaic acquisition and processing for optical-resolution photoacoustic microscopy". In: *Journal of Biomedical Optics* 17.8 (2012), pages. DOI: 10.1117/1.JBO.17.8.080503.

- Wei Shi et al. "High repetition rate passively Q-switched fiber and microchip lasers for optical resolution photoacoustic imaging". In: *Photons Plus Ultrasound: Imaging and Sensing 2010*. Ed. by Alexander A Oraevsky and Lihong V Wang. Vol. 7564. 1. SPIE, 2010, p. 75640X. DOI: 10.1117/12.842533.

- Ho-Chul Shin et al. "Ultrasound in medicine & biology". In: 36.4 (Apr. 1, 2010), pp. 623–636. ISSN: 0301-5629.

- R.I. Siphanto et al. "Serial noninvasive photoacoustic imaging of neovascularization in tumor angiogenesis". In: *Opt. Express* 13.1 (Jan. 2005), pp. 89–95. DOI: 10.1364/OPEX.13.000089.
- Mathangi Sivaramakrishnan et al. "Limitations of quantitative photoacoustic measurements of blood oxygenation in small vessels". In: *Phys. Med. Biol.* 52.5 (Mar. 2007), pp. 1349–61. ISSN: 0031-9155. DOI: 10.1088/0031-9155/52/5/010.
- N. J. A. Sloane et al. "Codes for Multiplex Spectrometry". In: *Appl. Opt.* 8.10 (Oct. 1969), pp. 2103–2106. DOI: 10.1364/AO.8.002103.
- Liang Song et al. "Fast 3-D dark-field reflection-mode photoacoustic microscopy in vivo with a 30-MHz ultrasound linear array." In: *J. Biomed. Opt.* 13.5 (2008), p. 054028. ISSN: 1083-3668. DOI: 10.1117/1.2976141.
- VR Stewart and PS Sidhu. "New directions in ultrasound: microbubble contrast". In: *British Journal of Radiology* 79 (2006), pp. 188–194. DOI: 10.1259/bjr/17790547.
- Camilla Storaa et al. "Tissue motion imaging of the left ventricle-quantification of myocardial strain, velocity, acceleration and displacement in a single image". In: *European Journal of Echocardiography* 5.5 (2004), pp. 375–385. DOI: 10.1016/j.euje.2004.02.004.
- Jimmy L Su et al. "Photoacoustic imaging of prostate brachytherapy seeds." In: *Biomedical optics express* 2.8 (Aug. 2011), pp. 2243–54. ISSN: 2156-7085. DOI: 10.1364/BOE.2.002243.
- Jimmy Su et al. "Photoacoustic imaging of clinical metal needles in tissue." In: *Journal of biomedical optics* 15.2 (2010), p. 021309. ISSN: 1560-2281. DOI: 10.1117/1.3368686.

- JF Synnevag, Andreas Austeng, and S. Holm. "Minimum variance adaptive beamforming applied to medical ultrasound imaging". In: *Proceedings of IEEE Ultrasonics Symposium*. Vol. 00. 4. Rotterdam, Netherlands, 2005, pp. 1199–1202.
- K.E. Thomenius. "Evolution of ultrasound beamformers". In: *IEEE Ultrasonics Symposium Proceedings*. IEEE, 1996, pp. 1615–1622. ISBN: 0-7803-3615-1. DOI: 10.1109/ULTSYM.1996.584398.
- Bradley E Treeby and B T Cox. "k-Wave: MATLAB toolbox for the simulation and reconstruction of photoacoustic wave fields." In: *J. Biomed. Opt.* 15.2 (2010), pages. ISSN: 1560-2281. DOI: 10.1117/1.3360308.
- A.L. Ulery et al. "IEEE Standard for Safety Levels with Respect to Human Exposure to Radio Frequency Electromagnetic Fields , 3 kHz to 300 GHz". In: *slac.stanford.edu* (1999).
- S. Vaithilingam et al. "Three-dimensional photoacoustic imaging using a two-dimensional CMUT array". In: *IEEE Trans. Ultrason., Ferroelectr., Freq. Control* 56.11 (2009), p. 2411.
- Bo Wang et al. "Detection of lipid in atherosclerotic vessels using ultrasound-guided spectroscopic intravascular photoacoustic imaging". In: *Optics Express* 18.5 (Feb. 2010), p. 4889. ISSN: 1094-4087. DOI: 10.1364/OE.18.004889.
- Lidai Wang et al. "Fast voice-coil scanning optical-resolution photoacoustic microscopy". In: *Opt. Lett.* 36.2 (Jan. 2011), pp. 139–141. DOI: 10.1364/OL.36.000139.

- Lidai Wang et al. "Fast voice-coil scanning optical-resolution photoacoustic microscopy". In: *Opt. Lett.* 36.2 (Jan. 2011), pp. 139–141. DOI: 10.1364/OL.36.000139.

- Lihong V. Wang and Hsin-I Wu. *Biomedical Optics: Principles and Imaging*. Hoboken, NJ: Wiley, 2007. ISBN: 978-0-471-74304-0.
- L.V. Wang. "Prospects of photoacoustic tomography". In: *Medical Physics* 35 (12 2008), pp. 5758–5767.
- L.V. Wang. "Tutorial on Photoacoustic Microscopy and Computed Tomography". In: *IEEE J. Sel. Top. Quant.* 14.1 (2008), pp. 171–179. ISSN: 1077-260X. DOI: 10.1109/JSTQE.2007.913398.
- Xueding Wang et al. "Noninvasive laser-induced photoacoustic tomography for structural and functional in vivo imaging of the brain". eng. In: *Nature Biotechnology* 21.7 (2003), pp. 803–806. ISSN: 1087-0156.
- Xueding Wang et al. "Noninvasive imaging of hemoglobin concentration and oxygenation in the rat brain using high-resolution photoacoustic tomography." In: *J. Biomed. Opt.* 11.2 (2006), p. 024015. ISSN: 1083-3668. DOI: 10.1117/1.2192804.
- Katheryne E Wilson, Kimberly A Homan, and Stanislav Y Emelianov. "Remotely triggered contrast nanoagent for ultrasound and photoacoustic imaging". In: *2010 IEEE International Ultrasonics Symposium*. IEEE, Oct. 2010, pp. 1003–1006. ISBN: 978-1-4577-0382-9. DOI: 10.1109/ULTSYM.2010.5935757.
- Zhixing Xie et al. "Combined photoacoustic and ultrasound imaging of human breast in vivo in the mammographic geometry". In: vol. 8581. 2013, pages. DOI: 10.1117/12.2004599.
- Guan Xu et al. "Photoacoustic and ultrasound dual-modality imaging of human peripheral joints". In: *Journal of Biomedical Optics* 18.1 (2012), pp. 010502–010502. DOI: 10.1117/1.JBO.18.1.010502.
- M Xu and L.V. Wang. "Photoacoustic imaging in biomedicine". In: *Review of Scientific Instruments* 77.4041101 (2006), pp. 1–22.

- M Xu, Y. Xu, and L.V. Wang. "Time-domain reconstruction algorithms and numerical simulations for thermoacoustic tomography in various geometries". In: *IEEE Trans. Biomed. Eng.* 50.9 (2003), pp. 1086–1099.
- Minghua Xu and Lihong Wang. "Universal back-projection algorithm for photoacoustic computed tomography". In: *Physical Review* 71.016706 (Jan. 2005), pp. 1–7. ISSN: 1539-3755. DOI: 10.1103/PhysRevE.71.016706.
- Minghua Xu and Lihong V. Wang. "Analytic explanation of spatial resolution related to bandwidth and detector aperture size in thermoacoustic or photoacoustic reconstruction". In: *Phys. Rev. E* 67 (5 May 2003), p. 056605. DOI: 10.1103/PhysRevE.67.056605.
- Lu Yin et al. "Tomographic imaging of absolute optical absorption coefficient in turbid media using combined photoacoustic and diffusing light measurements". In: *Opt. Lett.* 32.17 (Sept. 2007), pp. 2556–2558. DOI: 10.1364/OL.32.002556.
- J. Ylitalo. "On the signal-to-noise ratio of a synthetic aperture ultrasound imaging method". In: *European Journal of Ultrasound* 3.3 (1996), pp. 277–281. ISSN: 0929-8266. DOI: 10.1016/0929-8266(95)00160-S.
- Chun Yuan et al. "Contrast-Enhanced High Resolution MRI for Atherosclerotic Carotid Artery Tissue Characterization". In: *Journal of Magnetic Resonance Imaging* 15 (2002), pp. 62–67. DOI: 10.1002/jmri.10030.
- Zhen Yuan and Huabei Jiang. "Quantitative photoacoustic tomography: Recovery of optical absorption coefficient maps of heterogeneous media". In: *Appl. Phys. Lett.* 88.23 (June 2006), pages. ISSN: 0003-6951. DOI: 10.1063/1.2209883.

- R.J. Zemp, C.K. Abbey, and M.F. Insana. "Linear system models for ultrasonic imaging: application to signal statistics". In: *Ultrasonics, Ferroelectrics and Frequency Control, IEEE Transactions on* 50.6 (June 2003), pp. 642–654. ISSN: 0885-3010. DOI: 10.1109/TUFFC.2003.1209551.
- Roger J. Zemp. "Quantitative photoacoustic tomography with multiple optical sources". In: *Appl. Opt.* 49.18 (June 2010), pp. 3566–3572. DOI: 10.1364/AO.49.003566.
- Roger J. Zemp, Alexander Sampaleanu, and Tyler Harrison. "S-Sequence Encoded Synthetic Aperture B-Scan Ultrasound Imaging". *IEEE International Ultrasonics Symposium*. 2013.
- Roger J Zemp et al. "Photoacoustic imaging of the microvasculature with a high-frequency ultrasound array transducer". In: *Journal of biomedical optics* 12.1 (2007), p. 010501. ISSN: 1083-3668. DOI: 10.1117/1.2709850.
- Roger J Zemp et al. "Photoacoustic imaging of the microvasculature with a high-frequency ultrasound array transducer". In: *Journal of biomedical optics* 12.1 (2007), p. 010501. ISSN: 1083-3668. DOI: 10.1117/1.2709850.
- Roger J. Zemp et al. "Realtime photoacoustic microscopy in vivo with a 30-MHz ultrasound array transducer". In: *Opt. Express* 16.11 (May 2008), pp. 7915–7928. DOI: 10.1364/OE.16.007915.
- Lvming Zeng et al. "High antinoise photoacoustic tomography based on a modified filtered backprojection algorithm with combination wavelet". In: *Medical Physics* 34.2 (2007), pp. 556–563. DOI: 10.1118/1.2426406.
- Yaguang Zeng et al. "Photoacoustic and ultrasonic coimage with a linear transducer array". In: *Opt. Lett.* 29.15 (2004), pp. 1760–1762.
- Chi Zhang and Yuanyuan Wang. "Deconvolution reconstruction of full-view and limited-view photoacoustic tomography: a simulation study".

In: *J. Opt. Soc. Am. A* 25.10 (Oct. 2008), pp. 2436–2443. DOI: 10.1364/JOSAA.25.002436.

- Edward Zhang, Jan Laufer, and Paul Beard. "Backward-mode multiwavelength photoacoustic scanner using a planar Fabry-Perot polymer film ultrasound sensor for high-resolution three-dimensional imaging of biological tissues". In: *Appl. Opt.* 47.4 (Feb. 2008), pp. 561–577. DOI: 10.1364/AO.47.000561.
- Hao F Zhang et al. "Functional photoacoustic microscopy for high-resolution and noninvasive in vivo imaging". In: *Nat. Biotechnol.* 24.7 (July 2006), pp. 848–51. ISSN: 1087-0156. DOI: 10.1038/nbt1220.
- Hao F Zhang et al. "Imaging of hemoglobin oxygen saturation variations in single vessels in vivo using photoacoustic microscopy". In: *Appl. Phys. Lett.* 90.5 (2007), p. 053901. ISSN: 00036951. DOI: 10.1063/1.2435697.